# Energy and Charge Transfer at Hybrid Interfaces Probed by Optical Spectroscopy

Dissertation

zur Erlangung des akademischen Grades

doctor rerum naturalium

(Dr. rer. nat.)

im Fach Physik

Spezialisierung Experimentalphysik

eingereicht an der

Mathematisch-Naturwissenschaftlichen Fakultät

der Humboldt-Universität zu Berlin

von

M. Sc. Niklas Mutz

Präsidentin der Humboldt-Universität zu Berlin

Prof. Dr.-Ing. Dr. Sabine Kunst

Dekan der Mathematisch-Naturwissenschaftlichen Fakultät

Prof. Dr. Elmar Kulke

Gutachter/innen:

PD Dr. Sylke Blumstengel

Prof. Dr. Oliver Benson

Prof. Dr. Wolfram Heimbrodt

Tag der mündlichen Prüfung: 03.03.2021

# Abstract

Hybrid inorganic/organic systems offer the possibility of combining the advantages of both material classes such as high carrier mobilities in inorganic semiconductors and large light-matter interaction in organic ones. In order to benefit from these heterostructures, a thorough understanding of the processes at the interface is needed. Two occurring processes, that are looked at in this thesis, are non-radiative Förster resonance energy transfer (FRET) and excited-state charge transfer.

FRET is studied between a single InGaN/GaN quantum well and the polymer Cn-ether PPV. Despite the large internal electric fields in the quantum well, efficient FRET is possible as long as other non-radiative decay channels are suppressed. This is shown by temperature-dependent PL and PLE spectroscopy. At low temperatures of 30 K, a transfer efficiency of 0.46 is obtained from time-resolved PL measurements. PLE spectra clearly demonstrate an enhanced light emission from the acceptor. At elevated temperatures, non-radiative decay pathways become dominant.

Excited-state charge transfer is studied on $MoS_2$ in combination with the molecule $H_2Pc$. Monolayer $MoS_2$ is a promising candidate for ultra-thin opto-electronic devices. The combination with molecules has the prospect to further extend its functionality. Photoelectron spectroscopy (PES) reveals a type II energy level alignment at the $MoS_2/H_2Pc$ interface. Excited electrons are transferred from $H_2Pc$ to $MoS_2$ which is deduced from a shortening of the $H_2Pc$ PL decay time. Photocurrent action spectra show that the transferred electrons are not lost at the interface, but contribute to an enhanced photoconductivity.

Additionally to the $MoS_2$ hybrid samples, bare 2D transition-metal dichalcogenides (TMDCs) are studied. In order to fabricate high-quality TMDC monolayers, a physical vapour deposition method was developed in-house. The grown monolayers are characterised by optical spectroscopy. The versatility of the method is demonstrated by the growth of $Mo_{1-x}W_xS_2$ alloys and $TaS_2/MoS_2$ layered thin films with atomically sharp interfaces. The influence of the substrate dielectric function is investigated by comparing band-gaps measured by PES with the exciton transition energies obtained by reflectance measurements. An almost equal reduction in both energies with the substrate dielectric constant is seen.

# Zusammenfassung

Hybride Systeme, bestehend aus anorganischen und organischen Materialien, eröffnen die Möglichkeit deren individuelle Vorteile zu kombinieren. Diese sind u.a. eine hohe elektronische Mobilität in anorganischen und starke Licht-Materie-Wechselwirkung in organischen Halbleitern. Ein sinnvoller Nutzen der hybriden Systeme setzt ein umfassendes Verständnis der Prozesse an der Grenzfläche voraus. Zwei solcher Prozesse, die in dieser Arbeit behandelt werden, sind nicht-strahlender Förster-Resonanzenergietransfer (FRET) und Ladungstransfer im angeregten Zustand.

FRET wird zwischen einem InGaN/GaN Quantengraben und dem Polymer Cn-ether PPV untersucht. Es wird festgestellt, dass trotz des hohen internen elektrischen Feldes im Quantengraben effizienter Energietransfer möglich ist, solange andere nicht-strahlende Zerfallsprozesse unterdrückt werden. Dies wird mittels temperaturabhängiger PL und PLE Spektroskopie gezeigt. Eine Transfereffizienz von 0.46 ergibt sich aus zeitlich aufgelösten PL Messungen bei 30 K. PLE demonstriert zudem eine eindeutige Erhöhung der Lichtemission des Akzeptors. Bei höheren Temperaturen dominieren im Gegensatz dazu nicht-strahlende Zerfallskanäle.

Ladungstransfer im angeregten Zustand wird an einem System aus $MoS_2$ und dem Molekül $H_2Pc$ untersucht. $MoS_2$ als Monolage ist ein aussichtsreicher Kandidat für ultra-dünne optoelektronische Bauelemente. Die Kombination mit organischen Molekülen verspricht deren Funktionalität zu erweitern. Photoelektronenspektroskopie (PES) deckt einen Typ-II Heteroübergang an der $MoS_2/H_2Pc$ Grenzfläche auf. Aus einer Verkürzung der PL Zerfallszeit des $H_2Pc$ wird gefolgert, dass angeregte Elektronen von den $H_2Pc$ Molekülen in die $MoS_2$ Monolage übergehen. Photostrommessungen demonstrieren zudem, dass die transferierten Elektronen zu einer erhöhten Photoleitfähigkeit im $MoS_2$ beitragen.

Zusätzlich zu der hybriden Struktur werden auch einzelne zwei-dimensionale Übergangsmetall Dichalkogenide (TMDCs) untersucht. Um TMDCs von hoher Qualität herzustellen, wird eine intern entwickelte Methode der physikalischen Gasphasenabscheidung vorgestellt. Mittels PL Spektroskopie werden die so hergestellten Schichten charakterisiert. Die Vielseitigkeit der Methode wird anhand des Wachstums von $Mo_{1-x}W_xS_2$ Mischkristallen, sowie $TaS_2/MoS_2$ Heterostrukturen dargelegt. Der Einfluss der dielektrischen Funktion des Substrates auf die TMDC Bandlücke und die Bindungsenergie der Exzitonen wird erforscht. Durch die Kombination von PES und Reflexionsmessungen kann eine gleichzeitige Abnahme sowohl der Bandlücke als auch der Bindungsenergie gezeigt werden.

# Contents

**List of Figures** iii

**List of Abbreviations** v

**1 Introduction** 1

**2 Experimental methods and analysis** 5

2.1 Sample preparation and characterisation . . . . . 5

2.1.1 Spin coating . . . . . 5

2.1.2 Organic molecular beam deposition . . . . . 6

2.1.3 Atomic force microscopy . . . . . 7

2.1.4 Pulsed thermal deposition of TMDCs . . . . . 8

2.1.5 TMDC transfer . . . . . 8

2.2 Absorbance, photoluminescence and reflectance measurements . . . . . 9

2.2.1 UV-Vis-NIR absorption spectroscopy . . . . . 9

2.2.2 PL emission and excitation spectroscopy . . . . . 10

2.2.3 Time-correlated single photon counting and multichannel scaling . . . . 11

2.2.4 Differential reflectance spectroscopy . . . . . 11

2.2.5 Macro-PL setup . . . . . 13

2.2.6 Micro-PL setup . . . . . 13

2.3 Transmission electron microscopy . . . . . 14

2.4 Photoelectron spectroscopy . . . . . 15

2.5 Raman spectroscopy . . . . . 16

2.6 Photocurrent action spectroscopy . . . . . 17

**3 FRET between an InGaN/GaN quantum well and the polymer Cn-ether PPV** 19

3.1 Fundamentals . . . . . 21

3.1.1 Gallium Nitride . . . . . 21

3.1.2 Cn-ether-PPV . . . . . 23

3.1.3 FRET . . . . . 25

3.2 Results and Discussion . . . 27
3.2.1 Quantum well structure . . . 28
3.2.2 Cn-ether PPV . . . 32
3.2.3 Hybrid structure . . . 34
3.3 Summary and outlook . . . 39

**4 Growth and optical properties of transition metal dichalcogenides 43**
4.1 TMDC fundamentals . . . 44
4.1.1 Band structure properties . . . 45
4.1.2 Optical properties and defects . . . 47
4.1.3 Charge carrier transport and doping . . . 50
4.1.4 Raman spectra . . . 51
4.1.5 Influence of the dielectric surrounding on the electronic and excitonic states 52
4.1.6 Fabrication methods of monolayer TMDCs . . . 54
4.2 Pulsed thermal deposition . . . 55
4.2.1 Experimental background . . . 55
4.2.2 Characterisation of TMDC monolayers . . . 57
4.2.3 TMDC alloys and heterostructures . . . 63
4.3 The influence of the substrate . . . 67
4.3.1 Differential reflectance spectra of $MoS_2$ and $WSe_2$ . . . 67
4.4 Summary and outlook . . . 70

**5 Excited state charge transfer in a hybrid $MoS_2$/$H_2$Pc system 73**
5.1 Hybrid TMDC/organic systems - an overview . . . 74
5.1.1 Energy level alignment . . . 74
5.1.2 TMDC/organic heterostructures - literature overview . . . 75
5.2 Hybrid TMDC/organic systems - experimental results and discussion . . . 78
5.2.1 Why TMDC/Pc heterostructures? . . . 78
5.2.2 Excited state charge transfer at the $MoS_2$/$H_2$Pc interface . . . 81
5.3 Summary and outlook . . . 90

**6 Conclusion and outlook 93**

**Bibliography 97**

**List of publications 119**

**Acknowledgements 121**

# List of Figures


2.1 AFM working principle . . . . . 7
2.2 $MoS_2$ transfer . . . . . 9
2.3 Micro-PL setup . . . . . 14
2.4 Principle of Raman spectroscopy . . . . . 16

3.1 III-Nitride structure . . . . . 22
3.2 QCSE . . . . . 23
3.3 PPV derivatives . . . . . 24
3.4 Dipole orientation FRET . . . . . 27
3.5 InGaN/GaN QW structure . . . . . 28
3.6 Bare QW PL . . . . . 29
3.7 Calculated QW band structure . . . . . 30
3.8 Temperature and excitation dependent QW PL . . . . . 31
3.9 QW PL decay . . . . . 32
3.10 Bare Cn-ether PPV PL . . . . . 33
3.11 Scheme of the hybrid QW/Cn-ether PPV structure . . . . . 34
3.12 Hybrid QW/Cn-ether PPV PL and PLE . . . . . 35
3.13 Transfer efficiency from PLE . . . . . 36
3.14 PL decay in the hybrid QW/Cn-ether PPV sample . . . . . 38
3.15 Temperature dependent transfer efficiency . . . . . 38
3.16 Comparison of the decay channels in the hybrid QW/Cn-ether PPV sample . . 39
3.17 Summary picture QW/Cn-ether PPV . . . . . 40

4.1 TMDC structure . . . . . 45
4.2 Indirect to direct band gap transition . . . . . 46
4.3 Appellation of excitonic peaks in $MoS_2$ . . . . . 48
4.4 TMDC Raman spectrum . . . . . 51
4.5 TMDC monolayer fabrication . . . . . 54
4.6 PTD scheme . . . . . 56
4.7 Effect of growth time on TMDC PL and absorption . . . . . 58

4.8 $MoS_2$ TEM cross-section . . . 58
4.9 Optical microscope images $MoS_2$ obtained by three different methods . . . 59
4.10 PL and absorbance of $MoS_2$ obtained by PTD, CVD and exfoliation . . . 60
4.11 Influence of air on PL . . . 61
4.12 Soda lime as growth substrate . . . 62
4.13 PL and absorbance of $Mo_{1-x}W_xS_2$ . . . 64
4.14 Raman spectra of $Mo_{1-x}W_xS_2$ . . . 65
4.15 $TaS_2$ transmission . . . 66
4.16 TEM of $TaS_2/MoS_2$ heterostructure . . . 67
4.17 DRS spectra with exciton transition energies . . . 68
4.18 PES results on sapphire and gold substrates . . . 69
4.19 Exciton transition energy vs. dielectric constant . . . 70

5.1 Schematic energy level alignment . . . 75
5.2 $H_2Pc$ structure . . . 79
5.3 PES results at the $MoS_2/H_2Pc$ interface . . . 82
5.4 XPS of the $MoS_2/H_2Pc$ structure . . . 83
5.5 Derived $MoS_2/H_2Pc$ energy level alignment . . . 84
5.6 PL and absorbance of the hybrid $MoS_2/H_2Pc$ structure . . . 85
5.7 Different stacking of $H_2Pc$ molecules . . . 86
5.8 $MoS_2/H_2Pc$ PL decay . . . 87
5.9 Hybrid photoconductor scheme . . . 88
5.10 PAS of the $MoS_2/H_2Pc$ hybrid . . . 89
5.11 Morphology of $H_2Pc$ . . . 90
5.12 PL of a TDAF/$MoS_2$ hybrid structure . . . 91

# List of Abbreviations

| | |
|---|---|
| 2D/3D | two/three-dimensional |
| AFM | Atomic force microscopy |
| BCB | Benzocyclobutene |
| C8-BTBT | 2,7-Dioctyl[1]benzothieno[3,2-b][1]benzothiophene |
| C60(F48) | (Fluorinated) fullerene |
| CBM | Conduction band minimum |
| CCD | Charge-coupled device |
| Cn-ether PPV | Cyano-substituted ether-linked (p-phenylene vinylene) |
| CVD | Chemical vapour deposition |
| CW | Continuous wave |
| DOS | Density of states |
| DFT | Density functional theory |
| DRS | Differential reflectance spectroscopy |
| EDXS | Energy-dispersive X-ray spectroscopy |
| F4TCNQ | 2,3,5,6-Tetrafluoro-7,7,8,8-tetracyanoquinodimethane |
| F6TCNNQ | 1,3,4,5,7,8-hexafluorotetracyano-naphthoquinodimethane |
| FET | Field-effect transistor |
| FRET | Förster resonance energy transfer |
| FWHM | Full-width at half maximum |
| h-BN | Hexagonal boron nitride |
| $H_2O$ | Water |
| $H_2Pc$ | Metal-free phthalocyanine |
| $HfO_2$ | Hafnium dioxide |
| HIOS | Hybrid inorganic/organic system |
| HOMO | Highest occupied molecular orbital |
| HOPG | Highly oriented pyrolytic graphite |
| IE | Ionisation energy |
| ID | Interface dipole |
| InGaN | Indium gallium nitride |

| | |
|---|---|
| IPES | Inverse photoelectron spectroscopy |
| IRF | Instrument response function |
| ITO | Indium tin oxide |
| LED | Light emitting diode |
| LO | longitudinal optical |
| LUMO | Lowest unoccupied molecular orbital |
| MBE | Molecular beam epitaxy |
| MCS | Multichannel scaling |
| $MoS_2$ | Molybdenum disulfide |
| NADH | Nicotinamide adenine dinucleotide |
| $O_2$ | Dioxygen |
| OMBD | Organic molecular beam deposition |
| PAS | Photocurrent action spectroscopy |
| PES | Photoelectron spectroscopy |
| PDMS | Polydimethylsiloxane |
| PL | Photoluminescence |
| PLE | Photoluminescence excitation |
| PMMA | Polymethyl methacrylate |
| PS | Polystyrene |
| PTB7 | Poly[[4,8-bis[(2-ethylhexyl)oxy]benzo[1,2-b:4,5-b']<br>dithiophene-2,6-diyl][3-fluoro-2-[(2-ethylhexyl)carbonyl]<br>thieno[3,4-b]thiophenediyl]] |
| PTCDA | Perylenetetracarboxylic dianhydride |
| PTD | Pulsed thermal deposition |
| PVD | Physical vapour deposition |
| QCM | Quartz crystal microbalance |
| QCSE | Quantum-confined Stark effect |
| QW | Quantum well |
| QY | Quantum yield |
| SECO | Secondary electron cut-off |
| $SiO_2$ | Silicon dioxide |
| SOC | Spin-orbit coupling |
| STS | Scanning tunnelling spectroscopy |
| $TaS_2$ | Tantalum disulfide |
| TCSPC | Time-correlated single photon counting |
| TDBC | 5,6-dichloro-2[3-[5,6-dichloro-1-ethyl-3-(3-sulfopropyl)-2(3H) |

| | |
|---|---|
| | -benzimidazolidene]-1-propenyl]-1-ethyl-3-(3-sulfopropyl) benzimidazolium hydroxide |
| TFSI | bis(trifluoromethane) sulfonimide |
| TDAF | Bis[9,9-di(4-methylphenyl)-fluoren-2-yl]-9,9- di(4-methylphenyl)fluorene |
| (S)TEM | (Scanning) transmission electron microscopy |
| TMDC | Transition metal dichalcogenide |
| UHV | Ultrahigh vacuum |
| UPS | Ultraviolet photoelectron spectroscopy |
| UV-Vis-NIR | Ultraviolet-visible-near-infrared |
| VBM | Valence band maximum |
| $WS_2$ | Tungsten disulfide |
| $WSe_2$ | Tungsten diselenide |
| XPS | X-ray photoelectron spectroscopy |
| ZnO | Zinc oxide |

# 1 Introduction

Comprehension of electronic processes at the interface is key to design or improve any heterostructure device functionality. Or as the Nobel prize laureate Herbert Krömer put it: *[...] it may be said that the interface is the device* [1]. Under a heterostructure one understands the combination of two or more dissimilar materials and the interface is where they spatially meet. More precisely, the materials under question are typically inorganic semiconductors. Nowadays, it is common to find an example of such a heterostructure in everyday life when turning on the room light or the television screen. These white light emitting diodes (LEDs) are made up, for example, of heterostructures of the III-V semiconductor compounds aluminium (AlN), gallium (GaN) and indium nitride (InN). Other applications of heterostructures are found in telecommunication, optical sensors and solid state laser diodes [2]. On the other hand, organic small molecules and polymers are also widely researched and used for lighting or photovoltaic applications so that when turning on the television screen it might actually be an organic LED display. Instead of having inorganic and organic structures separately they can also be merged and the term *heterostructure* needs to be expanded to hybrid inorganic/organic systems (HIOS). The advantages of inorganic semiconductors are their high crystalline purity, large charge carrier mobility and efficient carrier injection. Organic semiconductors, on the other hand, offer better mechanical flexibility, can obtain higher optical absorption and emission cross-sections and are more easily chemically modified to change their electrical and optical properties. Combining inorganic and organic semiconductors is hence aiming at preserving the advantages of both material classes while compensating for individual drawbacks.

Of course, precise understanding of the interface is also needed in HIOS. Many studies have already been devoted to understanding different hybrid systems including zinc oxide, gallium nitride, gallium arsenide, transition metal dichalcogenides, silicon etc. to name only a few inorganic counterparts [3–12]. These studies lay the foundation for further investigations. Although the details in the individual studies differ, two main goals can be generally extracted. The first aim is to accumulate electron-hole pairs in one material by transfer from the other one thereby enhancing light emission. The second aim is to separate electron and hole at the interface and creating free charge carriers which can be used in light harvesting or sensor applications. Both aims are looked at within this thesis. Given the vast number of inorganic

and organic compounds, two inorganic semiconductor classes were chosen for the presented studies, namely bulk and two-dimensional semiconductors.

In this respect, the thesis is subdivided into three main parts. Chapter 3 and 5 cover the topic of hybrid inorganic/organic interfaces using an example of either one of the aforementioned two semiconductor classes in combination with organic molecules. Chapter 4 is entirely devoted to the inorganic class of two-dimensional transition metal dichalcogenides. Among others, it discusses topics relevant for the understanding of chapter 5 so that it precedes the HIOS chapter. Each chapter is based on results obtained during the course of this doctorate which are already published in peer-reviewed journals. Additionally, a more detailed view on the individual studies as well as some additional data is presented in order to deepen the discussion. Each chapter is introduced with the fundamentals necessary to understand the topic and an overview over existing literature. Subsequently, the experimental results will be presented and discussed which is followed by a conclusion. The thesis is finalised with a more general outlook on the three individual chapters in chapter 6. A short overview over the chapters three to five is given in the following.

The first semiconductor system - presented in chapter 3 - is a quantum well consisting of InGaN within GaN barriers. GaN and its alloys with InN are the basis of blue light emitting diodes. Usually, the blue LED radiatively pumps a phosphor that is used as colour converter to achieve white light emission. By bringing the active part of the LED within a distance of a few nanometres to the colour converter, it is possible to make use of non-radiative Förster-like resonance energy transfer (FRET). Efficient FRET was shown for ZnO in combination with small molecules [4, 5] and was also investigated for InGaN/GaN quantum wells [8, 9]. Although FRET was already studied with InGaN/GaN, it was not demonstrated that the excitons drained from the quantum well also lead to an enhancement in the emission of the acceptor. Additionally, large internal electric fields exist in InGaN/GaN quantum well structures reducing the FRET rate [13]. If these fields cannot be avoided, the question arising here is if FRET is still a useful alternative to the radiative colour conversion in conventional white LEDs. Both of these issues are tackled in the thesis by investigating FRET from a single InGaN/GaN quantum well to a PPV-derivative polymer called Cn-ether PPV. It is shown that despite large electric fields on the order of MV/cm, efficient FRET is still possible. Moreover, it is demonstrated that the emission of Cn-ether PPV is enhanced as compared to pure radiative excitation.

Chapter 4 covers the second inorganic semiconductor class, the so-called two-dimensional transition-metal dichalcogenides (TMDCs). Similar to graphene, a carbon sheet of only one atom thickness, these TMDCs can be thinned down to one monolayer. In their pristine form they do not possess any dangling bonds and are therefore chemically inert. This makes them

interesting candidates to investigate interface phenomena. From a technological point of view, they possess strong light-matter coupling and large charge carrier mobilities making them useful for sensor and transistor applications. The understanding of hybrid interfaces firstly requires knowledge of the TMDC itself and its interaction with the substrate. Therefore, a novel growth method for TMDC monolayers is presented together with their optical properties. The growth of $Mo_{1-x}W_xS_2$ and $MoS_2/TaS_2$ heterostructures highlights the versatility of the growth method. The influence of the substrate and its dielectric function on the energetics of the two TMDCs $MoS_2$ and $WSe_2$ is discussed. An almost equal decrease in exciton binding energy and energy gap can be seen in dependence of the dielectric constant of the substrate which is complimentary, but consistent with other experimental and theoretical work found in literature [14–16].

The combination of TMDCs with organic molecules is discussed in chapter 5. The study presented in this part focuses on the charge transfer and separation at the hybrid $MoS_2/H_2Pc$ interface. This is different from the case of the hybrid InGaN/Cn-ether PPV system where exciton accumulation in the polymer was desired. $MoS_2$ is a widely used semiconducting TMDC and $H_2Pc$ is a small organic molecule of the family of the phthalocyanines used in organic photovoltaics. Although some insight in the charge transfer process at hybrid TMDC/organic interfaces can be found in literature, open questions remain [17–20]. The energy level alignment is not investigated in detail so far. Additionally, the process of charge transfer itself, as well as the possible use of the transferred charges, need to be elaborated. These issues are tackled for the example of an $MoS_2/H_2Pc$ photoconductor. It is found that the two materials form a type II heterostructure. Excited state electron transfer from $H_2Pc$ to $MoS_2$ leads to an enhancement in $MoS_2$ photoconductivity resulting in an extended spectral sensitivity.

The main method used to examine energy and charge transfer phenomena at hybrid interfaces in this thesis is optical spectroscopy. Time-integrated and -resolved photoluminescence measurements were performed and analysed on reference and hybrid samples. Measuring photoluminescence in dependence of temperature allowed for investigating non-radiative decay channels. These methods were combined with transmission electron microscopy, photoelectron, Raman and photocurrent spectroscopy in order to obtain a comprehensive view of the studied system. The following chapter will therefore firstly present the experimental methods and analysis before discussing the results.

# 2 Experimental methods and analysis

This chapter introduces the experimental methods and analysis used in this thesis. The focus of the presented topics lay on the preparation of the organic counterpart in the hybrid samples as well as the optical characterisation of reference and hybrid samples. The preparation by spin coating, organic molecular beam deposition (OMBD) and the transfer of transition metal dichalcogenides (TMDC) as well as the optical experiments such as UV-Vis, time-integrated and -resolved photoluminescence (PL) and differential reflectance spectroscopy (DRS), which were performed by the author, will therefore be presented in some detail. A comprehensive picture of hybrid samples, however, relies also on other's peoples input as well as experimental techniques and analysis. Since the conclusions drawn in this thesis are also based on this work, an overview of these other techniques will be given. They include: transmission electron microscopy (TEM), photoelectron spectroscopy (PES), Raman spectroscopy and Photocurrent action spectroscopy (PAS). The growth of TMDC monolayers performed by Dr. Sergey Sadofev will be discussed in more detail chapter 4.

## 2.1 Sample preparation and characterisation

Two preparation methods for the fabrication of nanometre-thin organic films are given in this section, namely spin coating and OMBD. The technique of atomic force microscopy (AFM) was used to characterise the thickness and morphology of the prepared films. Additionally, transfer of TMDC monolayers from their growth substrate to the desired substrate was done based on a wet-transfer method. Both methods, AFM and TMDC transfer, are also detailed in the following paragraphs.

### 2.1.1 Spin coating

Spin coating is a vastly applied and easy-to-use method to obtain thin and homogeneous films from solution. The material under investigation is dissolved in an appropriate solvent such as water, ethanol, toluene, etc. This solution is dropped onto a rotating substrate. The film thickness depends on the rotation speed and the concentration of the solution. In this thesis, films of the polymers Cn-ether PPV (chapter 3), Polystyrene (chapter 5) and a BCB-based

polymer (chapter 5) were fabricated by this method. Cn-ether PPV was dissolved in toluene at a concentration of 1.0 mg/ml and left stirring over night to ensure that it was dissolved properly. Thin films were prepared on sapphire substrates or InGaN/GaN by spin coating under nitrogen atmosphere in a glove box. For a 5 nm thick film of Cn-ether PPV 10 µl were spun at 4800 rpm for 60 seconds. Polystyrene was used as a supporting polymer for water-assisted transfer of TMDC monolayers. Typically, a rotation speed of 3000 rpm for 60 seconds was used to obtain a good result in the transfer for a PS concentration of 90 mg/ml. The BCB-based polymer was obtained by diluting cyclotene 3022-35 (Dow-Chemicals) with two parts mesitylene. This mixture was spin coated at 500 rpm for 10 s and 5000 rpm for 120 s to obtain a 170 nm thick film. Subsequently the film was annealed at 270 °C for 10 minutes in a nitrogen filled glovebox.

### 2.1.2 Organic molecular beam deposition

Vacuum sublimation of small organic molecules and the fabrication of molecular films can be done by OMBD. The molecules are placed in a ceramic crucible in a vacuum chamber evacuated to $\sim 10^{-8}$ mbar. Heating the crucible will lead to the sublimation of the small molecules at a certain temperature. Molecular flux control is given by the temperature. The molecules will impinge on a substrate where they can form crystalline or amorphous films. Two shutters separate the molecule reservoir and the growth substrate. Shadow masks can be introduced in front of the substrate to prevent desired areas from being covered with molecules. In such a way, reference and hybrid organic/inorganic regions can be investigated on the same sample. A quartz crystal microbalance (QCM) is used to monitor the growth rate and thickness of the molecular film. Its measuring principle is as follows: Quartz can be brought into oscillations by applying an alternating electric field. The resonance frequency is dependent on the thickness of the quartz crystal and a change in the frequency can be put into relation with a change in the mass of the QCM. If molecules are deposited onto the substrate, they are also deposited on the QCM allowing to extract the growth rate [21]. A calibration measurement needs to be performed for each material to determine the desired thickness which is stored in the so-called tooling factor. Transfer from the evacuated growth chamber to a glove box filled with nitrogen is possible in the OMBD system used here without contact with ambient air. For this, a transfer cart can be attached to the load lock with the as-prepared sample. Subsequently, the sample is transferred into the glove box. This is important since contact with oxygen and water present in ambient air can lead to a degradation or alteration of the properties of the molecular film.

During the course of this thesis two molecules were evaporated using the OMBD system: Metal-free phthalocyanine ($H_2Pc$) and 2,7-Bis[9,9-di(4-methylphenyl)-fluoren-2-yl]-9,9-

di(4-methylphenyl)fluorene (TDAF) which were both used in conjunction with TMDCs. $H_2Pc$ was evaporated at a temperature of 265 °C resulting in a rate of 3.5 Å/min. The tooling factor was determined to be 111 % by growing a 15 nm thick layer of $H_2Pc$ and measuring its thickness in AFM. For TDAF a rate of 3.5 Å/min was used at a temperature of 257 °C with a tooling factor of 133 %. The substrate was kept at room temperature and the pressure during growth was always below $3 \cdot 10^{-8}$ mbar.

### 2.1.3 Atomic force microscopy

AFM was used within this thesis as a tool to determine the thickness and morphology of thin organic films and TMDCs. Figure 2.1 displays schematically the working principle. A cantilever with a microscopically sharp tip is scanned over the sample. When in proximity to a surface, the cantilever is subject to a force leading the cantilever to bend, similar to a springboard. This force depends on the distance of the tip to the surface which is repulsive close to and attractive farther away from the surface and modelled with a Lennard-Jones potential [22]. At every point, a laser beam is focussed on the cantilever and reflected onto a sensor to track its deformation. In this way, a parameter can be measured as the input for a feedback loop and kept fixed by varying the distance to the surface through a piezo stage. Such a parameter can

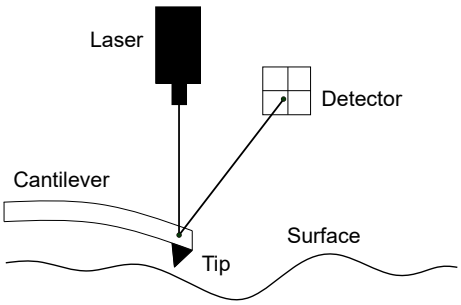


Figure 2.1: Sketch of the working principle of an AFM. Adapted from [22].

be the force on the cantilever so that the distance between sample and tip is kept constant (contact mode). A more commonly used mode is tapping mode in which the cantilever is driven close to its resonance frequency. The force acting on the cantilever will lead to a shift in this frequency. In turn, the shift leads to a change in the amplitude of the driven oscillation. This is used as the input parameter for the feedback loop to control the piezo. Tapping mode is less demanding on the tip and the sample since the average distance of the tip is larger than in contact mode and the time at short distances is much smaller. In this thesis a Bruker AFM (Bruker Dimension Icon) was used with the so-called *Peak Force Tapping* mode in which the cantilever oscillates well below its resonance frequency. The force on the tip is measured

by the deformation of the cantilever and the maximum repulsive force is kept constant. The advantage of this mode is that the maximum repulsive force is reduced from ∼1 nN to 10 pN [23].

### 2.1.4 Pulsed thermal deposition of TMDCs

The fabrication of monolayer TMDCs is typically done either by mechanical exfoliation, chemical vapour deposition (CVD) or physical vapour deposition (PVD). In order to fabricate TMDCs in-house, a novel PVD method was developed and applied by Dr. Sergey Sadofev using a metal wire and chalcogen powder as the precursors. The current sent through the metal wire leads to the sublimation of metal which is sufficient to produce TMDC mono- and multilayers by simultaneously evaporating chalcogen. Since the fabrication process and the TMDC characterisation is an integral part of the thesis, the details of this PVD method are given in chapter 4.

### 2.1.5 TMDC transfer

TMDC monolayers are usually grown on sapphire or quartz substrates. To transfer the monolayers onto a different substrate or device, some processes have been developed, as documented in literature [24]. Mainly two routes can be distinguished. They differ whether the process does or does not involve a solvent. In the dry transfer process, polydimethylsiloxane (PDMS), or Poly-methyl methacrylate (PMMA), is usually used as a stamp to peel away the TMDC monolayer [25]. In the wet transfer method, one makes use of the larger hydrophobicity of the TMDCs compared to the growth substrate [26]. Water penetrates between the TMDC and the substrate, thereby separating the two. The monolayer floats on water and can be picked up with the desired substrate. Within the studies here, water assisted transfer of $MoS_2$ was used and will be presented in the following.

The workflow is shown in figure 2.2. In general, a supporting layer is not needed to float off the $MoS_2$ [25], but the monolayer tends to fall apart after lift-off except for a few cases tested in this thesis. Thus, $MoS_2$ on its substrate was covered with a layer of polystyrene (PS) by spin coating as supporting layer. Afterwards, the edges and the back side of the substrate were cleaned with a q-tip soaked in toluene followed by annealing at 90 °C for 15 minutes. A water droplet is brought into contact with the substrate/$MoS_2$/PS-stack and the $MoS_2$/PS is floated off the substrate. The old substrate can then be removed and a new one placed below the floating $MoS_2$/PS. After positioning, residual water is removed with a pipette and a clean tissue. Afterwards the whole stack is annealed again at 80 °C for 1 hour and subsequently at 150 °C for 30 min. PS is washed away by dipping and rinsing with warm toluene. Finally, the

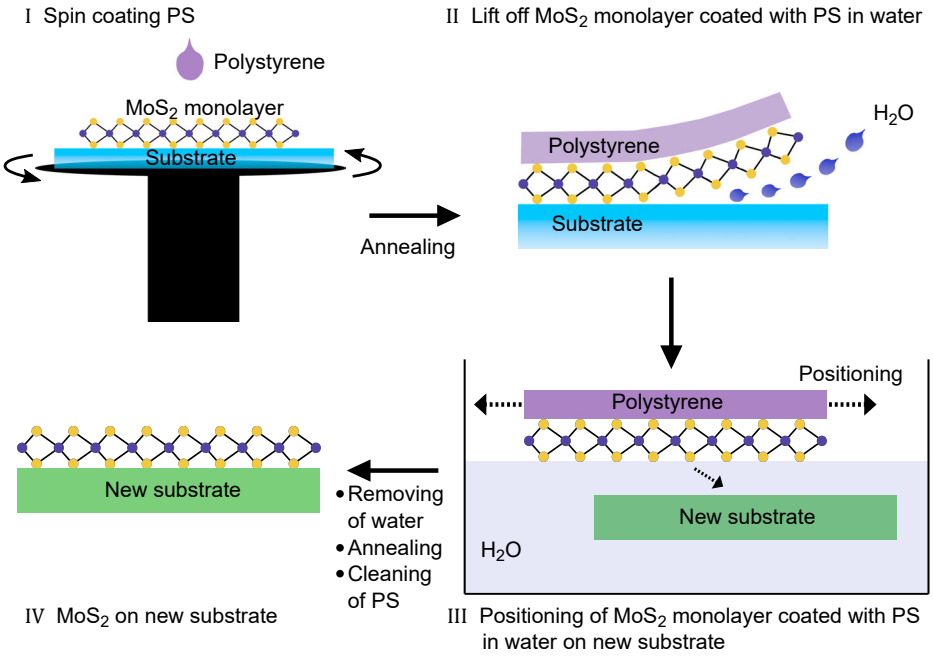


Figure 2.2: Steps involved in the water-assisted transfer of $MoS_2$.

transferred sample is dried with nitrogen.

## 2.2 Absorbance, photoluminescence and reflectance measurements

In the following, methods for the optical characterisation of organic films, TMDC monolayers and hybrid structures by absorption, PL and DR spectroscopy are presented.

### 2.2.1 UV-Vis-NIR absorption spectroscopy

Knowledge of the absorption spectrum is a crucial step in understanding the excited states of a material. Insight can be gained with a so-called UV-Vis(-NIR) spectrometer. Its name stems from the spectral range that is covered, i.e. from the ultraviolet (UV) over the visible (Vis) to the near-infrared (NIR) electromagnetic spectrum. The accessible spectral range depends on the spectrometer used. Here, absorbance spectra were acquired with a UV-2101PC (Shimadzu) and a Lambda UV-Vis-NIR (Perkin Elmer) spectrometer. The UV-2101PC has a spectral range from around 5 eV to 1.4 eV while the Lambda UV-Vis-NIR can be used to monitor spectra also within the near-infrared spectrum up to ∼0.4 eV. In a typical measurement, absorption is not measured directly, but the transmittance of a sample. The light intensity $I_T$ transmitted

through a material is reduced by absorption as given by the Lambert-Beer law $I(d) = I_0 e^{-\alpha d}$. Here, $I(d)$ is the light intensity after travelling a distance $d$ in the material. $I_0$ is the impinging light intensity and $\alpha$ is the absorption coefficient. Additionally, $I_T$ is reduced by reflection and scattering. Then, the absorbance $A$ of a thin film is defined as $A = -log(\frac{I_T}{I_0})$. This is what is usually measured in a UV-Vis spectrometer as long as no integrating sphere is used that additionally collects the reflected and scattered light. $I_0$ is conveniently measured simultaneously. The light beam from the excitation source, usually a halogen or deuterium lamp, is split into two beams with the same intensity. One is sent through the sample, the other one through a reference, for example the bare substrate. Both beams are then registered by a detector.

### 2.2.2 PL emission and excitation spectroscopy

After the absorption of light, the material is in an electronically excited state which can decay radiatively, i.e. under the emission of photons. This process is called photoluminescence since the excitation is done by light. In a typical PL spectrum, the excitation energy is held constant and the emission is detected over a certain energy range. The emitted light can be dispersed by a prism, but mostly gratings are used. A grating diffracts the light so that each energy shows constructive interference only at certain angles. By varying the angle of incidence, the light energy can be selected by a slit and detected with a photomultiplier tube or a charge-coupled device (CCD) where each pixel column serves as slit and detector. When detecting the emission only at a certain energy and the excitation energy is scanned, one speaks of PL excitation (PLE) spectroscopy. PLE is a useful technique since it shows which excitation energy leads to the emission under investigation. Put differently, it shows which excited states 'feed' the emissive species. Usually, PLE spectra resemble absorption spectra. This can be seen from the PL intensity

$$I_{PL}(E_{em}) \propto \eta I_0(E_{exc})(1 - e^{-\alpha(E_{exc})d}) \approx \eta I_0(E_{exc})\alpha(E_{exc})d\,, \tag{2.1}$$

so that $\frac{I_{PL}(E_{em})}{I_0(E_{exc})} \propto \alpha(E_{exc})$. Here, $\eta$ is the PL quantum yield, i.e. the probability of a radiative decay to happen, $E_{\{em,exc\}}$ is the emission and excitation energy, respectively. The approximation holds for $\alpha d << 1$ [27]. This gives the possibility of obtaining absorption spectra also for samples where transmission cannot be measured. On the other hand, PLE can also serve to detect transfer processes in heterogeneous material combinations, like hybrid inorganic/organic systems (HIOS). For example, energy transfer from material one to material two can lead to an absorption feature of material one in the PLE spectrum of material two.

### 2.2.3 Time-correlated single photon counting and multichannel scaling

The aforementioned PL and PLE spectra are typically acquired under continuous excitation so that no insight into the excited state dynamics is given. Different techniques exist for capturing such information. The one applied here is time-resolved PL spectroscopy with the methods called time-correlated single photon counting (TCSPC) and multichannel scaling (MCS). Depending on the decay time, either TCSPC or MCS is used. For fluorescence, i.e. decay times in the ps to µs range, TCSPC is applicable while for longer decays (phosphorescence) MCS is worked with. Both methods use a pulsed excitation source. In TCSPC, the excitation pulse gives a trigger signal as a starting point and the time is counted until an emitted photon is registered. If a photon is detected, the time correlated to this photon is stored in a histogram. After many of these measurements the decay curve is formed. Limitations are given by the measurement electronics. On average, much less than one photon per excitation pulse (∼5 %) needs to be detected. Otherwise, photons arriving slightly after the photon whose time was marked - but before the next excitation pulse - will not be registered in a new time slot. Therefore, the decay will appear faster than it actually is since 'later' photons will not contribute to the decay curve. MCS works similar but with the difference that all the counts from the detector are stored within a certain time window after the excitation trigger. These time-channels are swept consecutively. The downside is that the time-resolution is given by the time-channel width which is in the ns range.

PL decay transients ($I(t)$) are fitted by convoluting a model function ($Exp(t)$) with the measured instrument response function ($IRF(t)$) [28]. In this thesis only exponential decays were considered as model functions.

$$I(t) = \int_0^t IRF(t')Exp(t-t')dt' \,. \tag{2.2}$$

The IRF gives the time resolution of the overall experimental setup, i.e. detector, excitation source, optical components, etc. and is usually measured by detecting at the excitation energy. For a model function consisting of more than one exponential, the average lifetime was taken as $< \tau >= \int_0^\infty tI(t)dt / \int_0^\infty I(t)dt$.

### 2.2.4 Differential reflectance spectroscopy

DRS is a useful tool to determine the complex dielectric function $\epsilon = \epsilon_1 + i\epsilon_2$ of a thin film on a substrate. One measures the change in reflectance between a system with and without the thin film. The DR signal is defined as: $DRS = \frac{R(d)-R_0}{R_0}$. $R(d)$ is the measured reflectance of the thin film of thickness $d$ on top of a substrate. $R_0$ is the reference reflectance of the bare

substrate. DRS can be employed for example *in situ* during the growth of organic molecules [29] or it can be used to determine absorption spectra for films on non-transparent substrates. It is useful to measure for TMDCs, since often one deals with µm-sized flakes so that normal UV-Vis spectroscopy is not possible [30]. On transparent and non-interacting substrates; while measuring in vacuum or air; it holds that [31]

$$DRS = \frac{R - R_0}{R_0} \approx -\frac{8\pi d}{\lambda} Im\left(\frac{1-\epsilon_{tmdc}}{1-\epsilon_{sub}}\right) \approx \frac{16\pi d}{\lambda(1-n_{sub}^2)} n_{tmdc}\kappa_{tmdc}\,. \tag{2.3}$$

Here, $\epsilon_{tmdc}$ and $\epsilon_{sub}$ are the complex dielectric functions of the TMDC monolayer and the substrate. $n_{tmdc}$ and $\kappa_{tmdc}$ are the refractive index and extinction coefficient of the TMDC whereas the complex refractive index $\tilde{n}$ is given as $\sqrt{\epsilon} = \tilde{n} = n + i\kappa$. $n_{sub}$ is the refractive index of the substrate. The last approximation is valid as long as the substrate has a negligible absorption in the spectral region under investigation. The above is an approximation of the reflectivity of a three-layer system, i.e. air, thin film and substrate, derived for a plane electromagnetic wave utilising the Fresnel equations [32]. For a system which consists of more than three layers it is necessary to go back to the full expression of the reflectivity. This can be done by modelling $\epsilon_{tmdc}$ with Lorentz-oscillators. It follows for the real ($\epsilon_1$) and imaginary ($\epsilon_2$) part of each oscillator [33]:

$$\begin{aligned} \epsilon_1 &= \epsilon_\infty + \frac{\beta\omega_0^2(\omega_0^2-\omega^2)}{(\omega_0^2-\omega^2)^2+4\omega^2\gamma^2}\,, \\ \epsilon_2 &= \frac{2\omega\gamma\beta\omega_0^2}{(\omega_0^2-\omega^2)^2+4\omega^2\gamma^2}\,, \end{aligned} \tag{2.4}$$

whereas $\omega_0$ is the resonance frequency of the oscillator, $\gamma$ is the damping and $\beta = e^2N/(m_0\epsilon_0\omega_0^2)$ is the oscillator strength which is a measure of the probability of the transition to occur. In its definition, $N$ is the dipole density, $m_0$ and $e$ are the electron mass and elementary charge and $\epsilon_0$ is the vacuum permittivity. $\epsilon_\infty$ is the background dielectric constant at frequencies much larger than the resonance frequencies of the oscillators. In the analysis, it is summarised in the real part of one oscillator. If the complex dielectric functions of the substrate layers are known, one can calculate the total reflection using the transfer matrix formalism. The characteristic matrix $M$ for a layer with thickness $d$ and under normal incidence is given by [34]

$$M(d) = \begin{pmatrix} cos(\frac{2\pi}{\lambda}\tilde{n}d) & -\frac{i}{\tilde{n}}sin(\frac{2\pi}{\lambda}\tilde{n}d) \\ -i\tilde{n}sin(\frac{2\pi}{\lambda}\tilde{n}d) & cos(\frac{2\pi}{\lambda}\tilde{n}d) \end{pmatrix}. \tag{2.5}$$

The propagation of the electromagnetic wave is described by the product of the characteristic matrices of each layer. The total reflection coefficient is related to the entries $m_{k,l}$ of the overall

propagation matrix by:

$$r = \frac{(m_{1,1} + m_{1,2}\tilde{n_l})\tilde{n_0} - (m_{2,1} + m_{2,2}\tilde{n_l})}{(m_{1,1} + m_{1,2}\tilde{n_l})\tilde{n_0} + (m_{2,1} + m_{2,2}\tilde{n_l})}\,, \tag{2.6}$$

with $\tilde{n_l}$ and $\tilde{n_0}$ the complex refractive index of the last and first layer, respectively. In such a way one can fit the measured DR spectrum to the calculated one with $\epsilon_\infty$, $\omega_0$, $\gamma$ and $\beta$ as fitting parameters for each oscillator.

### 2.2.5 Macro-PL setup

PL and PLE as well as time-resolved PL measurements on the InGaN/Cn-ether PPV HIOS (chapter 3) were done with the FLS980 setup from Edinburgh Instruments. This instrument is a scanning PL spectrometer which allows for cooling and measuring time-integrated and -resolved PL. The time range spans from a few hundred ps up to ten seconds, depending on the excitation source. For time-integrated PL and PLE spectra, a continuous Xe-lamp is used. The wavelength is selected by a double monochromator. A glass plate reflects a small part of the excitation light onto a reference detector that is used for PLE measurements as $I_0$ and for correcting intensity fluctuations. The sample can be mounted in a closed-cycle helium (He) cryostat where it can be cooled down to around 25 K. Emitted light is dispersed by another monochromator and the light is detected by a photomultiplier tube. Other detector options are a microchannel plate (MCP) photomultiplier used for TCSPC since it shows faster response times and an NIR detector. PL decay transients can be measured either with interchangeable laser diodes for short decays in the 100 ps to 100 ns range by the TCSPC method or with a Xe-flash lamp for decays slower than $\approx 25$ µs using MCS. The wavelength is then selected by the same monochromator system as for time-integrated PL. Cooling down was done by evacuating the cryostat to $\sim 10^{-2}$ mbar. To ensure good thermal contact, a thin piece of aluminium foil was introduced between the holder and the sample and slight mechanical pressure was applied by the sample holder lid. The temperature was measured at the holder. At each temperature step, 5-10 minutes were waited in order to equilibrate the sample with the holder temperature.

### 2.2.6 Micro-PL setup

Additionally to the macro-PL setup described above, a micro-PL setup was used (figure 2.3). It consists of a microscope objective focusing the excitation light onto the sample. The excitation beam has a full-width at half maximum (FWHM) diameter of 1 µm for a 100x and 3 µm for a 20x objective, thereby setting the limit of lateral resolution. Four different excitation sources are available and can be selected by folding mirrors. A continuous wave (CW) laserdiode emitting at 440 nm (LDM440, Omicron Laserage), two CW/pulsed laserdiodes, emitting at

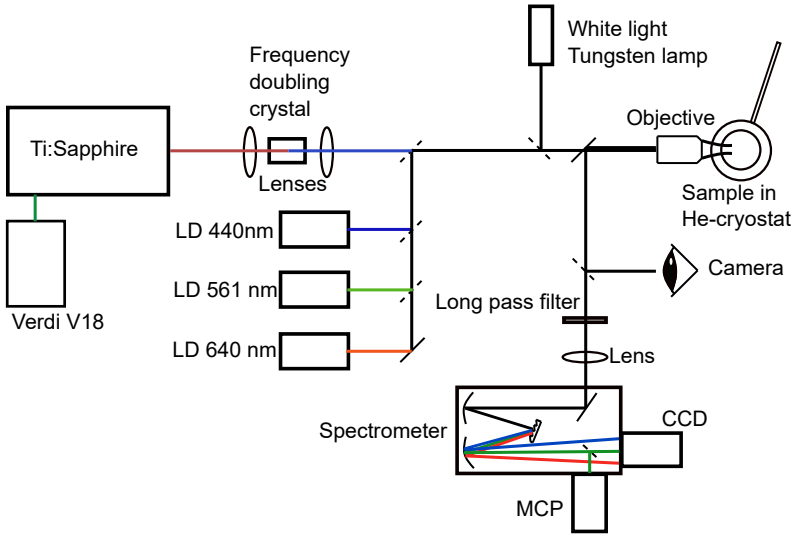


Figure 2.3: Schematic of the micro-PL setup.

561 nm and 640 nm (LDH series, Picoquant), and a mode-locked Ti:sapphire laser (Mira, Coherent). The Mira laser is tuneable between ∼700-950 nm and pumped by a laser emitting at 532 nm (Verdi V18, Coherent). The output of the Ti:sapphire laser is frequency doubled to match the absorption of the samples. The temporal FWHM of the laserdiodes is 70-90 ps while the one from the Ti:sapphire laser is below 200 fs. The sample can be mounted in a helium cooled cold-finger cryostat and measured under vacuum ($\sim 5 \cdot 10^{-5}$ mbar). The emission is collected by the same objective as for excitation and dispersed in a spectrograph (Acton SpectraPro 2500i). A liquid-nitrogen cooled CCD (Acton SPEC-10:100) can be used for collecting time-integrated PL and an MCP detector (Hamamatsu R3908) for recording PL decay curves. Light from the excitation is blocked by an appropriate long pass filter. A stabilised white light tungsten-halogen lamp (SLS201L, Thorlabs) is available in addition to the lasers. It is used together with a removable camera to identify TMDC monolayers and to measure DR spectra.

## 2.3 Transmission electron microscopy

Electron microscopy is a technique that uses electrons instead of light to construct an image. The electron's momentum $p$ corresponds to a de Broglie wavelength of $\lambda = h/p$ where $h$ is Planck's constant. Electrons can be accelerated in a static electric field so that after passing through that field $p = \sqrt{2eVm_0 + (eV/c)^2}$. Here, $V$ the potential difference, $m_0$ and $e$ the electron rest mass and charge and $c$ is the speed of light. Within this thesis, a transmission

electron microscope (TEM) was employed. It uses the transmitted electrons through a specimen for the image formation. Here, a value of $V = 200\,kV$ was used for the TEM images resulting in $\lambda = 2.5\,pm$ [35]. With the theoretical diffraction limited resolution of a microscope given by $\Delta x \approx 0.61\lambda/NA$ (NA is the numerical aperture) it becomes apparent that much smaller objects can be resolved in an electron microscope than in a light microscope for which $\lambda \approx 500\,nm$. The theoretical limit is lowered by imperfections of the electron lenses and lies at $\sim 0.2\,nm$ for the TEM used for the images presented within this thesis (TEM/STEM JEOL JEM2200FS). But it can also reach atomic resolution nowadays. Samples must be thin ($\sim 100$ nm) since electrons need to be transmitted through the specimen. This was done for the samples used here by sawing, lapping, mechanical polishing and Ar-ion milling. Energy-dispersive X-ray spectroscopy (EDXS) was used for the determination of the elemental distribution. In EDXS, the core electrons of the atoms building up the sample are excited by the impinging electron beam. The excited electron leaves a hole that can be filled by an electron of a higher energy shell. This will lead to the emission of X-rays whose energy is characteristic for a specific element and can thus be used to determine the elemental distribution of a sample.

TEM measurements were performed and analysed by Dr. H. Kirmse in the Structural Research and Electron microscopy group led by Prof. C. Koch.

## 2.4 Photoelectron spectroscopy

Photoelectron spectroscopy (PES) is a technique that allows determining the electronic structure of valence- and core-level electrons. It makes use of the photoelectric effect. Monochromatic UV light (UPS) of a few tens of eV or X-ray (XPS) radiation ($\sim 1$ keV) is used to probe the valence and core-level structure, respectively. The process of electron emission is usually described in a three-step process. Firstly, the photon is absorbed and creates an excited electron. Secondly, the electron travels to the sample surface where, as a third step, it is emitted into the vacuum [36]. The electrons emitted from the sample have a certain kinetic energy which is detected, for example, by a hemispherical electron energy analyser. If the electrons are only elastically scattered in the second step, then the measured kinetic energy is related to the photon energy $\hbar\omega$ by $E_{kin} = \hbar\omega - E_B - \Phi_s + (\Phi_s - \Phi_{det})$. Here, $\Phi_s$ and $\Phi_{det}$ is the sample and detector workfunction, respectively and $E_B$ is the binding energy of the electron referenced to $\Phi_s$. Sample and analyser are electrically connected so that they exhibit a common Fermi level. Inelastically scattered electrons contribute to a broad background which cuts-off at the energy related to electrons that have $E_{kin} = 0$ just after emission into the vacuum. This so-called secondary electron cut-off (SECO) contains direct information of $\Phi_s$ when $\Phi_{det}$ is known or calibrated with a metal of known workfunction [37]. A negative voltage is thus

applied to the analyser in order to collect these electrons. The electron momentum parallel to the sample surface is conserved during the photoemission process. It is related to $E_{kin}$ and the emission angle normal to the surface $\Theta$ by $k_{\parallel} = \frac{\sqrt{2m_0 E_{kin}}}{\hbar} sin\Theta$. So, by measuring $E_{kin}$ in dependence of $\Theta$, one can determine the electronic band dispersion as done in angle-resolved PES. UPS measures the occupied valence electron states. To gain insight into the unoccupied states close to the Fermi level, inverse photoelectron spectroscopy (IPES) is applied. Electrons are sent onto the sample where they can relax to a lower lying state under the emission of light of a certain energy related to the energy of unoccupied electron states above the Fermi level.

Within this thesis, UPS was performed with a He-discharge lamp (21.2 eV) and XPS with a Mg X-ray anode emitting at 1253.6 eV at a Phoibos-100 spectrometer or a JEOL JPS-0930 with the Al K$\alpha$-line (1486.6 eV). IPES and UPS were measured also angle-resolved to probe the $\Gamma$- and $K$- point of monolayer TMDCs. Details can be found in [38, 39].

PES measurements were performed and analysed by Dr. S. Park and Dr. T. Schultz in the Supramolecular Systems group led by Prof. N. Koch.

## 2.5 Raman spectroscopy

Raman spectroscopy is used to probe vibrational modes of molecules or atoms in the solid state. Its principle is depicted in figure 2.4. The system is optically excited by a laser beam of

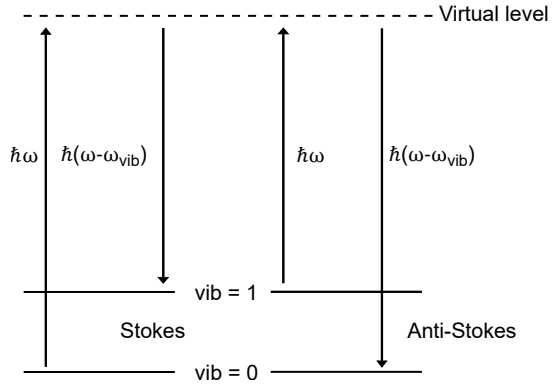


Figure 2.4: Sketch of the principle of Raman scattering with *vib* denoting the vibrational level and $\hbar\omega$ is the energy of the exciting laser. Redrawn after [40].

energy $\hbar\omega$. When relaxing back, it can occur that the system is left in a vibrational state of the ground state. The light emitted in the relaxation process is hence shifted by the energy of the vibrational state compared to the excitation laser, i.e. $\hbar\omega_{em} = \hbar\omega - \hbar\omega_{vib}$. On the other hand, the system might already be in a vibrational state before excitation and relax into the ground state after it was excited. This will lead to a shift of the emission to higher energies:

$\hbar\omega_{em} = \hbar\omega + \hbar\omega_{vib}$. These two processes are called Stokes and anti-Stokes scattering while the elastic process is termed Rayleigh scattering [40]. A sharp cut-off filter blocks the excitation light $\hbar\omega$ since the Raman emission is much weaker than the elastically scattered laser light. In this thesis, the Raman spectra were obtained with an XploRA Raman microscope from Horiba with an excitation energy of 2.33 eV.

Raman spectra were recorded and analysed by Dr. N. Severin in the group Physik von Makromolekülen led by Prof. J. Rabe.

## 2.6 Photocurrent action spectroscopy

In photo current action spectroscopy (PAS), the current of a photodetector is measured in dependence of the energy and intensity of the incident illumination. Absorbed light will generate electron-hole pairs that can dissociate into free carriers, for example, by an external or internal bias. Therefore, they can contribute to an increase in current. In first approximation, the photocurrent will be proportional to the absorption of the active region of the photodetector and linear in the excitation light intensity [2]. Within this thesis, PA spectra were acquired by exciting with a tungsten/halogen lamp (Spectral Products ASBN-W 150F-L). Wavelength selection was done with a dual grating monochromator (Digikröm CM110). The excitation light was modulated by a chopper and the photocurrent was pre-amplified (Femto, DLPCA 200) and measured with a Lock-in amplifier (Perkin 7265 DSP). The light intensity was $< 0.1$ mW/cm$^2$.

PAS measurements were done and analysed by Dr. S. Dalgleish in collaboration with the group of Prof. L. Reissig at the FU Berlin.

# 3 FRET between an InGaN/GaN quantum well and the polymer Cn-ether PPV

*The following chapter is based on the publication* Energy Transfer between Cyano-Ether PPV and InGaN/GaN Quantum Wells with Large Piezoelectric Fields [41] *by N. Mutz, H. Kirmse, C. T. Koch, E. J. W. List-Kratochvil and S. Blumstengel. The author wrote the manuscript, conducted and analysed all the experiments except STEM and EDXS. These were performed and analysed by H. Kirmse and C. T. Koch. Band structure calculations were done by the author using the free 1D Poisson and Schrödinger solver by Gregory Snider [42]. E. List-Kratochvil, S. Blumstengel and N. Mutz planned the experiments and interpreted the data. All authors contributed to the final manuscript. Additionally to the data presented in the publication, more details are given on the PL properties of the individual constituents and the derivation of the transfer efficiencies.*

This chapter focuses on Förster resonance energy transfer (FRET) from a planar inorganic single InGaN quantum well (QW), embedded in GaN, to the organic polymer Cn-ether PPV. The two components are chosen under the aspect of using the technologically and economically relevant class of GaN-materials as the inorganic part of the hybrid system. GaN and its alloys AlGaN and InGaN find widespread application in solid state lighting as light-emitting diodes. The combination with an organic counterpart to form the hybrid inorganic/organic system (HIOS) therefore enables the implementation into an existing industrial design. In reality, modern LEDs consist of several layers including the emission layer and p- and n-doped regions which sandwich the emission layer. For FRET to be active and efficient, the emission layer of the LED must be separated from the organic acceptor layer only by a few nanometres. This can either be achieved by a thin capping layer or by structuring the existing LED into pillars with the emissive layer being exposed. Both methods are challenging to realise. In the case of the thin capping layer, it needs to be doped to allow the formation of the p-n junction and still be of acceptable quality to minimise surface related defects and enable current flow. The etching of already existing LEDs into pillars circumvents this challenge, but is not easily done. Additionally, the etching can induce damage to the active area, the acceptor material has to

be deposited on the sidewalls of the pillars and more elaborate ways of electrical contacting are needed. As a third possibility, the organic acceptor can be incorporated monolithically in the p-n diode which can be done, for example for ZnO [43], but is not possible for GaN due to its high growth temperatures.

Despite these challenges, fundamental research was already devoted to the demonstration and understanding of FRET in the first two of the above described systems. FRET was investigated from planar GaN-based QWs either to inorganic nanocrystals [44, 45] or organic polymers [8–10, 46]. Structured QWs, on the other hand, were used in [47, 48]. Also, attempts were made to incorporate the FRET scheme into electrically driven LEDs as a means of colour down-conversion to achieve white light emission [47, 49, 50]. Although the cited work showed that FRET is feasible in these systems, by mainly observing a shortening of the QW decay time, it was not concerned with the enhanced light emission from the acceptor layer. A higher external quantum efficiency in the combined system, compared to purely radiative excitation of the colour converter, is required for the FRET scheme to be effectively implemented. On a more physical level, the high internal electric fields in c-plane GaN - stemming from spontaneous and piezoelectric polarisation - might hinder efficient FRET. Due to these fields, the wavefunction overlap between electron and hole is reduced influencing the FRET rate. This issue was raised by Itskos *et al.* [13]

Both of these concerns are looked at in this chapter. A single planar InGaN/GaN QW served as the donor and Cn-ether PPV, a derivative of poly(*p*-phenylene vinylene) (PPV), as the acceptor. The commercially purchased QW possessed high internal electric fields, on the order of MV/cm. Still, efficient FRET is observed at cryogenic temperatures. An enhancement of the Cn-ether PPV light emission is found in PL excitation (PLE) experiments when compared to a purely radiative process. The competition between the different decay channels in the QW is monitored by following the temperature dependence of the FRET rate. From around 130 K on, the decay of the excited states is dominated by non-radiative transitions, beating the radiative and FRET channels in the examined system. These findings highlight the advantages of FRET as a means of efficient colour conversion while it also shows the requirements set to the quality of the QW donor.

Next, it follows a description of the organic and inorganic components, their properties and fundamental interactions required for understanding the experimental findings. The subsequent section covers the experimental results and their discussion. The last part gives a summary of the findings and puts them into perspective.

## 3.1 Fundamentals

This section is started with a short introduction to the class of GaN materials focusing on the internal electrical field. The concept of calculating the energy bands of the InGaN/GaN single quantum well using the Schrödinger and Poisson equation is shortly summarised. Furthermore, the influence of the electric field on the quantum well excitons is highlighted. Subsequently, the organic counterpart - Cn-ether PPV - is discussed followed by a short review regarding Förster-like resonance energy transfer.

### 3.1.1 Gallium Nitride

Gallium nitride (GaN) is a III-V semiconductor compound which can be grouped together with the other III-nitride semiconductors aluminium nitride (AlN) and indium nitride (InN). All three semiconductors have a direct band gap with gap energies of 0.78 eV for InN, 3.44 eV for GaN and 6.13 eV for AlN [51, 52]. Furthermore, it is possible to tune the band gap in this class of materials by forming ternary and quaternary alloys. Type I heterostructures can be formed, enabling the design of quantum wells where charge carriers are accumulated. Together with the possibility of p- and n-doping the III-nitrides, they form the basis of efficient blue to ultraviolet light emitting diodes, with nowadays reaching the green colour spectrum. This achievement was awarded the Nobel-prize in 2014. Interestingly, GaN-materials and in particular InGaN/GaN QWs show a high density of structural imperfections, like threading dislocations on the order of $10^8 - 10^9$ cm$^{-2}$ [51, 53]. In spite of this high value as compared to, for example, red-emitting LEDs which have an around three orders of magnitude lower dislocation density, LEDs based on GaN still show a surprisingly high efficiency [54]. This observation is attributed to the small carrier mean-free path caused by strong carrier localisation [55–58].

The III-nitride semiconductors crystallise in zinc-blende or wurtzite structure where the wurtzite structure is found at room temperature. The structure is shown in figure 3.1 together with the band gap energies of the three materials over their lattice constants. It can be seen that the in-plane lattice constant for GaN and AlN are similar, while it differs by more than 10 % for InN and GaN when grown in the direction of the c-lattice vector. As a consequence, the growth of InN/GaN heterostructures is accompanied by strain that leads to a piezoelectric polarisation. Additionally, the non-centrosymmetric nature of the Wurtzite crystal lattice gives rise to spontaneous polarisation. Both polarisations will induce charges resulting in high internal electric fields on the order of a few hundred kV/cm up to a few MV/cm [60]. In InGaN/GaN QWs, these electric fields lead to a tilting of the valence and conduction band. As a consequence, electron-hole pairs in the QW will be spatially separated. Correspondingly, the wavefunction overlap between electron and hole is reduced leading to a smaller probability for

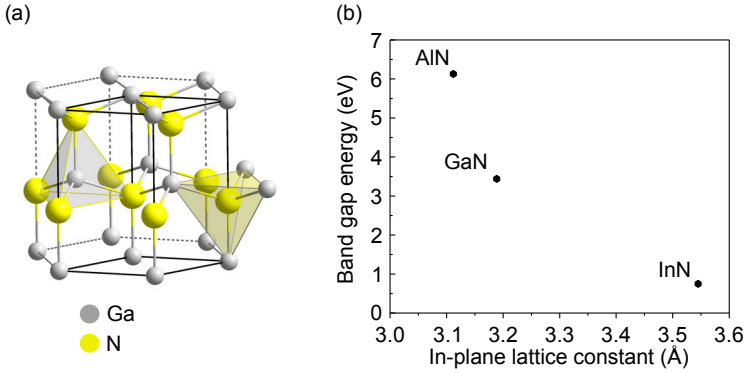


Figure 3.1: (a) Wurtzite crystal structure of GaN (from [59]). (b) The band gap energy of the III-nitrides in comparison to the respective in-plane lattice constant (values taken from [51]).

radiative recombination. Electron and hole are shifted in energy in opposite directions resulting in an overall red-shift of the optical transition. This phenomenon is termed Quantum-confined Stark effect (QCSE) and shown in figure 3.2.

The polarisation charges can be calculated for $In_xGa_{1-x}N$ as follows [61]:

$$\begin{aligned} P^{sp}_{In_xGa_{1-x}N} &= -0.042x - 0.034(1-x) + 0.038x(1-x)\,, \\ P^{pz}_{In_xGa_{1-x}N} &= x(-1.373b + 7.599b^2) + (1-x)(-0.918b + 9.541b^2)\,, \end{aligned} \tag{3.1}$$

whereas $b(x) = [a_{subs} - a(x)]/a(x)$ is the basal strain. Therein, $a_{subs}$ is the in-plane lattice constant of the substrate and $a(x) = (0.31986 + 0.03862x)\ nm$ for $In_xGa_{1-x}N$. From these polarisation charges one can obtain the sheet charges at the GaN/InGaN interface *via* $\sigma_{sheet} = [(P^{sp}_{GaN} + P^{pz}_{GaN}) - (P^{sp}_{InGaN} + P^{pz}_{InGaN})]/e$ with $e$ the electron charge.

If the material parameters and the interface charges of the quantum well are known, its energy levels as well as electron and hole wavefunctions can be calculated. For this, the Schrödinger and Poisson equations have to be solved self-consistently. Here, the procedure by Tan *et al.* is cited [62]. The time-independent Schrödinger equation for one electron with the wavefunction $\psi(x)$ in one dimension is given by

$$-\frac{\hbar^2}{2}\frac{d}{dx}\left(\frac{1}{m^*(x)}\frac{d}{dx}\right)\psi(x) + V(x)\psi(x) = E\psi(x)\,. \tag{3.2}$$

Here, $m^*(x)$ is the electron effective mass, $V(x)$ the potential and $E$ the energy. Since the potential $V(x)$ depends on the electron distribution $n(x)$ through the electrostatic potential $\phi(x)$, the Schrödinger equation is coupled to the Poisson equation:

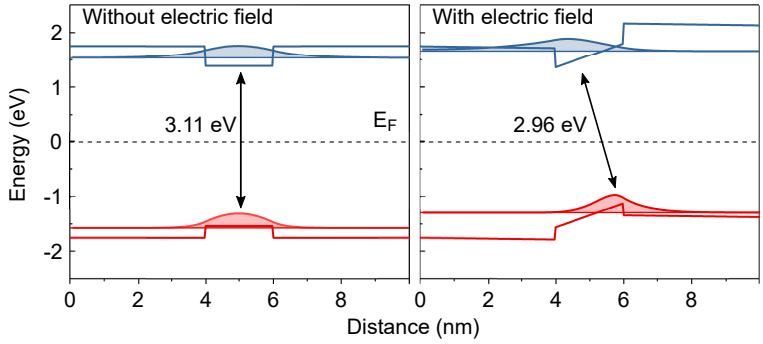


Figure 3.2: Effect of the polarisation fields on the band structure of an InGaN/GaN quantum well. The electric fields lead to a tilting of the conduction and valence band resulting in a decrease in transition energy and a reduced wavefunction overlap. For the calculations, an indium content of 0.15, a well width of 2 nm and no doping were used.

$$\frac{d}{dx}\left(\epsilon(x)\frac{d}{dx}\right)\phi(x) = \frac{-e(N_D(x) - n(x))}{\epsilon_0}\,, \tag{3.3}$$

with $\epsilon$ the dielectric constant, $\epsilon_0$ is the vacuum permittivity and $N_D$ the concentration of ionised donors. Therefore, equation 3.2 and 3.3 need to be solved iteratively. In the present study this was done by using the numerical software provided by Gregory L. Snider [42].

### 3.1.2 Cn-ether-PPV

The polymer poly[oxa-1,4-phenylene-1,2-(1-cyano)-ethenylene-2,5-dioctyloxy-1,4-phenylene-1,2-(2-cyano)-ethenylene-1,4-phenylene] (Cn-ether PPV) was chosen in this study as acceptor since its absorption spectrally overlaps with the emission of the InGaN/GaN QW used here. This is a prerequisite for Förster-like resonance energy transfer as will be discussed in the next part. Its relatively high photoluminescence (PL) quantum yield (45%) in the solid state makes it furthermore an interesting counterpart for the QW. For low PL quantum yield (QY), the transferred excitons would otherwise be lost non-radiatively in the acceptor. Additionally, Cn-eth PPV shows good solubility in organic solvents making it possible to easily spin coat thin films from solution on top of GaN.

Cn-ether PPV is a derivative of poly(*p*-phenylene vinylene) (PPV). PPV was a promising candidate as emitter in polymer-based organic light emitting diodes. In 1990, electroluminescence was shown for a PPV based device [63]. PPV itself is insoluble, therefore, side-chains were introduced, for example in the so-called MEH-PPV (Poly[2-methoxy-5-(2-ethylhexyloxy)-1,4-phenylene vinylene]). The introduction of cyano-groups at the vinylene units (Cn-PPV)

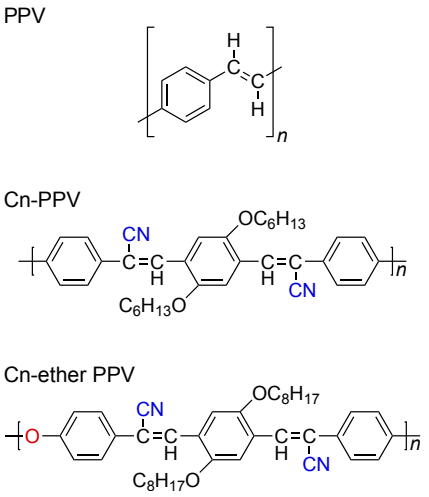


Figure 3.3: Three different derivatives of PPV. The structure of Cn-PPV is the one given by [69]. The PPV investigated in this thesis is depicted as the third derivative, Cn-ether PPV. The cyano and ether groups are highlighted in blue and red, respectively.

increases the electron affinity, making it possible to use more stable electrodes like aluminium instead of calcium as cathode in an OLED structure [64, 65]. Segmenting PPV into distyrylbenzene units by incorporating an ether group as the linker (Ether-PPV) led to a PPV derivative which showed photoconductivity and high PL quantum yield [66, 67]. The combination of both cyano groups and ether linkage promised an increased electron affinity together with a high PL quantum yield and good solubility in organic solvents [68].

The lowest optical absorption in PPV is attributed to an excitation between occupied $\pi$- and unoccupied $\pi^*$-orbitals with the generation of neutral excitons [70, 71]. Unlike in PPV, the main contribution to the emission in Cn-PPV was found to be structureless and considerably red-shifted, compared to measurements in solution [72–74]. In addition, its PL decay time was observed to be longer in the film. This led to the conclusion that emission in Cn-PPV is mainly due to an interchain excitation, instead of an intrachain exciton. Interestingly, Cn-PPV still showed a high PL quantum yield of 0.35 compared to 0.27 for unsubstituted PPV in the film. It was put forward that the polymer chains closely pack parallel in Cn-PPV with a calculated distance of 3.4 Å to each other [75]. The small distance then leads to an increased emission probability of the interchain species. Chasteen *et al.* investigated the difference between Cn-PPV and Cn-ether PPV with the result that the optical properties of both PPV derivatives are similar [69]. It was found that emission and absorption spectra of Cn-PPV and Cn-ether PPV were comparable in solution but were blue-shifted in the ether linked PPV as compared to Cn-PPV. This effect was attributed to the broken conjugation of the polymer backbone

through the ether group. A long decay time of 14 ns was found in the film for the dominant emission in Cn-ether PPV together with a shorter one of 6 ns. In conjunction with a measured high PL quantum yield of 0.45 this led to the conclusion that the emission is stemming from a dominant interchain excitation (longer decay time, 69 % contribution) with contribution of an intrachain exciton (shorter decay time, 31 % contribution). The broken conjugation was interpreted to hinder excitation migration to quenching sites making the small radiative decay rate competitive to the, in this way, reduced non-radiative decay rate.

### 3.1.3 FRET

An excited species, such as an exciton, can transfer its energy to another species in its respective ground state. The excited species is, therefore, called donor while the one in the ground state is termed acceptor. An interaction between donor and acceptor needs to exist for this process to happen. When considering the Hamilton operator of the donor-acceptor pair, this can be written as:

$$\hat{H} = \hat{H}_D + \hat{H}_A + \hat{V}_{DA} \,, \tag{3.4}$$

with $\hat{H}_D$ and $\hat{H}_A$ being the Hamilton operator of the isolated donor and acceptor, respectively, and $\hat{V}_{DA}$ a small perturbation describing the coupling between donor and acceptor. The donor is taken to be in the excited state while the acceptor is in the ground state. So far, the description is equivalent to a coupled two-level system. In case that the interaction is an oscillatory function, such as an electromagnetic field, the probability of finding one state in its excited state and the other one in its ground state will oscillate between these two. This is called coherent (or strong) coupling since the phase between the incident electric field and the coupled states is preserved. Usually, the acceptor (and also the donor) does not have its excited state at exactly one energy but it is spread around this value with a width of $\Delta E$ around $E_0 = \hbar\omega_0$ where $\omega_0$ is the transition frequency of the excited donor. This corresponds to a situation of coupling between a discrete initial state and a quasi-continuum of final states. The transition rate can be calculated by Fermi's golden rule [76]:

$$\Gamma = \frac{2\pi}{\hbar} \left| \langle \psi_A^* \psi_D | \hat{V}_{DA} | \psi_A \psi_D^* \rangle \right|^2 \rho(E_A = E_D) \,, \tag{3.5}$$

whereas $\langle \psi_A^* \psi_D | \hat{V}_{DA} | \psi_A \psi_D^* \rangle$ is the transition matrix element from the initially excited donor to the acceptor where the asterisk denotes the excited state. $\rho(E_A = E_D)$ is the density of states of the acceptor at the energy of the donor. In the limit that the width of the final states $\Delta E$ is small compared to the coupling $V$, then an (exponentially damped) coherent

coupling is recovered. In the opposite case, one speaks of incoherent (or weak) coupling. The loss in coherence can, for instance, be caused by a statistical energy distribution or vibrational coupling in the acceptor [76]. This will be the situation considered from now on.

Coming back to the specific case of an excited donor and an acceptor in its ground state, we are looking at processes of the sort $|\psi_A\psi_D^*\rangle \rightarrow |\psi_A^*\psi_D\rangle$. In order to calculate the transfer rate 3.5, the interaction $V_{DA}$ in the Hamilton operator 3.4 needs to be specified. For spatially separated donor and acceptor with large distance between them, compared to the extension of their respective charge distributions, the interaction can be approximated by considering point dipoles [71]:

$$\hat{V}_{DA} = \frac{q_D q_A}{4\pi\epsilon_0}\frac{\hat{d}_D\hat{d}_A}{R^3}\overbrace{(cos\Theta_{DA} - 3cos\Theta_D\cos\Theta_A)}^{=\kappa} . \tag{3.6}$$

The derivation of this expression is based on the energy of a dipole in an electric field $U = -q_A\mathbf{d}_A\cdot\mathbf{E}_D$ and the electric field produced by an electric dipole, $\boldsymbol{E}_D = \frac{3(q_D\boldsymbol{d}_D\cdot\boldsymbol{r_0})\boldsymbol{r_0}-q_D\boldsymbol{d}_D}{4\pi\epsilon_0 R^3}$. $q_D$, $d_D$ and $q_A$, $d_A$ are the charge and the distance of the donor and acceptor dipole, respectively [77]. $\boldsymbol{r} = \boldsymbol{r_0}R$ is the vector between donor and acceptor with the length R. The angles $\Theta_{DA}$, $\Theta_D$ and $\Theta_A$ are as defined in figure 3.4 and give the relative orientation of the two dipoles to one another. The above describes that the polarisation of the excited donor produces an electric field that induces a polarisation in the acceptor, therefore lifting it to an excited state.

Inserting 3.6 into 3.5 yields the following for the transfer rate:

$$\Gamma = \frac{1}{2\epsilon_0\hbar}\frac{|\mu_d|^2|\mu_a|^2}{R^6}\kappa^2\rho(E_A = E_D) , \tag{3.7}$$

with the dipole moments of the donor and acceptor defined as $\mu_d = q_D\langle\psi_D|\hat{d}_D|\psi_D^*\rangle$ and $\mu_a = q_A\langle\psi_A^*|\hat{d}_A|\psi_A\rangle$, respectively. As can be seen from the above equation, the transfer rate in this approximation is proportional to the square of the dipole moments of the donor and acceptor, their orientation and inversely proportional to the sixth power of the distance between donor and acceptor. In the present study, an InGaN/GaN QW is used as the donor. As discussed above, large internal electric fields can exist in these structures which will lead to a reduction of the electron-hole wavefunction overlap and, thus, to a reduced $\mu_d$ [13]. Therefore, the FRET rate will be reduced. Additionally, spectral overlap between donor emission and acceptor absorption is required through the density of states $\rho(E_A = E_D)$. This condition determines that the donor emission needs to be overlapping with the acceptor absorption spectrum for efficient FRET. It can be translated into the spectral overlap integral $J = \int I_D(\lambda)\epsilon_A(\lambda)\lambda^4 d\lambda$ where $I_D(\lambda)$ is the normalised donor emission spectrum and $\epsilon_A(\lambda)$ is the molar extinction coefficient of the acceptor [71]. The above relation was derived by Förster in 1948 and can be

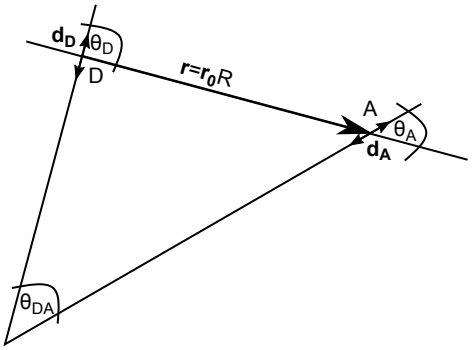


Figure 3.4: On the definition of the angles and vectors used in equation 3.6. D stands for the donor while A represents the acceptor (after [71]).

correlated to measurable quantities [78]. Hence, this kind of transfer is called Förster resonance energy transfer.

The restriction to an interaction of point dipoles is not always given. An extension to different geometries, like a sheet of dipoles, and Wannier-Mott excitons instead of Frenkel excitons, was given by Agranovich *et al.* [3, 79, 80]. The alterations made showed that the distance dependence of the transfer rate was modified as well as a dependence on the wavenumber of the Wannier-Mott exciton was found. Due to the localisation of excitons in the InGaN QW at cryogenic temperatures, this situation is similar to studies with ZnO QWs where a $1/R^4$-dependence of the FRET rate was found [4]. This corresponds to the interaction of a point dipole with a planar sheet of acceptors. Finally, it is noted here, that at close separation electrons can be exchanged between donor and acceptor, as worked out by Dexter [81]. The transfer is again accompanied by an excitation of the acceptor through the donor. But its rate is exponentially decaying with donor-acceptor separation, due to the requirement of wavefunction overlap [71]. While Förster resonance energy transfer is active over a few nanometres, Dexter transfer is only efficient at distances smaller than one nm. The InGaN/GaN QW investigated has a GaN cap with 4 nm thickness so that Dexter transfer does not need to be considered here.

## 3.2 Results and Discussion

In this section, the experimental results and analysis are presented. The first two subsections are devoted to the characterisation of the two individual components while the combined hybrid system is described in the third subsection.

### 3.2.1 Quantum well structure

The used InGaN/GaN single quantum wells were commercially purchased from the company Novagan and non-intentionally doped. To calculate the internal electric field and to confirm a thin GaN capping layer, transmission electron microscope (TEM) analysis and electron dispersive X-ray spectroscopy (EDXS) was performed to obtain the geometrical parameters and elemental distribution. The TEM cross section is shown in figure 3.5, together with the indium and gallium distributions. Indium is restricted to the quantum well. Therefore, its thickness can be determined as the region in which indium can be detected. The thickness is thus found to be 4 ± 1 nm. The same thickness is extracted for the top GaN layer, verifying a short distance between the later donor and acceptor in the hybrid system.

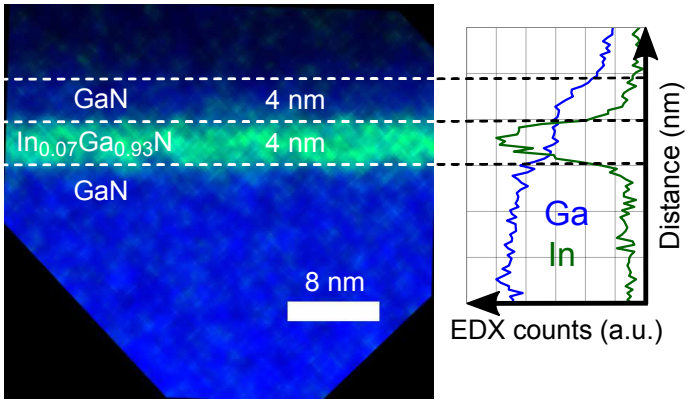


Figure 3.5: TEM scan and EDX spectroscopy of the single InGaN/GaN QW. The gallium and indium content are displayed in blue and green, respectively. An indium content of 0.07 was derived together with a top cap thickness and quantum well width of 4 nm each. Modified from [41].

Figure 3.6 shows the PL and PLE of the InGaN/GaN QW at a temperature of 30 K. At 30 K the PL spectrum is dominated by a single peak at 2.49 eV with phonon replica 90 meV lower in energy corresponding to the longitudinal optical phonon energy [51]. A sharp increase of PL intensity is observed at 3.49 eV in the PLE spectrum matching the GaN band gap energy. PL emission for excitation energies lower than this correlate to selective absorption in the quantum well. The QW absorption is broad and covers a range of about 500 meV. Additionally, the Stokes shift of 300 meV between emission and absorption is very large. A correlation between broad QW absorption together with increasing Stokes shift for increasing QW width is found in literature [82, 83]. This can be explained by the localisation of electron and hole on different sides of the QW.

The energy of the PL peak can be compared with the expected transition energy as extracted

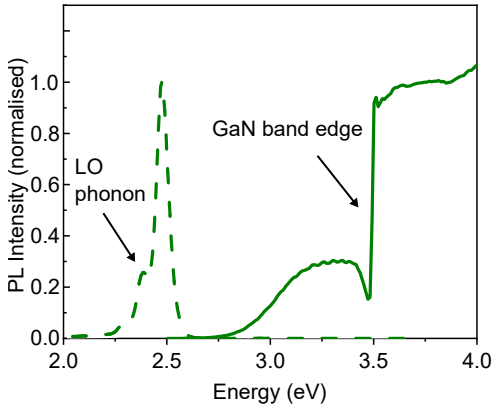


Figure 3.6: PL and PLE of a QW reference at 30 K. The LO phonon replica and the GaN band edge are highlighted.

from the calculated energy band diagram. Extracting the QW composition can be done by evaluating the Ga-K$\alpha$ integrated intensities in the EDX spectra. The composition is found to be $In_{0.07}Ga_{0.93}N$ by looking at the intensities of the GaN-only region and the InGaN QW. These parameters can be combined with literature values to calculate the energy band diagram of the QW region [52, 84]. Figure 3.7 shows the results of solving the Schrödinger and Poisson equation self-consistently. Using 3.1 and assuming fully relaxed GaN layers, an electric field of 316 kV/cm is deduced from the polarisation charges. An energy difference of 3.26 eV between the lowest electron and hole states is found from the calculations. In addition to the polarisation fields in the quantum well, there exists an electric field in the GaN surface depletion layer. The width of the depletion layer can be estimated as [85, 86]:

$$w = \sqrt{\frac{2\Delta V \epsilon \epsilon_0}{e^2 N_D}} \approx 220\, nm\,, \tag{3.8}$$

where $\Delta V$ is the potential drop from the surface to the bulk, $\epsilon = 10$ is the dielectric constant of GaN and $N_D = 10^{16}\, cm^{-3}$ is the donor concentration typical for unintentionally doped GaN [51, 87]. $\Delta V = 0.45\, eV$ was taken as the value for surface band-bending from experiments [88]. Therefore, the surface depletion layer extends well above the QW region giving rise to an electric field at the surface of $F_{depl,surf} = eN_d w/\epsilon\epsilon_0 \approx 40\, kV/cm$. This value is still too small to explain the difference between calculated and observed transition energies. Also, the exciton binding energy (≈25 meV in GaN) and a Stokes shift on the order of 0.1 eV, typically found in InGaN/GaN QWs, cannot explain this discrepancy [89, 90]. No unusual indium or well width fluctuations were observed in TEM which would lead to locally smaller transition energies.

In literature, usually an indium content of around 0.18 gives a similar PL response as seen in

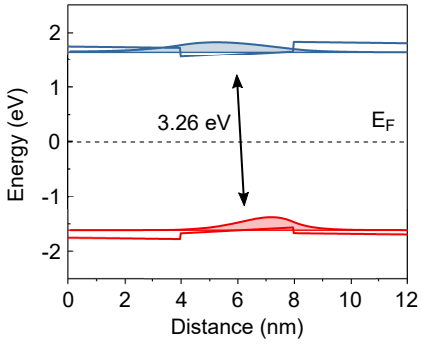


Figure 3.7: Calculated band diagram with the obtained values from TEM analysis. The transition energy is given by the arrow. No doping and relaxed GaN layers were assumed.

the present sample [82, 83]. Therefore, it is concluded that larger internal electric fields need to exist in the InGaN/GaN quantum well, similar to the ones for higher indium content. The estimation of the transition energy given above does not include any additional piezoelectric contribution from the GaN capping layer. This is possibly caused by strained growth of GaN on the InGaN slab. It also needs to be noted that $N_d$ assumed here was not given by the manufacturer leading to a level of uncertainty in $F_{depl,surf}$. Already an unintentional donor density of $N_d = 10^{17}$ will give rise to an order of magnitude higher electric field in the depletion layer while it still affects the near-surface quantum well. Since no insight in the growth process of the QW is given, a more detailed picture of the origin of the unusually high internal electric field with respect to the indium content cannot be given. From PL spectroscopy it can be inferred that the total electric field in the QW needs to be around 1-2 MV/cm and is, most likely, to a large extend owed to the close proximity of the QW to the surface in the studied sample.

The electron-hole wavefunction overlap and, therefore, the probability to decay radiatively is reduced as a consequence of the large internal electric field. In the optical spectra, this manifests itself in a pronounced temperature dependence of the QW PL. At 30 K the PL spectrum is dominated by a single peak at 2.49 eV (figure 3.8). When increasing the temperature, the PL intensity of the QW emission drops significantly and already at 180 K almost no emission stemming from the QW is observed any more. Instead, an emission related to defects becomes the most dominant one at around 2.2 eV. At room temperature and under low excitation intensity, the defect emission is the only one detectable. For higher excitation intensities the defect emission saturates and the QW emission becomes visible. Since PLE measurements were made under low excitation intensities, all other measurements were performed at these conditions, restricting the accessible temperature range to lie between 30 K and 130 K. For these low temperatures, the non-radiative decay rate is reduced and becomes small enough so

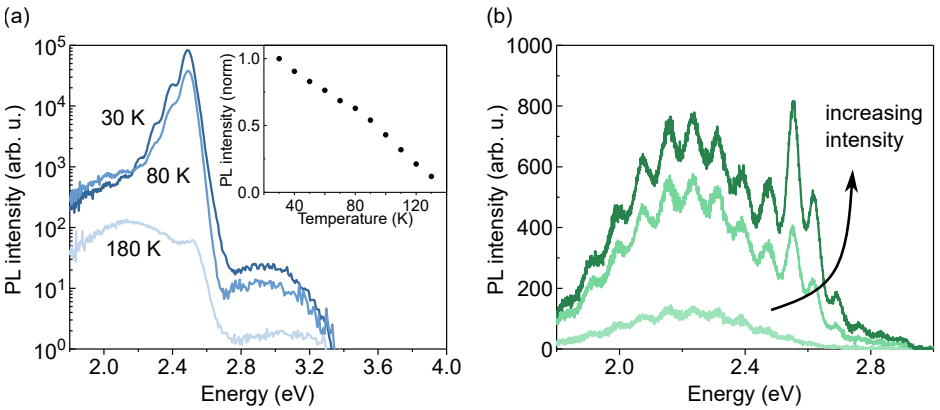


Figure 3.8: (a) Temperature dependence of the PL signal. The defect emission around 2.2 eV becomes dominant at 180 K. The inset shows the integrated QW PL intensity between 30 and 130 K normalised to the lowest temperature. (b) PL signal in dependence on the excitation intensity at room temperature. Defect emission is observable around 2.2 eV. The QW PL at 2.5 eV is visible for higher excitation intensities only. The oscillations in this case are due to Fabry-Perot interferences.

that an optical signal stemming from the QW can be recorded.

A small radiative decay rate will also manifest itself in a long PL decay time at low temperatures. This is shown in figure 3.9. The PL decay measured at the peak position is non-exponential, which is typical for InGaN QWs and caused by carrier localisation [91]. To determine an effective decay time, the transients were fitted with a three-exponential decay and the average decay time was calculated:

$$< \tau >= \frac{\int_0^\infty tI(t)}{\int_0^\infty I(t)} \, . \tag{3.9}$$

Here, $< \tau >$ is the average decay time and $I(t)$ is the PL decay. The QW shows a long average PL decay time of $13.2 \pm 0.7$ µs at 30 K. A shortening of the PL decay time can be observed for increasing temperatures with a decay time of $1.20 \pm 0.08$ µs at 130 K which is depicted in the inset.

By assuming a quantum yield of $\eta_{QW}(T = 30K) = 1$ the radiative and non-radiative decay rates can be determined relative to the temperature at 30 K. The PL quantum yield is defined as the probability of a radiative transition from the excited to the ground state in comparison to the sum of all transitions. The total probability of a decay to happen per unit time is experimentally accessible in the form of the PL decay rate, i.e. the inverse of the measured PL decay time.

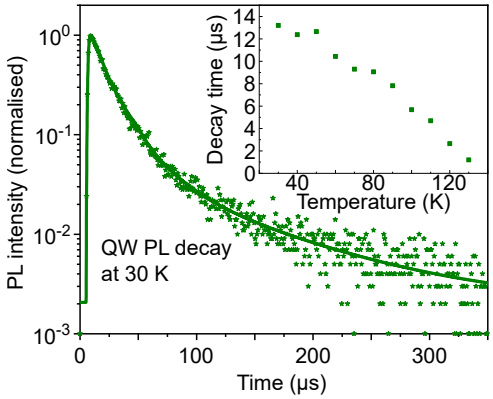


Figure 3.9: PL decay of the InGaN/GaN QW at 30 K. The emission was recorded at 2.49 eV and the excitation energy was 3.76 eV. Plotted in the inset is the dependence of the decay time on the temperature.

$$\eta_{QW} = \frac{\Gamma_{rad}}{\Gamma_{tot}} = \frac{\Gamma_{rad}}{\Gamma_{rad} + \Gamma_{nrad}} = \frac{1/\tau_{rad}}{1/\tau_{rad} + 1/\tau_{nrad}} \,. \tag{3.10}$$

Here, $\Gamma_{rad}$, $\Gamma_{nrad}$ and $\Gamma_{tot}$ are the radiative, non-radiative and total decay rate, respectively while $\tau_{rad}$ and $\tau_{nrad}$ are the radiative and non-radiative decay times. The inset of figure 3.8(a) depicts the integrated PL intensity in dependence of the temperature for the investigated QW. With increasing temperature, non-radiative decay channels become active. In consequence, the PL QY and therefore PL intensity drops significantly.

To summarise, the optical properties of the investigated QW are dominated by the large internal electric field. Together with a relatively large QW thickness of 4 ± 1 nm, this manifests itself in a large Stoke's shift, long PL decay time and decreasing PL quantum yield with increasing temperature. Since the FRET rate is proportional to the squared dipole matrix moment element of the donor species, a reduced electron-hole wavefunction overlap will influence the FRET rate. This issue will be further elaborated in the remaining chapters.

### 3.2.2 Cn-ether PPV

Cn-ether PPV was received by the courtesy of H.-H. Hörhold and used as-is. For optical measurements, the polymer was dissolved in toluene and spin coated onto a sapphire substrate in a glovebox. Exposure to ambient air was kept to a minimum of around five minutes when mounting the sample and evacuating the measurement cryostat for PL measurements. The room temperature absorption and emission spectra of Cn-ether PPV as a thin film are shown in figure 3.10(a). The absorption features two distinct peaks at 2.7 eV and 3.3 eV. The lower transition corresponds to the vibrationally unresolved $S_1 \leftarrow S_0$. The spectra are comparable

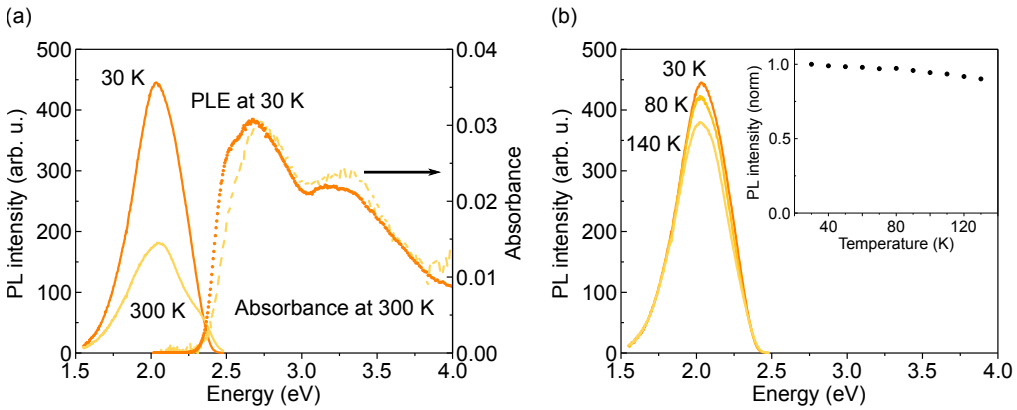


Figure 3.10: (a)PL and absorption (broken lighter orange line) and PL and PLE (dotted orange) spectra of a thin Cn-ether PPV film on sapphire at room temperature and 30 K, respectively. The PL is peaked at 2.03 eV. (b) Temperature evolution of the PL spectrum at 30, 80 and 140 K. The inset shows the integrated PL intensity over the temperature, normalised to 30 K. The film thickness was 4–5 nm.

to literature for Cn-ether PPV which is similar to other PPV derivatives, like Cn-PPV or MEH-PPV [69, 71, 72]. The PL spectrum peaks at 2.03 eV, is broad and does not show a considerable structure. As mentioned in the earlier chapter 3.1.2, the emission is attributed to be mainly due to an interchain excitation. An additional peak is observable at around 2.35 eV and was interpreted by Yin *et al.* as the intrachain exciton [92]. Upon cooling to 30 K, the overall PL intensity grows approximately two times as compared to room temperature. The higher energy PL peak is seen to vanish. Otherwise, the spectrum at 30 K is very similar to the room temperature spectrum without any signatures of vibronic progression. It is noted here that also a red shift of 60 meV was observed for one sample in the low temperature PL which might be caused by different aggregation in the film forming process. It is known for PPV that the detailed optical properties, such as PL quantum yield, also depend on the preparation conditions used when dissolving the polymer [70].

The PL decay cannot be modelled with a single exponential decay, as already established in literature [69]. Two decay times of 2.7 ns (35 % weight) and 10.0 ns (65 %) were found at room temperature. These values are smaller than the ones found by Chasteen *et al* which might hint to a lower PL quantum yield caused by a different preparation method. At 30 K, both times get larger by a factor of approximately two resulting in 4.3 ns and 20.8 ns for the short and long decay component, respectively. This increase in decay time corresponds well with the larger PL intensity at low temperature.

When looking at the PL excitation spectrum at 30 K in comparison to the room temperature absorption, no significant difference is found. This is an indication that no substantial change

in the optical transitions is introduced upon cooling. In the temperature range relevant for measurements in combination with the InGaN/GaN QWs, i.e. between 30 K and 130 K, the change in PL spectral shape and intensity is marginal. This temperature dependence of the PL is displayed in figure 3.10(b). The integrated PL intensity at 130 K shows a slight decrease to approximately 85 % of its value at 30 K. Such a temperature dependence can also be found in other conjugated polymers [93].

### 3.2.3 Hybrid structure

In this section, the combination of the individual materials presented in the preceding sections will be discussed. The sample structure of the hybrid system is shown in figure 3.11(a). Here, the QW served as excitation donor, while the polymer Cn-ether PPV as acceptor. A thin film of Cn-ether PPV was spin coated onto the single QW structure in the same way as the reference sample. The film thickness was measured by atomic force microscopy (AFM) as depicted in figure 3.11(b). A thin film of the acceptor is needed since only the polymer within a few nm will be excited *via* FRET. Hence, a thickness of around 5 nm was chosen. This resulted in homogeneous films and still provided a sufficiently small distance between donor and a large amount of the acceptor.

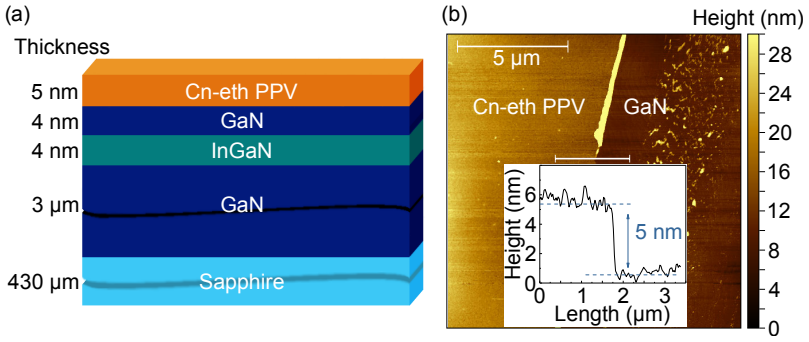


Figure 3.11: (a) Schematic image of the investigated hybrid structure. (b) AFM image with height profile of a spin coated film of Cn-ether PPV on the InGaN/GaN QW structure (adapted from [41]).

Figure 3.12 shows the PL and PLE spectra of the reference samples and the hybrid structure at 30 K in comparison. The spectral overlap between QW emission and Cn-ether PPV absorption can be seen as the shaded region in panel (a). Both the emission of the QW at 2.49 eV and the Cn-ether PPV emission peaked at 1.97 eV are visible and well separated in the PL spectrum of the hybrid sample. The green shaded region in figure 3.12(b) shows the PLE measured at the QW emission in the hybrid sample and is unchanged compared to the reference. More interesting is the PLE spectrum when recording the emission of Cn-ether PPV.

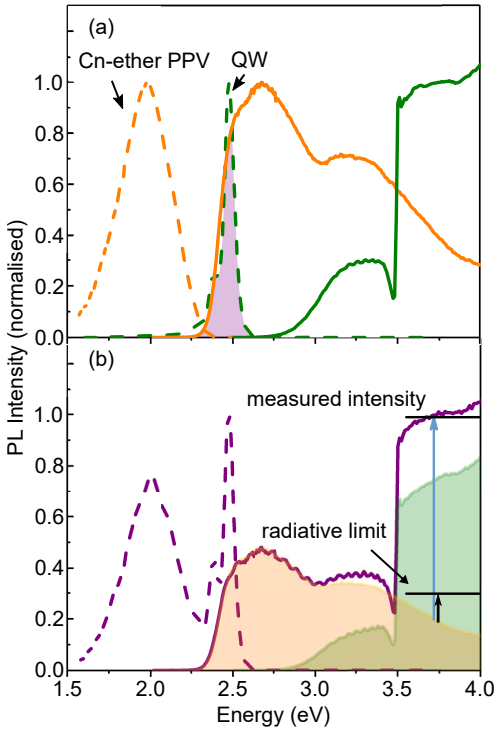


Figure 3.12: (a) Reference PL and PLE of the QW (green) and a film of Cn-ether PPV (orange) at T=30 K. The spectral overlap between QW emission and Cn-ether PPV absorption is shaded. (b) PL and PLE of the hybrid sample. Both emissions are visible and well-separated. The shaded regions show the individual PLE spectra. The black arrow indicates the limit for pure radiative excitation of the Cn-ether PPV as detailed in the text. The blue arrow is the actual measured value (adapted from [41]).

The emission intensity does not only follow the absorption of Cn-ether PPV (orange shaded region), but is also a superposition of the QW and GaN absorption. This can be most prominently seen in the sharp increase of Cn-ether PPV emission intensity when exciting at 3.49 eV and above. This value corresponds to the GaN band gap energy at 30 K. Therefore, the QW excites Cn-ether PPV which then leads to emission from the polymer. The excitation can happen radiatively, in the sense of an emission and reabsorption process, or non-radiatively, in the sense of Förster-like resonance energy transfer, or both. In the following, a qualitative argument will be given that a simple radiative excitation alone cannot explain the PLE spectra recorded, even for $\eta_{QW} = 1$. One can think of the QW as a lamp exciting the Cn-ether PPV at 2.49 eV. For simplicity, it is assumed that the excitation energy is above the GaN band gap (e.g. 3.75 eV as indicated by the arrows in 3.12) meaning that all the excitation light is absorbed. The fraction of excitons generated in the QW is proportional to its absorption

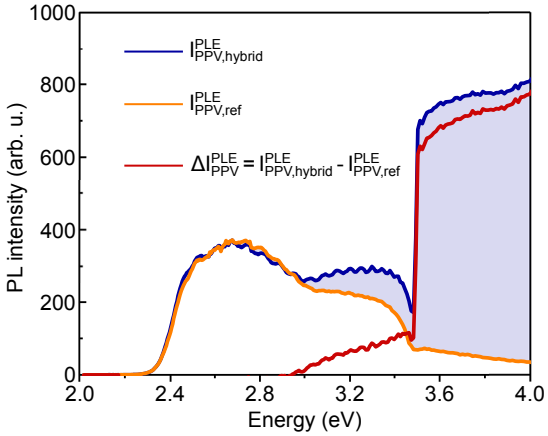


Figure 3.13: Illustration of the derivation of $\eta_{indirect}$. For the reference, $I^{PLE}_{PPV,ref}$, the appropriately scaled PLE at T=140 K was taken since no PLE enhancement was observable anymore at this temperature. The shaded region corresponds to the area of the difference in PLE signal.

and approaches unity when exciting above the GaN band gap energy. The number of photons emitted by the QW that can be absorbed by the Cn-ether PPV is much lower than the number of photons in the lamp at any excitation energy. In more detail, the PLE spectrum measured at the Cn-ether PPV emission (1.98 eV) can be expressed as follows [27]:

$$I^{PLE}_{PPV,hybrid}(E) = \frac{I^{PL}(E = 1.98eV)}{I_0(E)} \; . \tag{3.11}$$

$I^{PLE}_{PPV,hybrid}(E)$ represents the recorded PLE spectrum, $I^{PL}(E = 1.98eV)$ is the measured PL intensity at the fixed emission energy of 1.98 eV and $I_0(E)$ is the intensity of the excitation source in dependence of excitation energy. $I^{PL}$ can be separated into two contributions arising from direct and indirect excitation through the lamp and the QW, respectively. In the linear excitation regime, this can be written as:

$$I^{PL} = I_0 \eta_{PPV}(A_{PPV} + \eta_{indirect} A_{QW}) \; . \tag{3.12}$$

With $\eta_{PPV}$ being the PL quantum yield of Cn-ether PPV, $A_{PPV}$ and $A_{QW}$ the absorbed fraction of excitation light of Cn-ether PPV and the excitons generated in the QW, respectively and $\eta_{indirect}$ the efficiency of the indirect excitation mechanism. Inserting 3.12 into equation 3.11 and solving for $\eta_{indirect}$ leads to:

$$\eta_{indirect} = \frac{I^{PLE}_{PPV,hybrid} - I^{PLE}_{PPV,ref}}{I^{PLE}_{QW,hybrid}} \frac{\eta_{QW,hybrid}}{\eta_{PPV}} \; . \tag{3.13}$$

Here it was assumed that the excitation intensity $I_0$ is the same for Cn-ether PPV and the QW. With an absorption fraction of 0.05 in a 5 nm thick Cn-ether PPV film, this is a reasonably good approximation. Additionally, the PL quantum yield is taken to be independent of excitation energy which is generally the case [28] and $\eta_{PPV}$ does not change in the hybrid. This assumption is justified since almost no change of the PL decay time of Cn-ether PPV is found when deposited on sapphire and GaN for an excitation energy below the QW absorption (see further below figure 3.14 (b)). As mentioned earlier, the PLE spectrum of Cn-ether PPV in the hybrid sample cannot be explained by radiative excitation alone. To better estimate its contribution to the enhanced emission, $\eta_{indirect}$ can be written as $\eta_{indirect} = \eta_{QW}\eta_{out}A_{PPV}(E = E_{QW})$ for radiative excitation only. $\eta_{out}$ is the outcoupling efficiency of the QW PL. Due to the large difference in the index of refraction between Cn-ether PPV and GaN ($\sim$1.5 and 2.4, respectively), only a small portion of the emitted light can be absorbed by Cn-ether PPV. For the resulting critical angle at the Cn-ether PPV/GaN interface of 39° and isotropic QW emission, then $\eta_{indirect} \leq 0.2A_{PPV}(E_{QW})$ even for $\eta_{QW} = 1$. This limit is shown in figure 3.12 by the lower horizontal line. The measured intensity is much higher as illustrated by the blue arrow. Charge transfer from the QW region to Cn-ether PPV is excluded due to the barrier width of the GaN cap. Therefore, the main contribution to the enhanced emission of Cn-ether PPV needs to stem from FRET.

Förster-like resonance energy transfer manifests itself in a shortening of the QW PL decay time. The FRET rate can be viewed as an additional decay channel for the QW excitons. For an otherwise unaltered decay rate of the donor in the hybrid system compared to the isolated donor, the FRET rate can be extracted:

$$\Gamma_{FRET} = \Gamma_{QW,hybrid} - \Gamma_{QW,ref} = \frac{1}{\tau_{QW,hybrid}} - \frac{1}{\tau_{QW,ref}} \, . \tag{3.14}$$

From this, the efficiency of the FRET process can be obtained:

$$\eta_{FRET} = \frac{\Gamma_{FRET}}{\Gamma_{QW,hybrid}} = 1 - \frac{\tau_{QW,hybrid}}{\tau_{QW,ref}} \, . \tag{3.15}$$

Figure 3.14(a) shows the PL decay transients measured at the QW emission in the reference and the hybrid at 30 K. A faster decay is observed in the hybrid sample, as expected for FRET. A FRET efficiency of $\eta_{FRET} = 0.46 \pm 0.08$ is calculated from the decay times. Direct comparison with the efficiency obtained from PLE is not possible since the quantum yield of the QW, $\eta_{QW}$, is experimentally not accessible due to its low value at room temperature.

Nonetheless, both efficiencies derived through the two separate methods should show the same temperature dependence if they origin from the same phenomenon. Consequently, tem-

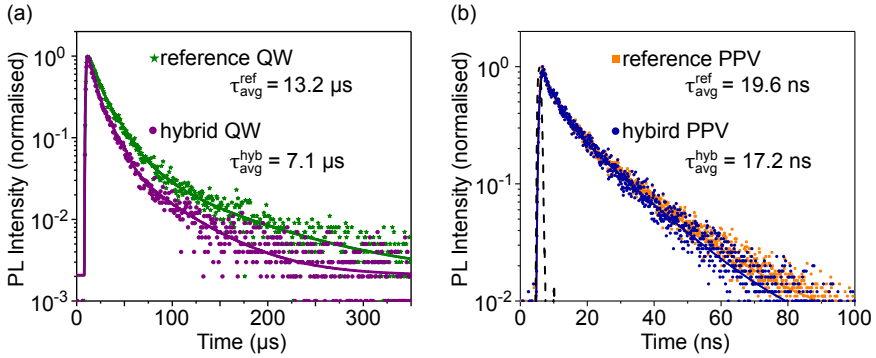


Figure 3.14: (a) PL decay of the QW in the reference and in the hybrid at 30 K. A shortening of the decay time can be observed. (b) PL transient of a thin film of Cn-ether PPV on sapphire and on the InGaN/GaN QW. The excitation energy was 2.79 eV, i.e. probing the Cn-ether PPV selectively (modified from [41]).

perature dependent measurements were performed. Figure 3.15(a) depicts the evolution of the PLE spectra of Cn-ether PPV in the hybrid sample with temperature. Evidently, a decrease in PL emission is seen when indirectly exciting Cn-ether PPV, again most obviously seen for excitation energies above the GaN gap energy. Conversely, insight into $\eta_{FRET}(T)$ as a function of temperature is given by following the temperature behaviour of the QW PL decay. Figure 3.15(b) shows the relative $\eta_{indirect}(T)$ and $\eta_{FRET}(T)$ in comparison. The same trend is reproduced in both cases, i.e. a decrease of the derived efficiencies for increasing temperature. The reason for this becomes more apparent when looking at the rates of the different contributions to the overall PL decay.

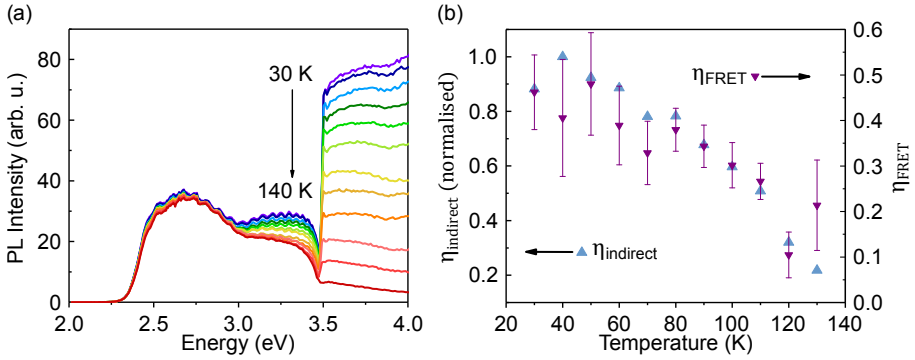


Figure 3.15: (a) Evolution of the PLE signal in the hybrid measured at the Cn-ether PPV emission as a function of temperature. (b) Comparison of the deduced transfer efficiencies with the help of the PLE spectra (blue upwards pointing triangles) and through time-resolved PL (violet downwards pointing triangles). $\eta_{indirect}$ is given in relative values and normalised to the maximum (modified from [41]).

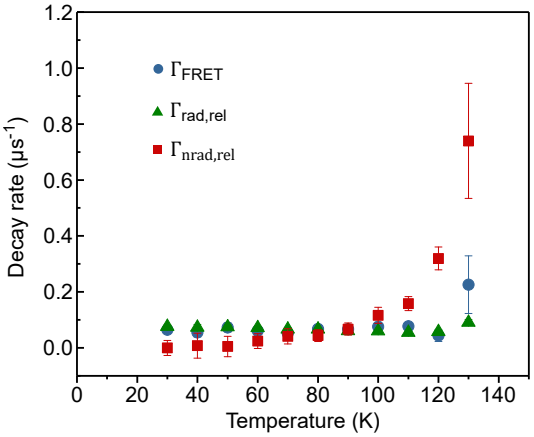


Figure 3.16: Comparison of the radiative, non-radiative and FRET rates calculated from time-resolved measurements. The rates are given relative to a unity PL quantum yield at 30 K. The seemingly increase in $\Gamma_{FRET}$ at 130 K is caused by the large error in fitting the decay curves at this temperature (adapted from [41]).

The PL intensity of Cn-ether PPV is almost not affected by temperature in the measured range in the reference on sapphire. This can also be seen in the PLE spectra of the hybrid sample for direct excitation of Cn-ether PPV. Opposed to this behaviour is the decrease in QW PL intensity with increasing temperature. As pointed out in section 3.2.1, the decrease of the QW PL is caused by the increase of the non-radiative decay rate. Assuming $\eta_{QW}(T = 30K) = 1 - \eta_{FRET}$, one can compare the relative contribution between radiative, non-radiative and FRET pathways. Corresponding rates can then be calculated relative to a temperature of 30 K. Figure 3.16 demonstrates the increase in non-radiative decay rate while the radiative one as well as the FRET rate are not considerably affected in the measured temperature range. This is expected as long as the temperature is low enough to ensure localisation of the QW excitons. The relative value of $\Gamma_{rad}$ and $\Gamma_{FRET}$ are comparable and higher than $\Gamma_{nrad}$ for temperatures lower than 90 K. By increasing the temperature, the non-radiative decay rate becomes larger than the other ones. As a consequence, the majority of excitons generated in the QW decay non-radiatively and are neither transferred to Cn-ether PPV nor decaying radiatively.

## 3.3 Summary and outlook

This chapter studied Förster-like resonance energy transfer from a single InGaN/GaN quantum well to the polymer Cn-ether PPV. The optical properties of the QW were found to be dominated by large internal electric fields, in the order of 1-2 MV/cm. Nonetheless, a FRET efficiency of 0.46 was found at low temperatures using time-resolved PL measurements. PL

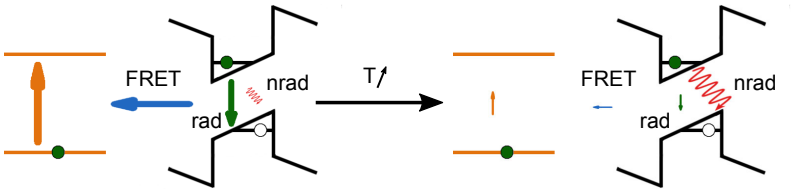


Figure 3.17: Sketch illustrating the competition between the three different decay channels in the QW. At low temperatures FRET and radiative decay dominate, leading to an efficient excitation of the Cn-ether PPV. At higher temperatures, non-radiative channels are most probable (adapted from [41]).

excitation spectroscopy showed that the acceptor, Cn-ether PPV, emitted more light as a consequence of FRET than through a trivial radiative mechanism. These results highlight the principle advantage of non-radiative colour conversion, since the external quantum efficiency is not limited by the large difference in refractive index of the two materials. On the other hand, the reduced wavefunction overlap of electrons and holes, due to the internal electric field, will result in smaller rates both for the radiative and FRET process in a similar manner. This is expected since both processes are to first order mediated by electric dipole coupling. As long as non-radiative pathways are suppressed, FRET can be efficiently active. For the investigated sample, non-radiative decay was suppressed by cooling it to cryogenic temperatures. When increasing the temperature, the non-radiative rate became dominant over the FRET and radiative rates. It is therefore crucial to circumvent these non-radiative decay channels, especially for samples with large internal electric fields, which can in principal be done.

Nowadays, commercial white LEDs show a power conversion efficiency of ca. 0.4 - 0.5 [94]. This high value is dependent on the quantum yield of the LED and the colour converter, but also on efficient light out-coupling from the GaN-based LED. A high out-coupling efficiency can be achieved through additional refractive index matching layers or by nano-structuring the LED surface [95]. The FRET conversion scheme bypasses this problem since the transfer is non-radiative. Efficiency droop in LEDs is mentioned as a final outlook to this chapter. By this, it is meant that the efficiency decreases when operating under high current densities. Apart from an increase in device temperature, which leads to a decrease in efficiency, Auger recombination is also believed to contribute to the droop [91, 96]. Under the assumption of a competitive FRET rate, non-radiative energy transfer can lower the electron and hole density without them being lost non-radiatively. It was shown theoretically that the transfer rate grows with increasing charge carrier concentration in a ZnO/molecular system [97]. A similar conclusion was drawn in an experiment using quantum-well nanorods and colloidal nanocrystals [98]. Zhuang *et al.* investigated resonance energy transfer from InGaN/GaN nanorod LEDs to

colloidal nanocrystals in the efficiency droop regime [50]. They found a slight increase in the relative external quantum efficiency at high current densities in the FRET LED as compared to one without the nanocrystals. Further investigating colour conversion *via* FRET in the efficiency droop regime and absolute power conversion efficiencies can therefore be of interest for high power LEDs.

# 4 Growth and optical properties of transition metal dichalcogenides

*Two publications form the basis of this chapter. The first part builds up on* Pulsed thermal deposition of binary and ternary transition metal dichalcogenide monolayers and heterostructures [99] *by N. Mutz, T. Meisel, H. Kirmse, S. Park, N. Severin, J. P. Rabe, E. J. W. List-Kratochvil, N. Koch, C. T. Koch, S. Blumstengel and S. Sadofev. The author performed and analysed PL, absorbance, sheet resistance measurements as well as obtained optical micrographs on the samples grown by Dr. S. Sadofev in order to provide feedback for optimising the growth process. T. Meisel supported the interpretation with additional measurements. H. Kirmse and C. T. Koch performed and analysed TEM and EDXS measurements. S. Park and N. Koch measured and interpreted XPS. N. Severin and J. Rabe measured and analysed Raman spectra. S. Sadofev and S. Blumstengel wrote the manuscript. E. List-Kratochvil, S. Sadofev, S. Blumstengel and N. Mutz planned and interpreted the experiments. All authors contributed to the final manuscript. This chapter extends the data already presented in the publication through the comparison of the optical properties with mechanically exfoliated and commercially CVD-grown $MoS_2$. Additionally, an improvement of the crystal grain size is shown when using soda-lime glass as the growth substrate. The second publication refers to* Direct determination of monolayer $MoS_2$ and $WSe_2$ exciton binding energies on insulating and metallic substrates [38] *by S. Park, N. Mutz, T. Schultz, S. Blumstengel, A. Han, A. Aljarb, L-J. Li, E. J. W. List-Kratochvil, P. Amsalem and N. Koch. The contribution of the author lies in the experimental determination of the exciton transition energy through reflectance measurements. S. Park in the group of N. Koch wrote the manuscript and collected all data. S. Park and T. Schultz performed PES and DFT calculations. S. Blumstengel analysed DRS spectra. A. Han, A. Aljarb and L. Li prepared the samples. All authors finalised the manuscript. Additionally to the two substrates presented in the publication, reflectance data on three more substrates and their analysis using the transfer matrix method is shown.*

Two-dimensional transition metal dichalcogenides (TMDCs) moved into focus of research in 2004 after the successful exfoliation of graphite into its monolayer graphene and by showing

its unique properties, such as high carrier mobility and mechanical strength [100, 101]. Like graphite, bulk TMDC crystals are built up of individual sheets. They are strongly bound in the plane of the sheet, but only weakly bound out-of plane. Therefore, these crystals can be cleaved into monolayers comprised of one transition metal in the center and two chalcogenide atoms on top and below when viewed from the side (see figure 4.1). In the monolayer, these TMDCs can show different physical properties than in the bulk which are beneficial for opto-electronic applications, such as a direct band gap [102]. A large variety of TMDCs exists. However, in recent years, the majority of studies focussed on the following four semiconducting TMDCs: $MoS_2$, $MoSe_2$, $WS_2$ and $WSe_2$. Likewise, the focus of this thesis lies on these four TMDCs. They are referred to when using the term TMDC together with the addition of metallic $TaS_2$.

This chapter introduces the fundamental properties of the TMDCs, which will also be of use for the following chapter. The book by Kolobov and Tominaga served here as a starting reference [103]. After the introduction, a new TMDC deposition method called pulsed thermal deposition (PTD) is described. The growth of large area TMDC monolayers is usually done by chemical vapour deposition methods. This fabrication method uses a carrier gas and precursors which form the TMDC on a heated growth substrate. Due to the use of carrier gases, it is not possible to work in ultra-high vacuum (UHV) conditions. The control of the carrier gas flux and thus the precursor flux is challenging. Using physical vapour deposition in UHV avoids these challenges. It is found that TMDC monolayers can be formed by simple thermal resistive heating of metal wires together with conventional sublimation of chalcogenides. The versatility of this method is exemplified by the growth of $Mo_{1-x}W_xS_2$ alloys and thin heterostructures of $TaS_2/MoS_2$.

In a second part of this chapter, the impact of the substrate on optical and electronic properties is investigated. The focus lies on obtaining exciton transition energies using differential reflection spectroscopy (DRS). Since monolayer TMDCs are only three atoms thick, the electrons will be influenced by the dielectric function of the surroundings. This effect is studied with photoelectron spectroscopy (PES) in combination with optical spectroscopy in order to determine the energy gap and exciton transition energy by two separate methods. From these two values, the exciton binding energy is obtained. The last part of this chapter will summarise the findings.

## 4.1 TMDC fundamentals

TMDC crystals are layered with only weak van der Waals bonds between individual layers. This gives rise to the possibility of exfoliating bulk crystals into single layers up to the limit of one monolayer with sub-nm thickness. Electronic and optical properties of the TMDCs are

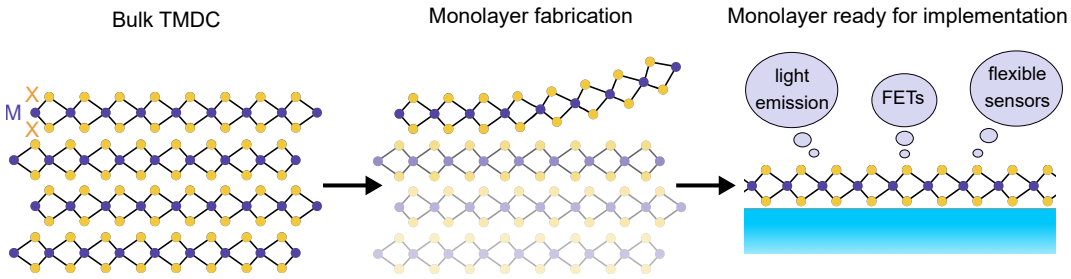


Figure 4.1: Sketch from bulk to monolayer TMDC by mechanical exfoliation and possible applications. The transition metal is denoted as $M$ and shown in blue while the chalcogen atoms are depicted in yellow and as an $X$.

strongly affected when making the transition from many to one layer. Even already bilayer and monolayer feature different behaviour [104, 105]. These altered properties, presented in more detail below, make the TMDCs interesting and promising for fundamental and applied research. Albeit the vast increase in published papers in the last ten years or so, they are fairly old. Bulk TMDCs, like $MoS_2$, were investigated in the mid-70s or used in industry as dry lubricants [103, 106]. The first report of an $MoS_2$ monolayer was as early as 1986, but interest grew only after the demonstration of novel physical properties of two-dimensional graphite in 2004 [107]. Graphene exhibits very large charge carrier mobilities of 15000 $cm^2/(Vs)$ at room temperature and the largest mechanical strength tested so far [108, 109]. It thus seemed obvious to look for other materials which can be brought from a 3D bulk crystal into 2D sheets and can be used alongside graphene. The four TMDCs with the formula $MX_2$, where $M = \{Mo, W\}$ and $X = \{S, Se\}$, are all semiconducting. Therefore, this makes them promising candidates for applications where a band gap is needed, which pristine graphene is missing. Such applications include transistors and optical sensors that require high carrier mobilities and large light-matter coupling. It was found that in monolayers of these TMDCs, carrier mobilities of up to hundred $cm^2/(Vs)$ and high on-off ratios in field-effect transistors (FETs) of $10^8$ can be obtained [110]. Additionally, the TMDCs show a transition from an indirect band gap in the bulk to a direct one in the monolayer, which manifests itself, for example, in an increase in photoluminescence (PL) intensity [111]. These two characteristics make them already interesting for applications and fundamental research. A few of their properties will be reviewed in the following in some more detail.

### 4.1.1 Band structure properties

The four semiconducting TMDCs all have a direct band gap only as monolayer. Already in the bilayer the electronic band gap is indirect [104, 112]. The direct band gap in the monolayer

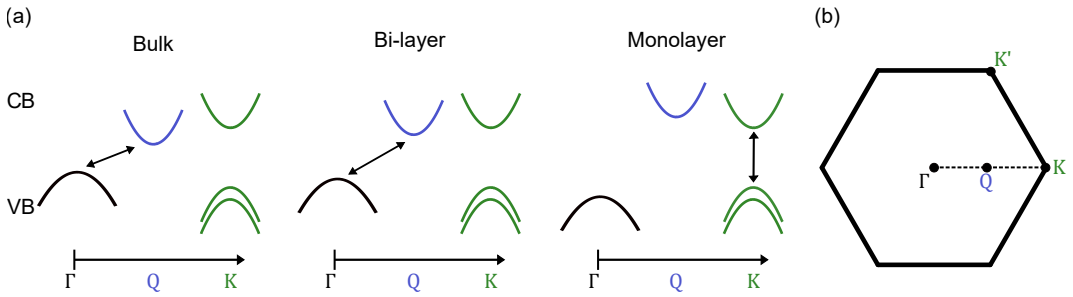


Figure 4.2: (a) Schematic evolution of the valence and conduction band extrema from bulk to monolayer. Only the spin-orbit split bands at the valence band K-point are shown for clarity (redrawn from [104]). (b) Hexagonal Brillouin zone with the high symmetry points displayed.

is found at the $K$-point in $\mathbf{k}$-space of the hexagonal Brillouin zone. On the other hand, the indirect band gap is situated at the Γ-point for the valence band maximum and between Γ- and $K$-point (called $Q$ or sometimes Λ-point) for the conduction band minimum. The crossover between indirect and direct semiconductor is caused by a decrease in energy of the valence band at Γ and an increase of the conduction band at $Q$ with decreasing number of layers while the bands at $K$ are only weakly affected (see figure 4.2).

From first-principles calculations, the states at Γ and $Q$ are found to have a larger contribution of the more de-localised chalcogen $p$ orbitals to the mixing with the metal $d$ orbitals than the states at the $K$-point. Therefore, the states at Γ and $Q$ are more sensitive to the number of layers [103, 113, 114]. In the experiment, the transition between an indirect and a direct band gap is seen by an increase of the PL intensity in the monolayer and a slight blue-shift in the transition energies [111]. There exists a significant contribution of spin-orbit coupling (SOC), because of the metal $d$ orbitals, leading to a splitting of the valence band maximum (VBM) and the conduction band minimum (CBM). Due to the lack of inversion symmetry of the monolayer unit cell, the $K$ points at the edge of the hexagonal Brillouin zone are inequivalent, e.g. in their spin state, and usually termed $K$ and $K'$ (or $K^+$ and $K^-$). In addition, SOC leads to an energetic difference between the spin-up and -down states which allows them to be accessed individually [102]. Most of the splitting takes place in the valence band with a total amount of around 150-200 meV for $MoX_2$ and 400-500 meV for $WX_2$ TMDCs [115]. SOC is the explanation for the appearance of the so-called A and B exciton peaks in absorbance and PL.

The energy gap in two-dimensional TMDCs is also affected by strain. Theoretical and experimental studies demonstrated that in-plane positive strain leads to a decrease in band gap energy and a shift from direct to indirect gap [116–118]. Under compression it was found

that the band gap first increases up to about 22 GPa and subsequently decreases again [119].

### 4.1.2 Optical properties and defects

**Excitons in TMDCs**

The optical properties of TMDCs are dominated by excitons and their description given here follows in some part the review by Wang *et al* [120]. Due to quantum confinement and the low dielectric screening in monolayer TMDCs, excitons have binding energies of up to several hundred meV. Exciton Bohr radii are in the nm range thus extending over a few lattice sites, putting TMDC excitons in between tightly bound Frenkel and weakly bound Wannier-Mott excitons. Methods developed for inorganic semiconductors are usually applicable in the description of their optical properties, but the two-dimensional nature and their immediate surrounding also need to be taken into account. Prominent peaks exist in the absorption spectra of TMDCs. They are termed A, B, C, D, E according to early investigations by Frindt and Yoffe [121] (figure 4.3). In the monolayer, the transition correlated with the A peak is assigned to an exciton stemming from an excitation at the direct band gap at the K-points. It originates from the higher lying SO-split valence band maximum while the B exciton is shifted to larger energies by the amount of SO-splitting. Since most of the splitting takes place in the valence band, the energetic difference between A- and B-exciton corresponds approximately to the splitting of the valence band at the K-points.

In general, excitons can be free or localised and bound, for example, at a defect site. This will lead to a different behaviour observable in PL experiments such as a reduced transition energy [122]. For TMDCs, the room temperature PL is usually attributed to a transition stemming from free excitons together with a contribution from charged excitons, called trions [123, 124]. Coherence times of the free exciton state were calculated to be on the sub picosecond time-scale with an effective lifetime due to thermalisation of few to tens of ps at liquid helium temperature up to nanoseconds at room temperature [125–127]. Experimentally, a fast decay of the coherence time of a few hundred femtoseconds has been deduced [128–131]. Obtained PL decay times, i.e. the measurement of the effective radiative and non-radiative lifetime, scatter from sub ns to several ns, depending on the sample quality, preparation and excitation conditions [132–134]. Another peculiarity of the four TMDCs is that their decay dynamics behave differently with temperature for $MoX_2$ as compared to $WX_2$ [135]. It was found that the PL intensity decreases with increasing temperature for the Mo containing TMDCs while it is the opposite for the W ones [136]. This behaviour was interpreted such that excited states exist in $WX_2$ which are lying energetically lower than the optically bright A-exciton. One state corresponds to a first order spin-forbidden transition since the spin-split conduction band minimum is of a different electron spin state than the valence band maximum. Additionally to

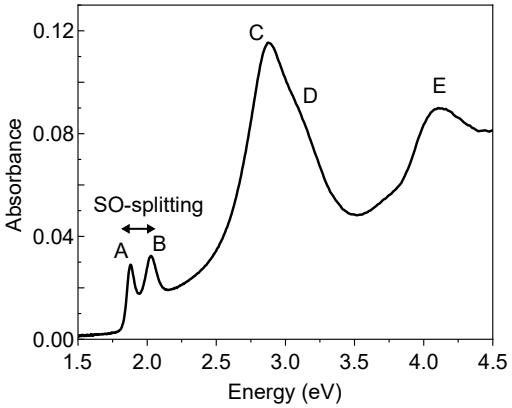


Figure 4.3: Typical absorbance spectrum of an $MoS_2$ monolayer with the appellation of the characteristic peaks.

the optically spin-forbidden excitation, it was theoretically found that in tungsten containing TMDCs momentum-forbidden excitons, i.e. electron-hole pairs in different **k**-valleys exist at lower energies than the A exciton [137]. For $MoS_2$ also a lower lying exciton state was shown, namely where the hole resides in the Γ valence band and the excited electron in the Q conduction band. But it was argued that the energy difference to the exciton at the K-point might be only on the order of 10 meV, also depending on the band structure input calculated by density functional theory (DFT). The schematic excitonic energy landscape given by Malic *et al.* has as a consequence that in their investigations the energetically lowest exciton is bright only in $MoSe_2$ [137]. The bright exciton of the other TMDCs is just populated after adding energy to the system, for instance by raising the temperature up to room temperature. In related studies, the thermalisation of the exciton in the K-valley as well as scattering into the lower lying dark states was seen to occur ultra-fast over only a few hundred fs [138]. The exciton formation for non-resonant excitation was also found theoretically and experimentally to happen on a sub- to picosecond timescale [139–141]. In the case of the theoretical studies, no scattering with defects and no interaction with residual charges or other excitons was included which would lead to quantitatively different times [120]. However, the general trend in these studies is that exciton formation as well as thermalisation and scattering into the lowest lying dark states occurs on an ultra-fast time scale. Although there exist dark excitonic states with electron and hole in different **k**-valleys lower in energy than the bright ones, the single particle energy band gap is still direct at the K-point in all four TMDCs.

**Trions**

Apart from the exciton, there exist other energetically lower lying optical transitions observable in PL. A second PL peak is often seen in TMDC samples approximately 20 to 40 meV

lower in energy than the A-exciton. This peak is associated with a three body quasi-particle, called a trion. A trion is a charged exciton, i.e. an exciton bound with either an additional electron or hole. Newaz *et al.* showed a modulation of the PL intensity of $MoS_2$ with varying electric field in a FET configuration [142]. Mak *et al.* performed similar experiments and observed an additional peak emerging in the absorbance and PL spectra with applied gate bias [143]. One transition was assigned to the A exciton and the other one to a negative trion. It was found that the PL intensity of the exciton grew with applied negative bias. Further experiments with electron withdrawing molecules deposited on $MoS_2$ showed similar trends and were interpreted as a depletion of the n-doped TMDC, enhancing the free exciton emission [144]. Apart from acceptor molecules, like F4TCNQ, the PL of $MoS_2$ excitons was also found to improve in ambient air [145]. Measurements with different gases, such as $O_2$ and $H_2O$ vapour showed qualitatively the same effect on the PL as electrostatic doping in a FET configuration, namely an increase in the free exciton PL intensity. DFT calculations proposed a charge transfer mechanism from $MoS_2$ to the physisorbed oxygen or water molecules [146]. As a second effect, it was put forward that sulphur vacancies in $MoS_2$ are responsible for electronic states within the band gap [147]. Oxygen could then passivate these defects by chemisorption at the vacancy sites, leading to a decrease in gap states and consequently to a decrease in the non-radiative decay rate [148].

**PL quantum yield**

So far, untreated TMDC monolayers show a low PL quantum yield (QY) in the range of a few percent [103]. There are several reasons investigated to be responsible for such low QY. One of them is the fast scattering into dark states in W-based TMDCs [137]. On the other hand, the effect of the substrate on PL spectra of various TMDCs was investigated. Sandwiching TMDC monolayers between h-BN led to an enhanced emission intensity together with a severe reduction of the PL linewidth [131]. Additionally, native defects can lead to states within the band gap which might enhance non-radiative decay channels [145]. In particular for the case of $MoS_2$, it was pointed out that sulphur vacancies are the most likely ones to occur [149]. They are reported to be the reason for unintentional n-type doping in $MoS_2$, but theoretical studies showed that they might act as electron charge compensation centres [147, 150–152]. From calculations it was inferred that they produce unoccupied states in the mid-gap and occupied ones close to the valence band maximum. In FET measurements, typically n-type behaviour is observed for $MoS_2$, but also locally p-type conductivity is found [153]. For large workfunction electrodes p-type conductivity can be achieved as well [154]. Park *et al.* recently showed occupied gap states in ultraviolet photoelectron spectroscopy (UPS) of $MoS_2$ on sapphire close to the Fermi level which are absent when the monolayer is deposited on gold or HOPG [155]. Singh *et al.* performed DFT calculations with the result that hydrogen

incorporated in or adsorbed on the $MoS_2$ lattice could function as shallow donors leading to a filling of the sulphur vacancy gap states [156]. As can be seen from this discussion, the origin of n-type doping is still under debate. Also, a contribution to unintentional doping from the underlying substrate needs to be taken into account [157–159]. Other vacancies like missing Mo or antisites were found to occur with lower probability and were predicted to produce mid-gap states [149]. By performing scanning tunnelling electron microscopy (STEM) and FET measurements, Hong *et al.* found that antisites, where Mo replaces one or two S atoms, could be responsible for a reduced electron and hole mobility. On the other hand, sulphur vacancies did not lead to such a decrease [160]. The healing of sulphur vacancies with MPS molecules, however, was shown to lead to an improvement in FET mobility [161]. Strain also has an effect on the optical properties leading to a decrease in PL intensity [117]. Grain boundaries were either found to decrease or increase the emission intensity depending on the relative orientation of the two grains [162, 163]. An additional reason for the small PL QY was suggested by Lien *et al.* [164]. Their study hints towards the interaction of excitons with residual charges and of exciton-exciton annihilation to be mostly responsible for the low PL QY. In their earlier work, they showed that post-treatment of $MoS_2$ with the super acid TFSI (bis(trifluoromethane) sulfonimide) leads to an enhanced PL intensity [133, 165]. Later it was found that electrostatic gating leads to the same observations. It was concluded that the origin of an increase in PL intensity is in both cases a reduction of excess charge carriers, while defects were not passivated or cured. In experiments, a large exciton-exciton interaction was deduced, effectively leading to a reduced PL QY [166–168]. This was also concluded for exciton interaction with residual charges resulting in scattering and the formation of trions [120, 169, 170].

### 4.1.3 Charge carrier transport and doping

The theoretical maximum of the mobility for TMDCs is in the range of a few hundred $cm^2/(Vs)$ at room temperature. Mobilities found in experiments were approaching 100 $cm^2/(Vs)$ in $MoS_2$ FETs [171]. The TMDC FETs show a dependence of the extracted mobilities on the underlying dielectric substrate in addition to scattering at crystal imperfections. It was shown that, when using $SiO_2$ as the gate dielectric, the FETs show reduced mobilities and long persistent photoconductivity [172–174]. This observation was attributed to scattering and capturing of charge carriers at impurities of the gate dielectric and water and oxygen adsorbates. An increase in mobilities was achieved when using PMMA, h-BN or high-$k$ materials, such as $HfO_2$, as the gate dielectric [171, 175, 176]. This can partially be explained by the damping of Coulomb scattering as put forward by Jena *et al.* [177]. Their theoretical considerations show that the environmental dielectric function plays a critical role in thin films. For high-$k$ materials the scattering rate is reduced and, hence, the charge carrier mobility is enhanced. In terms

of doping, it was found that most of the TMDC monolayers show n-type behaviour while in $WSe_2$ p-type doping was observed [150] depending on the preparation conditions. Intentional doping can be subdivided into two classes. Introduction of impurity atoms into the TMDC lattice corresponds to the classical p- or n-doping in conventional bulk semiconductors like Si or GaN. Usually, Nb is introduced as p- and Re as n-dopant either when growing bulk crystals or fabricating TMDC monolayers [150, 178]. The other method could be called environmental doping where atoms or molecules are brought into contact with the TMDC layer and lead to a change in the Fermi level by charge transfer or electrostatic interaction. Environmental doping makes use of the fact that the ultra-thin TMDC layers are directly affected by their surroundings. In this respect, electron donating or accepting molecules have been adsorbed on the TMDC surface. Many molecules have been tested [179]. To give an example, an electron withdrawing (p-doping) effect was observed for the deposition of F4TCNQ molecules while an electron donating one (n-doping) was shown for NADH. Electrostatic doping can also be implemented in a FET geometry and controlled with the gate electric field [180]. It can be seen that a variety of possibilities for the manipulation of the electronic properties are under investigation and still ongoing.

### 4.1.4 Raman spectra

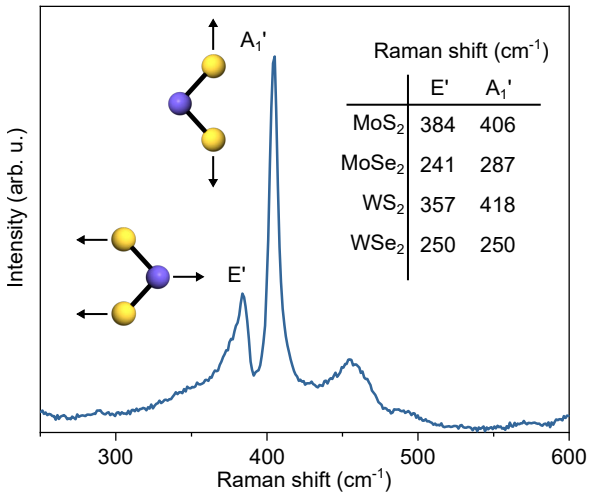


Figure 4.4: Raman spectrum of monolayer $MoS_2$ together with a sketch of the respective vibrations. The table gives the wavenumber values of the E' and A'$_1$ vibrations of the four TMDCs according to [181].

The spectral positions of two characteristic Raman modes were shown to depend on the layer number and could, therefore, be used as a tool to determine the thickness [182]. They are

termed $A_1'$ and $E'$ (or sometimes $A_{1g}$ and $E^1_{2g}$ from the nomenclature of the bulk) and their respective vibration is shown in figure 4.4 together with the room temperature wavenumber of the monolayer for the four TMDCs [181]. Similar to the band energies and PL properties, the Raman spectra were also shown to depend on different other parameters. In particular, the frequency of the $A_{1g}$ vibration in $MoS_2$ was found to be sensitive to the carrier concentration and can therefore be used to indicate doping densities [183]. Strain and pressure also influence the Raman spectra and can serve as a tool to determine these [117, 184].

### 4.1.5 Influence of the dielectric surrounding on the electronic and excitonic states

Since two-dimensional TMDCs consist of only one monolayer, their electronic and optical properties are strongly affected by the surrounding [179]. Some of the aspects regarding PL efficiency and charge carrier transport have already been mentioned above. In this section, the influence of the surrounding dielectric function on the TMDC band gap and exciton binding energy will be presented as discussed by several authors [14, 16, 185–189]. A trend of decreasing dielectric constant with increasing band gap energy is seen in 3D inorganic semiconductors. Moss put this relation in terms of the energy gap and the effective dielectric constant as $E_g \propto 1/\epsilon^2_{eff}$ [190]. There exist also other models and empirical formulas which give similar trends as the Moss relation and can be fitted to experimental data [191]. The binding energy in the effective mass approximation for a Wannier-Mott exciton is given with the same proportionality, $E_b \propto 1/\epsilon^2_{eff}$. The physical picture is that in both cases the Coulomb interaction of a point charge is screened by the surrounding medium. Therefore, in a first approximation, it can be assumed that both the band gap and the exciton binding energy are affected in the same way by the dielectric constant.

In the 2D case, the interaction of two point charges embedded in a thin slab of a dielectric with thickness $d$ surrounded by two dielectric materials was investigated by Keldysh [192, 193]. The author considered the assumptions that the surrounding dielectric constants are much smaller than the one for the thin slab and that the exciton Bohr radius is larger than $d$. Then, the interaction potential takes the form of a screened Coulomb potential ($V \propto 1/(\rho\epsilon_{eff})$) for large distances $\rho$ between the two charges and a logarithmic behaviour for small $\rho$ with a characteristic screening length $\rho_0 = d\epsilon_2/(\epsilon_1 + \epsilon_3)$ separating these two regimes. Here, $\epsilon_{\{1,3\}}$ are the dielectric constant above and below the TMDC monolayer while $\epsilon_2$ is the dielectric constant of the TMDC [194]. Importantly, the dielectric function entering the Coulomb potential becomes wave vector dependent (similarly expressed with the charge separation $\rho$) in addition to the frequency [195]. In contrast to bulk semiconductors, the dielectric surrounding also needs to

be taken into account. This gives the possibility of tuning the energy band gap, for example by spatially varying the dielectric constant of the substrate [16, 186, 196]. An expression for the effective dielectric function can be found in [197] and here only the limiting cases will be cited. For small absolute values of the wave vector $q << 1/d$ (large $\rho$), the charges will be mainly affected by the surrounding medium and $\epsilon_{eff} \rightarrow (\epsilon_1 + \epsilon_3)/2$. For large wave vectors $q >> 1/d$ (small $\rho$) $\epsilon_{eff} \rightarrow \epsilon_2$, i.e. similar to the 3D case. Typical screening lengths and exciton radii $a_{exc}$ are $\rho_0 \approx 3 - 4\ nm$ and $a_{exc} \approx 1\ nm$ in free-standing TMDCs so that an intermediate effective dielectric constant is needed to describe screening within this model [197]. Chernikov *et al.* [15] applied this model by experimentally investigating the excitonic series of the $WS_2$ A-exciton from 1s to 5s. A non-hydrogenic behaviour was found and explained by the increasing radius of the excited state excitons which manifests itself in a varying dielectric function. This is an interesting observation of the non-locality of the dielectric function in 2D TMDCs. It needs to be kept in mind that the above considerations are valid under the assumptions of $\epsilon_2 >> \epsilon_{1,3}$ and $\rho > d$ as pointed out by Cho *et al.* [14]. These approximations are given for monolayer TMDC excitons on substrates like $SiO_2$. For a more general screening potential other techniques, like image charges, can be applied. In such a way, the band gap and exciton binding energy were investigated as a function of the dielectric surrounding theoretically [14]. The authors found a very similar absolute decrease of the band gap energy and the 1s exciton transition energy so that the optical gap stays roughly the same for increasing dielectric function. On the other hand, the 2s state was found to show a stronger deviation in the transition energy.

Experimentally, the exciton binding energy can be obtained by measuring the band gap energy and the optical gap. This was done with the help of scanning tunnelling spectroscopy (STS) and it was shown that the band gap of $MoSe_2$ decreases when it is deposited on graphite instead of bilayer graphene [198]. This effect was attributed to the different dielectric screening between graphite and bilayer graphene. Wang *et al.*, however, reported no difference in the STS band gap between bilayer graphene and graphite [199]. The discrepancy was explained by different measurement and growth conditions leading to a change in defect density which could affect the band gap measurement. A disadvantage of STS is that it is not sensitive to the reciprocal lattice vector $\mathbf{k}$ meaning that it also probes states at local band extrema, like the $\Gamma$-point. Moreover, usually a conducting substrate is needed limiting the range of dielectric environments that can be investigated. Another technique to obtain the electronic band gap is photoelectron spectroscopy (PES) and inverse PES. PES can be performed by resolving the angle at which electrons leave the sample and which in turn can be translated to $\mathbf{k}$. In such a way the band dispersion can be mapped. Combining PES and optical measurements can give experimental insight on the band gap and exciton binding energy as a function of the

underlying substrate dielectric constant. This will be discussed in section 4.3 as part of the experimental findings of this thesis.

### 4.1.6 Fabrication methods of monolayer TMDCs

In order to distinguish between extrinsic and intrinsic properties, control over the monolayer growth is needed. So far, mostly mechanically exfolatied monolayers or monolayers fabricated by chemical vapour deposition (CVD) are used. These methods have advantages and disadvantages, as will be laid out in the following. It will be discussed why physical vapour deposition methods could serve as a third method alongside the other two. Layered bulk TMDCs can be cleaved into a single layer in the same way as graphite into graphene by mechanical exfoliation. Schematically this is shown in figure 4.5(a). Usually, adhesive tape is used but also freshly cleaved mica (as sketched in the figure) or gold can be used to thin the bulk crystal down until one ends up at a monolayer. This method gives generally flakes of good optical and electronic quality since bulk crystals can be obtained with high purity. Moreover, it can be done at relative ease without needing costly equipment. One disadvantage is the flake size of a few tens of µm, although it was recently shown that gold-mediated exfoliation can lead to flakes of millimetres in lateral size [200, 201]. Another drawback is that not only monolayers but also multilayers are obtained without control of the thickness. Other methods have been therefore developed whereat CVD methods have been the most used ones. In figure 4.5(b) an example for the CVD growth technique is schematically illustrated. Elemental chalcogen and a metal precursor, like $MoO_3$ or $WO_3$, are evaporated in a heated tube furnace. The two materials are transported with a carrier gas, such as argon, towards a heated growth substrate at which the TMDC is formed. Not only the metal and chalcogen sources depicted here are used but various precursors are under investigation. For example, TMDC powder itself, pre-deposition of a thin metal or metal-oxide film on the growth substrate or metal-organic sources are used [202]. It

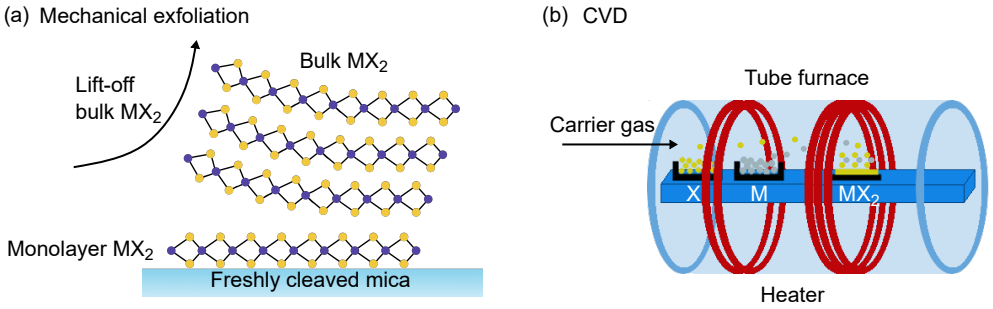


Figure 4.5: Fabrication methods for monolayer TMDCs. (a) sketches the mechanical exfoliation route while (b) displays the principle of CVD.

has also been shown that alloys and heterostructures with other TMDCs can be fabricated by CVD [103, 202]. CVD grown monolayers tend to form triangles with edge lengths of several tens to hundreds of µm which can merge together to give polycrystalline closed monolayers. By now, the optical and electronic characteristics can be comparable to exfoliated flakes. Still, the control of the growth parameters like material flux, constant temperature or stoichiometry is difficult due to many growth parameters. For instance, it has been shown that not only the growth time and temperature but also the carrier gas flow influences the growth as well as the substrate position where the TMDC forms [203, 204]. Physical vapour deposition (PVD) techniques in ultra-high vacuum (UHV) like molecular beam epitaxy (MBE) are also being explored but are less common so far [205–208]. Here, the advantage lies in the better control of the atomic flux, in particular when thinking of alloys, heterostructures or doping. Moreover, the use of UHV limits undesired contamination. As a challenge, it can be mentioned that MBE growth is more work intensive and the workflow is not so easily scalable for industry applications. Usually, the evaporation of elemental molybdenum and tungsten is done by an e-beam evaporator which is costly. The next section will therefore show an experimental method developed in-house of how this issue can be tackled. Within, results that highlight the versatility of using MBE to grow TMDCs alongside the more established CVD process will be discussed.

## 4.2 Pulsed thermal deposition

### 4.2.1 Experimental background

Pulsed thermal deposition (PTD) is a PVD technique which uses thermal resistive heating of a metal wire as the Mo, W or Ta source, similar to a light bulb. It was developed since elemental transition metals and chalcogenides need largely different temperatures of more than 2000 °C and less than 200 °C for the metals and chalcogenides, respectively, to reach suitable vapour pressures. In MBE growth, usually a large and costly electron beam evaporator is used for the deposition of these metals. Conventional melting of the metals is not easily possible since standard crucibles themselves are composed of these materials. In PTD however, a small, pure wire of the desired metal is heated by letting a current flow through it. This makes the method very easy to implement. Due to its electrical resistivity, the wire heats up to a temperature at which a small amount of metal is sublimed. To improve the longevity of the wire and to control the amount of deposited material, the current is applied in a pulsed instead of a continuous mode. The evaporation takes place in a vacuum chamber together with the co-evaporation of the elemental chalcogen. Both elements will impinge on the heated growth substrate, as shown in figure 4.6.

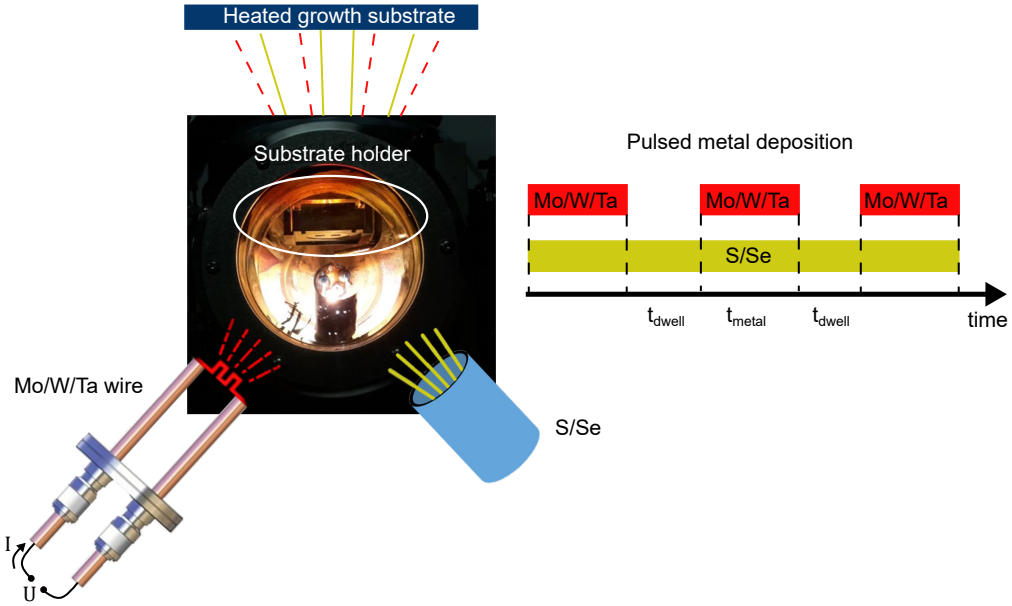


Figure 4.6: Schematic setup of the PTD chamber. The chalcogen is evaporated from a standard Knudsen cell. The current flows through the metal wire in a pulsed mode while S (Se) is evaporated simultaneously all the time as depicted on the right-hand side. The substrate is facing downwards and can be heated from the back side.

The evaporation rate and, therefore, the flux of metal atoms can now be controlled by the electrical power $P = UI$ sent through the wire. The electrical power is dissipated into heat and the temperature $T$ of the wire is related to the electrical power by $P_{el} \approx P_{rad} \propto \sigma T^4$ [209]. Here, the approximation is made that the heat is converted completely into radiation. $P_{el}$ and $P_{rad}$ are the electrical and radiated power, respectively, and $\sigma$ is the Stefan-Boltzmann constant. On the other hand, the evaporation flux $\Phi_e$ is given by the Hertz-Knudsen equation

$$\Phi_e = \frac{\alpha_v (P_v - P_h)}{\sqrt{2\pi m k_B T}} \,. \tag{4.1}$$

$\alpha_v$ is the coefficient of evaporation and lies between zero and one. $k_B$ is the Boltzmann constant, $m$ is the mass of the evaporated metal, $T$ is the temperature and $P_v$ and $P_h$ are the vapour and ambient pressure, respectively [21]. Experimentally, the temperature can be obtained through Wien's displacement law by treating the wire as a black body and measuring the peak maximum of the emitted spectrum [210]:

$$\lambda_{peak} \approx \frac{2880\ \mu m K}{T[K]} \,. \tag{4.2}$$

The flux of atoms arriving at the substrate depends further more on the size of the evaporation source and on the angle as well as the distance between source and substrate. In the case of flux control of the chalcogen source this can in principle also be done *via* evaporation temperature. Practically, this is not possible in the setup used since the heat generated by the wire and the substrate heater will indirectly evaporate the chalcogen. This is also the reason why alloys of the sort $MS_{1-x}Se_x$ cannot be fabricated in a controlled manner in the used setup, since both S and Se will be evaporated at the same time. One way to avoid this is to use a so-called cracker cell consisting of two chambers allowing for flux control. However, this was not available within the time of this thesis.

Tungsten, molybdenum and tantalum wires were used together with co-evaporation of either sulphur or selenium for the fabrication of the TMDCs. In the evaporation chamber, two metal wires could be installed simultaneously in order to produce mixed $Mo_{1-x}W_xS_2$ layers or $MoS_2/TaS_2$ heterostructures. All four semiconducting TMDCs as well as metallic $TaS_2$ can be produced. The metal wires were installed in a slight angle to the growth substrate. The growth substrate itself was facing downwards and could be heated to temperatures around 450 °C. Evaporation was performed at a base pressure of $10^{-6}$ mbar.

### 4.2.2 Characterisation of TMDC monolayers

There are two possibilities to control the amount of metal and therefore the number of layers on the substrate, the impinging flux and the number of pulses together with their duration. In practice, a fixed power and thus flux was chosen as well as a fixed pulse period, so that the number of layers is controlled by the number of pulses. S or Se was usually evaporated during the whole time of the deposition process. In order to calibrate the thickness and to obtain monolayers, it is possible to use PL and absorption as a quick and non-destructive method. For this, a series of TMDC thin layers with varying number of pulses was fabricated. Since the monolayer exhibits a direct band gap, a certain number of pulses (for otherwise fixed parameters) exists for which the sample shows the highest PL signal. This sample can then be used as a reference for absorption spectra corresponding to an average monolayer. Figure 4.7 (a) shows PL and UV-Vis spectra of a series of $MoS_2$ with varying pulse count. It can be seen that the PL intensity first grows with the amount of deposited material and decreases again after too much metal was sublimed. The thickness is controlled by the absorbance spectra. One monolayer can then, in a first approximation, be linked to an absorbance value of $Abs = 0.11 \pm 0.01$ for the peak maximum around 2.9 eV in the case of $MoS_2$. Figure 4.7 (b) depicts the absorption spectra of the four TMDCs $MoS_2$, $MoSe_2$, $WS_2$ and $WSe_2$ grown with PTD. All spectra show the typical transitions as manifested by the distinct peaks in the absorption spectra. Most of the growth optimisation was done on $MoS_2$. Therefore, the

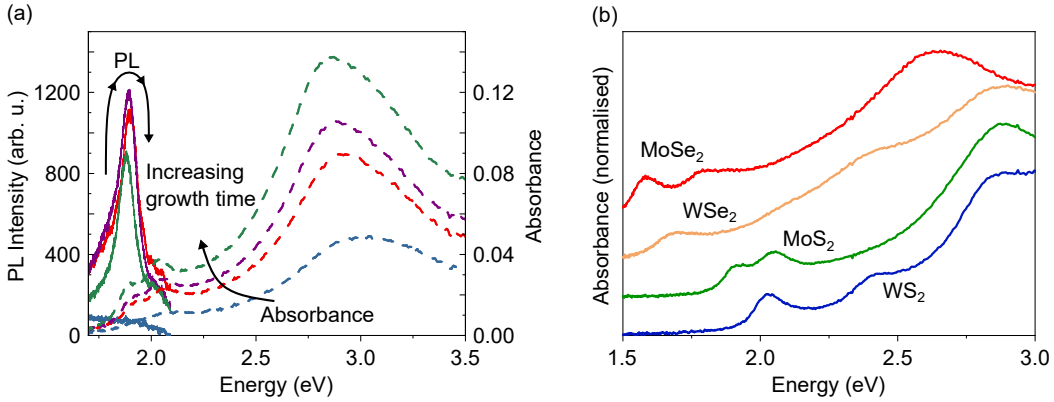


Figure 4.7: (a) PL and absorbance evolution of $MoS_2$ for an increasing number of pulses. The maximum PL is seen for an absorbance of 0.1 at 2.9 eV and shown in violet (b) Absorbance spectra of the four TMDCs corresponding to one monolayer. The typical excitonic absorption features are seen.

remainder of this subsection will focus on this specific TMDC.

PL measurements give a first and fast indication when having deposited a monolayer, but a direct thickness measurement is preferable. Atomic force microscopy (AFM) is usually used to determine the thickness of thin films. In the case of $MoS_2$ deposited on quartz or sapphire substrates, AFM measurements did not give conclusive results. This might have been due to either a too high roughness of the substrate itself or the lack of large enough individual crystallites. TEM cross section images were therefore taken. One example of $MoS_2$ on an $SiO_2$/Si substrate is shown in figure 4.8. TEM reveals that the films are, to a large extend, comprised of monolayers but that there are also parts where two or more layers overlap. Moreover, the grain size of single crystallites is found to be around 10 nm with no preferential in-plane growth orientation. In conclusion, for the utilised growth conditions, continuous TMDC monolayer films can be grown which follow the topology of the substrate and consist of small crystallites with no in-plane long range order and a large amount of grain boundaries. Considering the ease

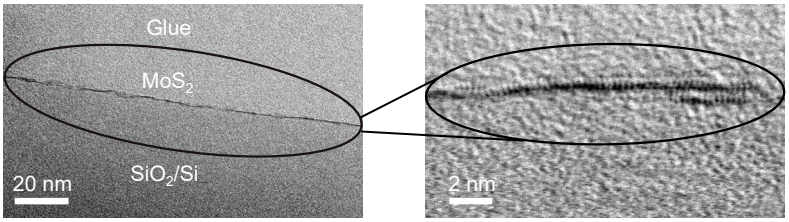


Figure 4.8: STEM cross-section of $MoS_2$ on $SiO_2$/Si. The film consists of mainly small (≈10 nm) monolayers with occasional overlap between layers as seen in the magnification.

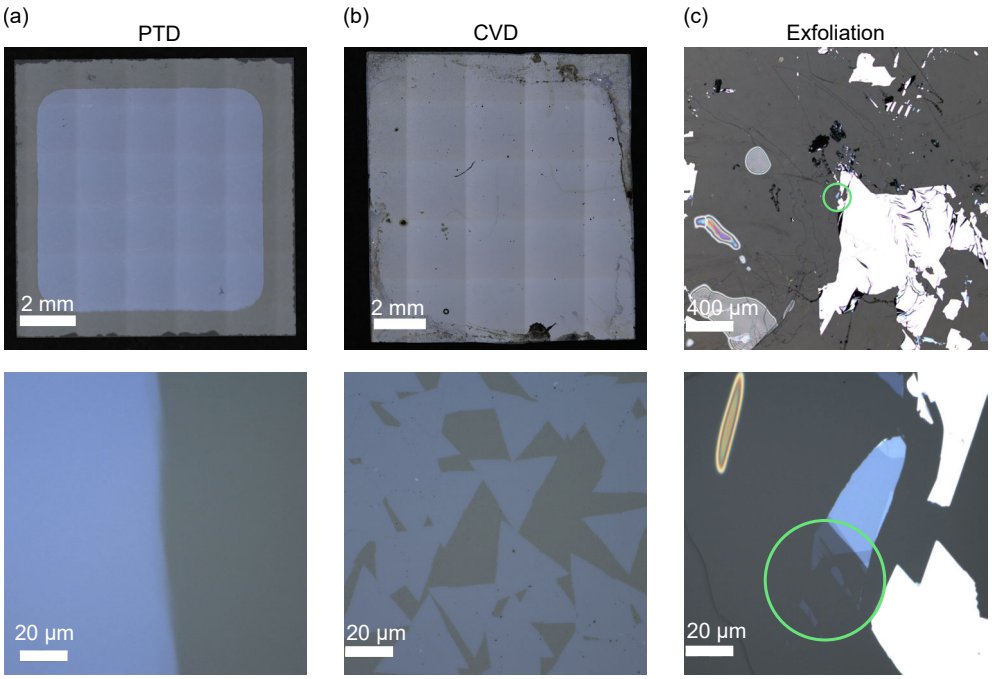


Figure 4.9: Optical microscope images of $MoS_2$ obtained by the three methods as described in the text. (a) The PTD monolayer film covers the whole substrate (10 x 10 $mm^2$). No structure can be seen with the optical microscope. The contrast between quartz substrate and $MoS_2$ on one edge is demonstrated in the lower panel. (b) Image of a commercially purchased CVD sample. The sample is fully covered except for the edges where individual triangles can be found. (c) Exfoliated $MoS_2$ on mica. The monolayer region is circled and shows a slight blue contrast. Thicker regions appear more blue and bulk parts shiny white.

of the fabrication method and possibility of implementation into a designated MBE system, these results are promising. Next, the optical properties will be discussed in more detail in comparison to commercial CVD-grown and mechanically exfoliated $MoS_2$.

Figure 4.9 compares optical microscope images of representative samples for each of the differently obtained TMDCs. Reflectance microscope images can serve as the first indication and identification of monolayers since already a single layer shows distinguishable contrast on many of the used substrates. Furthermore, different number of layers can be identified by their colour, as can be seen in the case of the exfoliated sample. The first image depicts a sample grown with PTD. No structure can be seen as expected from the small grain size established by TEM. Rather, a closed single layer thick film is obtained. The middle image shows a commercially purchased $MoS_2$ monolayer produced by chemical vapour deposition. At the edges of the sample, individual triangles can be observed as typical for CVD-grown

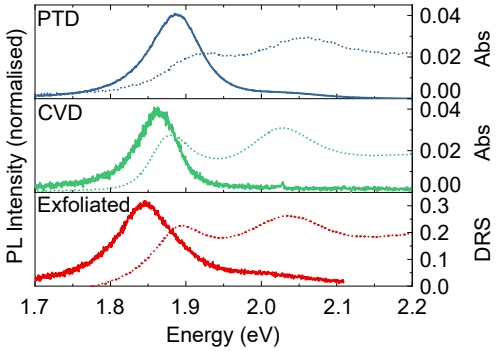


Figure 4.10: Room temperature PL and absorbance (DRS) spectra of the three differently obtained $MoS_2$ in the region of the A and B excitons.

monolayers. The triangles merge together to form a closed polycrystalline film over the range of cms. The exfoliated sample, as represented by the third image, was obtained by cleaving a sheet of mica in the glovebox to obtain a clean surface. The same was done with a bulk $MoS_2$ crystal. Both clean surfaces were then pressed together and separated again. This method, developed for the exfoliation of graphene [211], leads to flakes of a few tens of μm in size, but the yield is rather low and the identification of monolayers is time consuming. Nonetheless, $MoS_2$ exfoliated from bulk crystals can be of high quality and can be used for fundamental understanding as well as reference. A comparison of room temperature absorption and PL spectra in the region of the A and B exciton can be found in figure 4.10. The 'absorption' spectrum of the exfoliated sample was obtained by using differential reflectance spectroscopy which is related to the absorption for samples deposited on transparent and non-interacting substrates. However, the absolute values of the absorbance and DRS spectra cannot be directly compared, since the dielectric function of the mica substrate is not known. In the case of the absorbance spectra of the PTD and CVD sample, it can be seen that their absorption is very similar. This is further proof of the monolayer nature of the PTD fabricated sample. Also, the difference between the A and B exciton transition is found to be the same in all samples with approximately 144 meV. This value is consistent with literature [115]. On the other hand, it can also be observed that the PTD sample is shifted in absorption to higher energies by about 40 meV and 26 meV as compared to the CVD and the exfoliated sample, respectively. This effect might be caused by compressive strain which was shown to increase the energy gap [119]. The exact reason for the blue-shift is not clear, but it was consistently observed for the PTD samples grown on quartz. A striking difference between the three samples is the increased linewidth and the less sharp transitions of the PTD absorption. A reason for this can be the reduced crystallinity of the PTD sample due to the comparable low growth temperature with respect to CVD grown samples ($\sim$ 450 °C and $\sim$ 700 °C, respectively). As a consequence, the

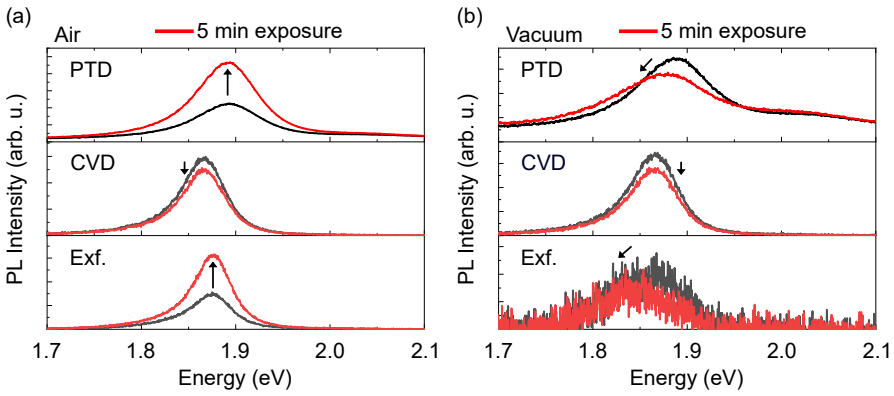


Figure 4.11: The effect of continuous laser exposure on the PL under ambient air (a) and in vacuum (b) for five minutes. The excitation energy was 2.82 eV.

PTD samples show a larger inhomogeneous broadening due to a higher variation in transition energies. This is partially also reflected in the linewidth of the PL. However, PL of $MoS_2$ consists, to a varying content, also at room temperature of a contribution of trions. This can, for example, be seen for the exfoliated sample where a shoulder at 1.88 eV is observed which can be attributed to the exciton PL. The Stokes shift, as taken from absorption to emission peak maximum, is the smallest for the CVD grown sample (19 meV), followed by the PTD sample (34 meV) and the exfoliated one (48 meV) due to the apparent larger contribution of the trion. An enhancement of the exciton PL was reported in literature when the TMDC is exposed to oxygen and water molecules [146]. To test this on our samples, the effect of ambient air on the PL in comparison to measurements in vacuum were performed. The results are presented in figure 4.11. On the left-hand side the effect of continuous laser excitation for five minutes in ambient air is displayed. For the PTD samples as well as for the exfoliated $MoS_2$, an increase in PL intensity in ambient air is seen. The PL intensity in vacuum drops to about 0.4 and 0.05 of its value in air for the PTD and exfoliated sample, respectively, and shows a slight red-shift. The CVD sample shows a slight decrease in its PL intensity after 5 minutes of laser excitation under both measurement conditions. But also for the CVD sample, a decrease of the PL intensity in vacuum as compared to air is seen, albeit with a factor of around 0.6 smaller than the other samples. Altogether, the behaviour of the CVD sample is found to be more robust against the effect of ambient air. An explanation for the effect of ambient air on the PL properties of $MoS_2$ is the depletion of excess carriers by $O_2$ and $H_2O$ leading to a reduced trion and enhanced exciton emission and the passivation of gap states [145–148]. One can therefore assume that the exfoliated and PTD samples studied here exhibit a higher defect density than the CVD sample. Especially the exfoliated sample shows a strong decrease of the PL intensity when measured in vacuum. While the exact reason is not known, it might also be

related to a high defect density in this particular sample. It was shown that PL linewidth and Stokes shift as well as the amount of trion PL depend on the underlying substrate [157–159]. Since the three samples were deposited on different substrates, a direct comparison is only qualitatively possible here. Nonetheless, a few conclusions can be drawn from the comparison of the optical properties of the PTD, exfoliated and CVD samples. First, that the PTD films consist of a large number of tens of nm big crystallites which results in many grain boundaries and broader excitonic features as observed in the other two. Second, despite this, the optical properties regarding PL and absorption are very similar, also with respect to the behaviour in ambient air, and the PL intensity is comparable. Clearly, the growth process needs more optimisation in terms of crystal domain size, but the results highlight the facile fabrication of closed, large-area monolayer TMDC films. A major advantage of the presented method is the possibility of the controlled co-evaporation of other metals as dopants or the assembly of alloys and heterostructures in a vacuum environment. This will be exemplified in the next subsection for the case of $Mo_{1-x}W_xS_2$ mixed films and $MoS_2/TaS_2$ heterostructures after a short outlook on the growth optimisation.

Yang *et al.* reported the positive effect of sodium in terms of soda lime glass on the growth of large area $MoS_2$ monolayers [212]. Soda lime glass was therefore also tested with PTD to

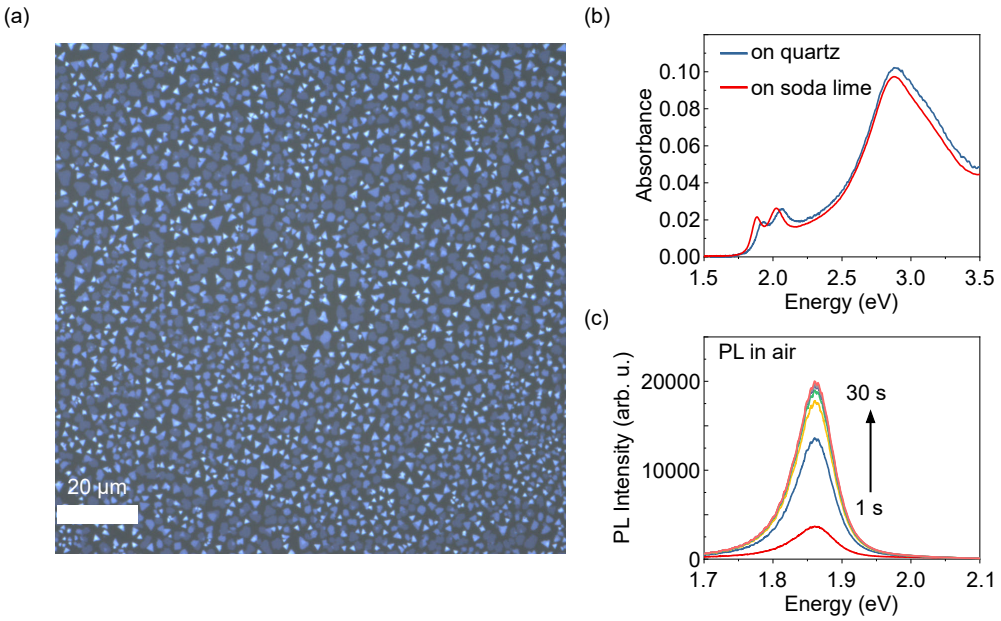


Figure 4.12: $MoS_2$ grown on soda lime glass. (a) Microscope image showing larger grain size of a few µm. (b) Comparison of the absorbance spectra of soda lime and quartz grown samples (c) PL spectra of an $MoS_2$ sample on soda lime glass under ambient conditions. Spectra were taken every five seconds for one second exposure time.

study its possible impact on crystal size. Figure 4.12 (a) shows a microscope image of $MoS_2$ grown on soda lime glass. A clear increase in grain size is observable compared to $MoS_2$ grown on quartz glass under the same conditions.

A trend of increasing grain size with growth temperature was found which is limited to about 500 °C by the low glass transition temperature of soda lime and downwards facing substrate. Sharper exciton peaks and a shift towards lower energies is seen in the absorption of the soda lime sample compared to the quartz one. The PL intensity is also found to increase by more than an order of magnitude. This increase is accompanied by a higher sensitivity to ambient air than seen for the sample on quartz. Samples showed a rise in PL intensity under laser excitation of around five times over a few tens of seconds before saturating. Until the end of this thesis it was not possible to find the cause of the high sensitivity of the PL intensity to ambient air. Complementary measurements like TEM to study the structure and possible defects need to be left for future work.

### 4.2.3 TMDC alloys and heterostructures

As introduced before, it is possible with the PTD method to evaporate different transition metals during the same growth process. Hence, it is possible to deposit mixed crystals and heterostructures without the need to break the vacuum. This gives the opportunity to tune the band gap as well as spin-orbit coupling. To demonstrate the feasibility of PTD, the mixed crystal $Mo_{1-x}W_xS_2$ was grown for x = 0..1 as well as $MoS_2/TaS_2$ heterostructures. Alloys of either mixing the metal (Mo and W) or the chalcogen (S or Se) and various heterostructures have been grown by employing different methods before [213–219]. The purpose of this study is to show that a controlled deposition method for varying mixing ratios and abrupt atomic interfaces using PTD under high vacuum is possible. Mo was co-evaporated with W either at the same time or subsequently. The ratio of Mo/W was adjusted by the time current flows through the respective wire. $MoS_2$ has a smaller band gap and SOC than $WS_2$ which manifests itself in a distinguishable optical response. Figure 4.13 demonstrates the transition between $MoS_2$ and $WS_2$ by measuring absorption and PL in dependence of $x$. The amount of Mo and W in the samples was derived using X-ray photoelectron spectroscopy (XPS). The integrated areas of the corrected Mo $3P$, W $4f$ and S $2p$ atomic core levels were compared to determine the composition. For an increasing W/Mo ratio, both characteristic A and B exciton features in absorption are gradually shifted. Most importantly, no sign of phase separation is observed that would manifest itself in a mixed signal of the respective A and B exciton transitions of pure $MoS_2$ and $WS_2$. It is seen that the shift is not monotonic in the case of the A exciton, but first shifts to the red with consecutive increase in energy. The B exciton also exhibits bending, but is monotonically increasing. Usually, the evolution of the band gap in semiconductor alloys

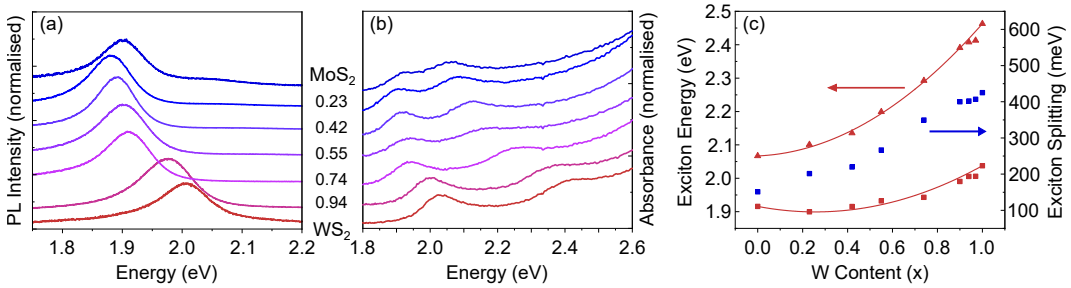


Figure 4.13: PL (a) and absorbance (b) spectra of $Mo_{1-x}W_xS_2$. The value for $x$ is shown in-between. (c) Evolution of the A and B exciton energy and the A-B splitting with respect to $x$ (modified from [99]).

is fitted with the non-linear formula

$$E_g(x) = (1-x)E_{MoS_2} + xE_{WS_2} - bx(1-x)\,, \tag{4.3}$$

where $E_g$ is the band gap of the alloy as a function of $x$, $E_{MoS_2}$ and $E_{WS_2}$ are the band gap energies of $MoS_2$ and $WS_2$, respectively and $b$ is a bowing parameter. In order to fit the data with the above equation, it is assumed that the exciton transition follows the band gap behaviour. This assumption is so far justified since exciton binding energies of different TMDCs are similar to each other. The fit resulted in bowing parameters of $b_A = 0.25 \pm 0.03\ eV$ for the A exciton and $b_B = 0.37 \pm 0.03\ eV$ for the B exciton. The value for the A exciton agrees well with literature also quantitatively in experiment and DFT calculations [218, 220]. Qualitatively, also the behaviour of the B exciton is reproduced in our measurements, however, the bowing parameter obtained here is larger. This might be attributed to the different method of obtaining the B-exciton energy as compared to literature. While Chen *et al.* [220] used PL, absorption spectroscopy was employed here which might lead to different absolute values of the B exciton energy. A different behaviour of the A and B exciton could hint to an unequal evolution of the SO-split bands that can be of interest for investigating bright and dark excitonic states as pointed out by Wang *et al.* Opposed to their finding in $Mo_{1-x}W_xSe_2$, a bowing of the energy difference between the A and B exciton, i.e. the SO splitting, is not observed here [221]. Rather a monotonic increase from 150 meV to 425 meV going from pure $MoS_2$ to $WS_2$ is seen as demonstrated in figure 4.13. A more thorough theoretical analysis is needed to gain more insight, but is out of the scope of the present study. From figure 4.13, it is also seen that the PL follows the shift of the A exciton absorption. A similar bowing parameter of 21 meV was derived. The PL intensity, linewidth and Stokes shift is similar in all compositions indicating no disorder introduced by alloying. By employing Raman spectroscopy, it is also possible to track the gradual transition of the alloy composition. The two characteristic vibration modes

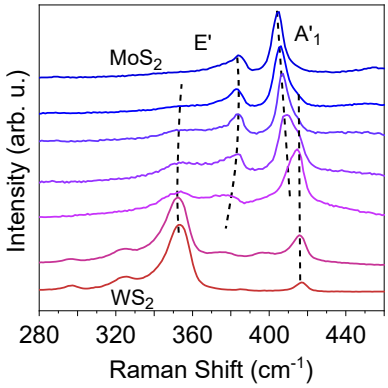


Figure 4.14: Raman spectra of the $Mo_{1-x}W_xS_2$ alloy. The composition is the same as in 4.13. The broken lines are a guide to the eye for the evolution of the two vibrational modes (adapted from [99]).

$A_1'$ and $E'$ are demonstrated in figure 4.14. For $MoS_2$ $E'$ ($A_1'$) is found at 384.0 $cm^{-1}$ (404.5 $cm^{-1}$) and for $WS_2$ at 353.5 $cm^{-1}$ (417.0 $cm^{-1}$). These values are consistent with the reported wavenumbers for monolayers in literature [181]. In the evolution of the two vibrations, one can observe a clear two-mode behaviour for the energetically lower $E'$ mode. That is, both modes of $MoS_2$ and $WS_2$ exist separately in the mixed crystals with a composition dependent shift of their respective frequencies. The $E'$ mode is shifted to lower wavenumbers in $MoS_2$ while it is opposite for $WS_2$. In the case of the $A_1'$ mode, sulphur atoms oscillate out of plane while the metal atom is stationary. As a consequence, the vibrational energies of this mode for the two TMDCs are similar since the bond lengths of the two TMDCs are alike. For our measurements, we can also assign two separate modes corresponding to the individual $MoS_2$ and $WS_2$ $A_1'$ modes, as can be seen from the shoulders in the Raman spectra. While the $MoS_2$ mode shifts to larger wavenumbers, the $WS_2$ mode shifts to lower ones. A clear separation of the two modes is also observed by Zhang *et al* [217]. On the other hand, literature also describes a one-mode behaviour of $A_1'$, meaning a gradual shift between x = 0 and x = 1 of only one merged mode [222]. This might be ascribed to the relatively large linewidth compared to the energy separation between the $MoS_1$ and $WS_2$ $A_1'$ mode. In the measurements by Chen *et al.* [222] one might also argue that two modes are indeed present. It is thus concluded that a two-mode behaviour is given for the $E'$ as well as for the $A_1'$ mode.

As a next step, the fabrication of a $TaS_2/MoS_2$ heterostructure is discussed. $TaS_2$ can be grown in the same way as the semiconducting TMDCs, but shows metallic properties. This makes thin films of $TaS_2$ interesting as semi-transparent electrodes in TMDC devices. The work function of $TaS_2$ is around 5.5 eV making it a possible alternative to indium tin oxide (ITO) [223, 224]. In order to establish its general applicability, absorption and sheet resistance

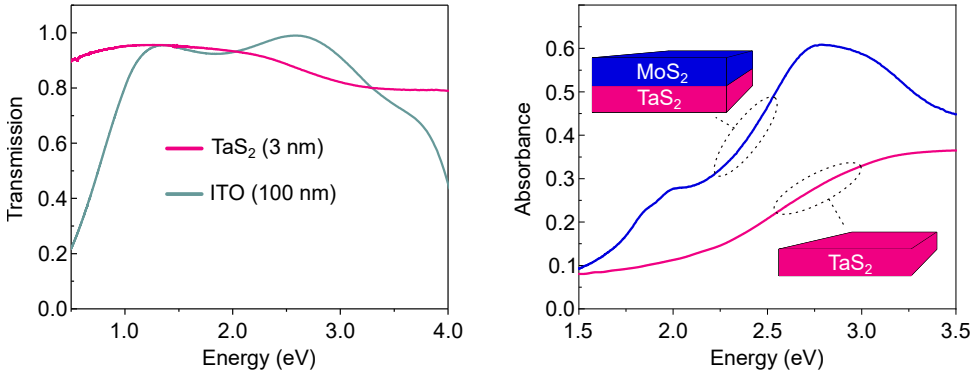


Figure 4.15: (a) Transmission of a thin film of $TaS_2$ and ITO on glass. (b) Absorbance spectrum of bare $TaS_2$ and a $TaS_2/MoS_2$ heterostructure. The $MoS_2$ A and B exciton are clearly visible. Adapted from [99].

of a 3 nm thin film was measured. The sheet resistance was measured with a four-point probe station to be 2 k$\Omega/\square$ equivalent to a conductivity of $1.7 \times 10^5$ S/m. While the sheet resistance is approximately two orders of magnitude larger than for ITO films used in devices due to the ∼30x thicker ITO, the conductivity value is compatible [225]. $TaS_2$ and ITO transmission is compared in figure 4.15. The $TaS_2$ thin film shows good transparency over the entire visible range ($T \geq 0.8$) and a much less pronounced falloff in the NIR spectral region compared to ITO. One advantage of $TaS_2$ is the easy co-evaporation with other TMDCs like $MoS_2$ to form heterostructures or contacts without the need of breaking the vacuum. As a proof of concept of the applicability of $TaS_2$, $MoS_2$ was grown on $TaS_2$ and the absorbance was measured (Figure 4.15). Importantly, the characteristic A and B excitons are also visible in the heterostructure showing that $MoS_2$ is grown in the semiconducting polymorph on $TaS_2$. A TEM cross-section is shown in figure 4.16. Few-layer $TaS_2$ was deposited on $SiO_2$ and subsequently a few $MoS_2$ layers were evaporated on top. From the TEM images, it can be seen that the interface between the two TMDCs is abrupt and atomically sharp. This is also highlighted by energy-dispersive X-ray spectroscopy (EDXS) with Ta confined to the lower part of the heterostructure. Further, $MoS_2$ exhibits small grains as indicated by the discontinuous lines. This behaviour is similar to the growth of monolayers directly on quartz but with a smaller contribution of the substrate roughness. The corrugation of the substrate is levelled out by $TaS_2$ after a few monolayers. Employing image contrast simulation, it was found that $TaS_2$ and the $MoS_2$ on top do not show the same in-plane orientation but are rotated to each other.

To summarise this section, it was shown that TMDC monolayers can be deposited in continuous films with an easy to implement physical vapour deposition method. To show its versatility, $Mo_{1-x}W_xS_2$ alloys were grown over the whole composition range and its optical

properties were discussed. $TaS_2/MoS_2$ heterostructures were successfully grown with atomically sharp interfaces and structural integrity of the two TMDCs.

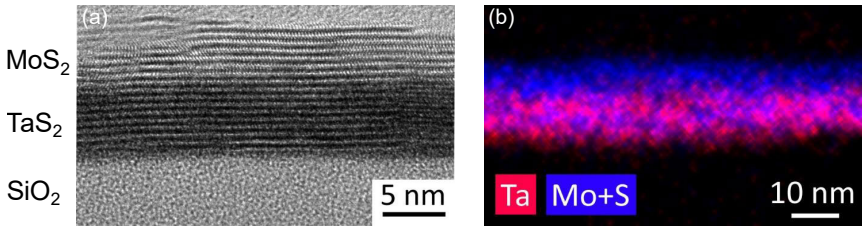


Figure 4.16: (a) TEM cross-section of a $TaS_2/MoS_2$ heterostructure demonstrating the sharp interface between the two components. (b) EDX spectra for Ta and Mo+S (Modified from [99]).

## 4.3 The influence of the substrate

The immediate surrounding of the monolayer plays an important role in its optical as well as electric properties due to the two-dimensional nature of the TMDCs. In this respect, the used substrate can induce changes also in the case when no apparent interaction, like charge transfer or a permanent dipole, are present. As pointed out in the fundamentals, this can be explained by the effect of the dielectric screening caused by the immediate TMDC environment. As a consequence, the single particle band gap is renormalized and the exciton binding energy is modified. In this section, it will be shown how the exciton transition energies ($E_{opt}$) can be determined optically by reflection measurements of TMDCs on various substrates with different dielectric constants. Together with PES experiments one can observe the effect on the single particle band gap ($E_{gap}$) and deduce the exciton binding energies.

### 4.3.1 Differential reflectance spectra of $MoS_2$ and $WSe_2$

Differential reflectance spectroscopy (DRS) is a method which allows to derive the complex dielectric function of thin films with thickness $d$ *via* two comparative reflection measurements. The DRS signal is defined as

$$DRS = \frac{R - R_0}{R_0} \,, \tag{4.4}$$

where $R$ and $R_0$ are the reflectivity spectra of the substrate with and without thin film, respectively. If the complex dielectric function $\sqrt{\epsilon} = \tilde{n} = n + i\kappa$ of the substrate is known, one can deduce the dielectric function of the thin film. This is done by employing the transfer matrix method and modelling the thin film response with a Lorentz oscillator model. In this

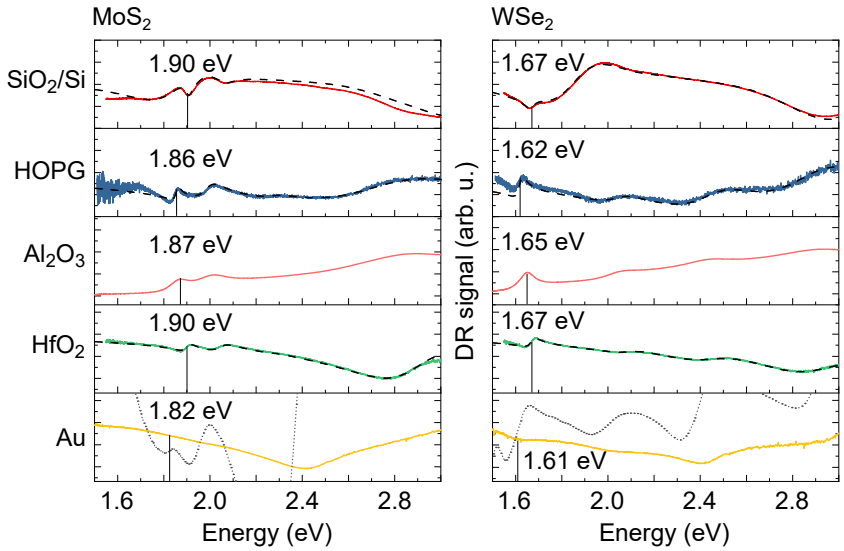


Figure 4.17: DR spectra of $MoS_2$ and $WSe_2$ on five different substrates. The dashed line shows the transfer matrix fit and the dotted line depicts the first derivative in the case of gold as the substrate. The A exciton transition energies are highlighted by the vertical line.

way, the theoretical DR spectrum is matched with the measured one. Details on the model and the theoretical background can be found in the experimental section of chapter 2.

The two TMDC monolayers $MoS_2$ and $WSe_2$ were deposited on five substrates: 340 nm $SiO_2$ on Si, $Al_2O_3$, 30 nm $HfO_2$ on Si, graphite (HOPG) and gold. The measured DR spectra are shown in figure 4.17. Transfer from the growth substrate to the new substrate was done in the group of Lain-Jong Li in a similar way as the wet transfer described in the methods section, but with PMMA instead of PS [38, 226]. For the TMDCs on $Al_2O_3$, it is possible to directly read-out the transition energies of the A and B exciton since the DRS signal for non-interacting and transparent substrates is directly proportional to the extinction coefficient $\kappa$ of the TMDCs [31]. In the case of gold as a substrate, only a small signal was observable for the excitons. The transition energies were determined by forming the first derivative and taking its inflection point, as shown by the broken line. For the other substrates the transfer matrix method was employed. The exciton transition energies are marked in the figure by vertical lines. It can be seen that the A exciton transition energy stays approximately constant for the oxide substrates but is red-shifted when the TMDCs are deposited on HOPG and Au by a few tens of meV. Figure 4.18 shows the energy levels as measured by PES for the samples on sapphire and gold. An energy gap of 2.11 eV and 1.90 eV was found for $MoS_2$ on $Al_2O_3$ and Au, respectively and similarly 1.89 eV and 1.75 eV for $WSe_2$. This results in exciton binding

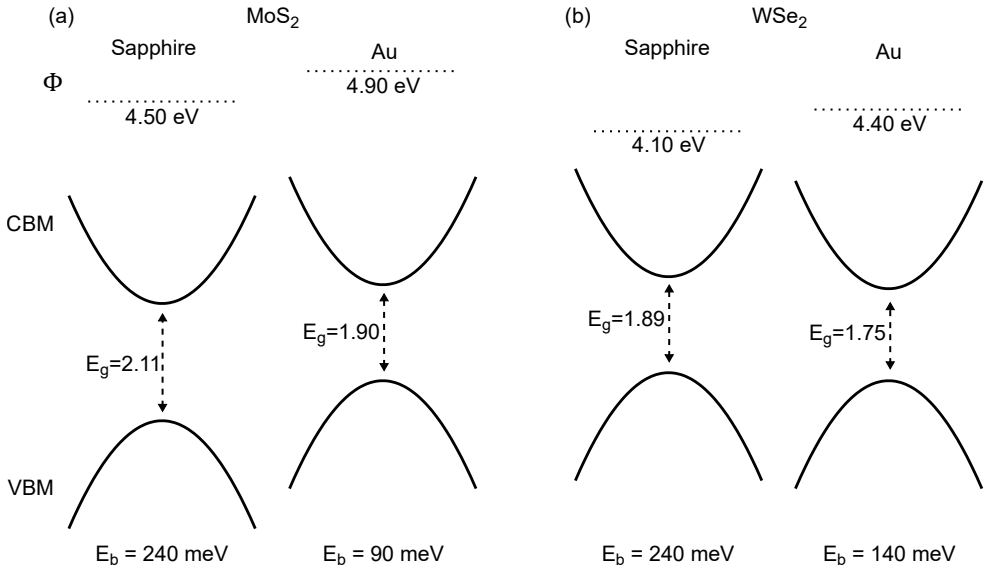


Figure 4.18: Energy levels and deduced exciton binding energies of $MoS_2$ (a) and $WSe_2$ (b) on sapphire and gold substrates. Adapted from [38].

energies given by $E_b = E_{gap} - E_{opt}$ of 240 meV and 90 meV in the case of $MoS_2$ on $Al_2O_3$ and Au and 240 meV and 140 meV for $WSe_2$. This reduction of $E_{gap}$ and $E_b$ is partially ascribed to a larger screening of the Coulomb interaction when the TMDCs are deposited on Au. Another effect leading to a renormalisation of the band gap could be due to a small charge transfer from the TMDCs to Au [227]. The difference in the change of $E_{gap}$ arising between $MoS_2$ and $WSe_2$ can be attributed to a hybridisation of the $MoS_2$ VBM at the Γ-point with Au leading to a distortion and reduction of $E_{gap}$ at $K$ [38, 228].

As discussed in section 4.1.5, the dielectric surrounding of the TMDC monolayers will influence the screening of charge carriers and thereby $E_{gap}$ and $E_b$. Since the dielectric function is frequency dependent, the question is which value is relevant. As a starting point, the frequency corresponding to $E_b$ is used for excitons [33]. For TMDCs this lies at around 200 meV which is slightly above the phonon energy of the oxides studied here. Also, for the oxides it holds that $\kappa \approx 0$ in this energy range. $n$ changes smoothly only by around 15 % between the value for $E_b$ and $E_{gap}$ so that values of the relative dielectric constant within this range seem reasonable. The larger screening of the Coulomb interaction, that leads to a reduction of both $E_{gap}$ and $E_b$ when the TMDCs are deposited on Au, can be associated with free electrons. Gold has a plasma frequency well above the optical and binding energies considered here so that screening becomes effective [197]. A slight red-shift of $E_{opt}$ towards higher dielectric constants was predicted theoretically by Cho *et al.* [14]. In their study they used numerical values of the static dielectric constant of silica (≈4) and graphite (≈10). In order to compare the present

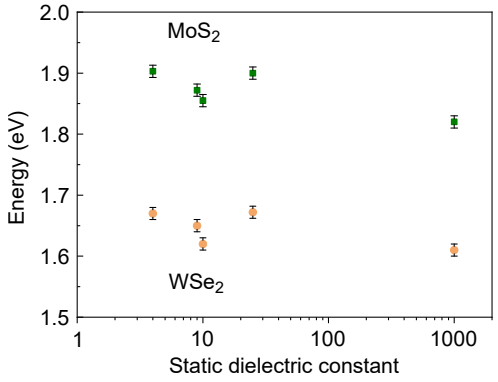


Figure 4.19: Transition energy of the A exciton ($E_{opt}$) of $MoS_2$ and $WSe_2$ in dependence of the static dielectric constant of the substrate. The value for the static dielectric constants used here are: 4 ($SiO_2$), 9 ($Al_2O_3$), 10 (HOPG), 25 ($HfO_2$) and the value for gold was set to 1000.

results with their theory, $E_{opt}$ is plotted against the substrate static dielectric constant in figure 4.19. $E_{opt}$ stays approximately constant within the error for the oxide substrates and slightly reduces for Au as the substrate. The samples on HOPG shows a reduced exciton transition energy of 40 - 50 meV as compared to samples on $SiO_2$. Hence, the transition energy lies not exactly in the trend of decreasing energy with increasing dielectric constant. This might be due to the usage of the static dielectric constant for HOPG instead of the dielectric function at the exciton binding energy. Additionally, $\kappa \neq 0$ at the frequency corresponding to $E_b$. The absolute value of the dielectric constant at this value is $|\epsilon_r| = \sqrt{\epsilon_r^2 + \epsilon_i^2} \approx 30$, which represents the trend better. However, more theoretical insight on the value of the used dielectric constant is needed here [120].

## 4.4 Summary and outlook

Within this chapter, a resistive heating method for the fabrication of large area TMDC monolayers was introduced. These monolayers showed comparable optical properties with respect to PL and absorption to mechanically exfoliated and CVD grown layers. The use of wires as source for the sublimation of the transition metals makes this procedure versatile and easy to implement in existing ultra-high vacuum (UHV) deposition chambers. By growing mixed monolayers of the type $Mo_{1-x}W_xS_2$, it is possible to tune the optical absorption and the spin-orbit splitting as manifested by the difference between A and B exciton. Furthermore, the subsequent deposition of metals makes it possible to grow heterostructures without breaking the vacuum. In such a way, $TaS_2/MoS_2$ slabs with sharp interfaces could be deposited, illus-

trating the possibility of $TaS_2$ as a semi-transparent electrode. Albeit heterostructures and mixed TMDC crystals and monolayers have been grown before by various methods, the fabrication using PTD highlights the facile and controllable growth in a UHV environment. In the future, the method at hand will allow the introduction of impurities, e.g. for doping or the controlled study of defect sites. These impurities can be observed for example by low temperature PL. Not only the substrate, but also adsorbed gas molecules influence the TMDC properties. Therefore, the growth and subsequent study of TMDCs without breaking the vacuum allow for a deeper insight into the intrinsic TMDC characteristics. PTD is a first step towards this direction. More control over the crystallinity and knowledge of the growth mechanism is, however, needed. Soda lime glass as growth substrate was shown as an example to improve $MoS_2$ grain size, but as-deposited monolayers lacked air-stability. An explanation for this is still missing and a deeper understanding is needed on how the substrate influences the TMDC growth.

Moreover, DR spectra of $MoS_2$ and $WSe_2$ were investigated on five different substrates with varying dielectric constants. By using the transfer matrix method, it was possible to extract the exciton transition energies also for multilayer and non-transparent substrates. The energy of the A exciton was found to slightly red-shift with increasing dielectric constant, an effect predicted by theory [14]. The shift is only small since both the band gap as well as exciton binding energy are affected simultaneously and almost equally by the dielectric screening of the surroundings. The presented optical investigations by DRS in combination with PES allow for the experimental determination of the relevant energies in dependence of the surroundings. This was exemplarily shown for sapphire and gold as the substrates. A clear reduction in the exciton binding energy and the band gap could be observed for the TMDC samples deposited on Au. While the principal theory of screening in two-dimensional materials can be found in literature, there are some open questions regarding the value of the surrounding dielectric function. These could be tackled and tested with an expanded combination for PES and DRS measurements. DRS allows further investigation of the complex dielectric function of TMDCs at low temperatures. Especially in conjunction with low temperature PL, it helps in understanding the emission and absorption processes with respect to defects and trions and the influence therein of the underlying substrate. In particular, when investigating small flakes or non-transparent substrates, DRS in combination with a microscope setup is a versatile technique to study the optical properties of TMDCs.

# 5 Excited state charge transfer in a hybrid $MoS_2/H_2Pc$ system

*In this chapter the findings presented in the publication* Excited-State Charge Transfer Enabling $MoS_2$/Phthalocyanine Photodetectors with Extended Spectral Sensitivity [39] *by N. Mutz, S. Park, T. Schultz, S. Sadofev, S. Dalgleish, L. Reissig, N. Koch, E. J. W. List-Kratochvil and S. Blumstengel are shown. The author contributed through the measurement and analysis of PL, absorbance, AFM images and fabrication of the hybrid samples. PES and XPS were performed and analysed by S. Park and T. Schultz in the group of N. Koch. S. Sadofev prepared $MoS_2$ samples. S. Dalgleish conveyed the TMDC transfer as well as the photoconductor design and measured and analysed PAS together with L. Reissig. E. List-Kratochvil and S. Blumstengel contributed to the analysis and interpretation of the data. S. Blumstengel and N. Mutz collected all the data and wrote the manuscript. All authors contributed to the final manuscript. The following chapter deepens the view on the properties of the individual materials as well as the combined system.*

After the introduction of two-dimensional transition metal dichalcogenides (TMDCs) in the previous chapter, this chapter will cover the combination and interaction of the inorganic TMDCs with organic molecules. The effect of molecules on the photoluminescence (PL) of the TMDCs will be extended. The motivation of bringing monolayer TMDCs and organic molecules together is the same one as for hybrid inorganic/organic systems with conventional three-dimensional semiconductors. An enhanced functionalisation is pursued by utilising charge transfer, carrier separation or energy transfer at the hybrid interface. The advantage of monolayer TMDCs is that they consist solely of surface without bulk due to their reduced thickness. They offer the prospect of being merged with organic materials for flexible opto-electronic devices. For instance, the organic molecules can serve as dopants, form diode structures with the TDMCs, enhance overall PL or absorption. The following chapter will introduce these aspects in more detail, using the review papers [179, 229] as starting point. Then, the experimental studies performed on TMDC/organic molecule heterostructures will be discussed. The main focus of this chapter lies on the $MoS_2$/Phthalocyanine system. Finally, preliminary

results of another TMDC/molecule structure will be shown in the last section.

## 5.1 Hybrid TMDC/organic systems - an overview

One important aspect when investigating the interface of two dissimilar materials is the alignment of their energy levels with respect to each other. In dependence on how the energy levels are aligned, different behaviour can be expected such as charge transfer and electron-hole separation or their accumulation. Therefore, before discussing the specific TMDC/organic heterostructures, a brief, but more general view is given regarding energy level alignment.

### 5.1.1 Energy level alignment

Energy level alignment describes how the highest occupied molecular orbital (HOMO) (or valence band (VB)) and lowest unoccupied molecular orbital (LUMO) (or conduction band (CB)) of two materials arrange to each other energetically. Thermal equilibrium is established when the two materials are brought into contact. An important measure here is the work function, that is the energy needed to remove an electron at the Fermi level to the local vacuum level just outside the solid. In that sense it is a surface related quantity only [230, 231]. The work function can be regarded as a combination of the bulk chemical potential $\mu$ and interface (surface) related potential changes caused by band bending and an interface (surface) dipole [232]. There exist some concepts to predict how the energy levels of two heterogeneous materials align when brought into contact. The simplest models are the Schottky-Mott and Anderson's rule for metal-semiconductor and semiconductor-semiconductor heterostructures, respectively. Both models take the equilibration towards a common chemical potential of the two materials in contact into account. But they consider the electron affinity and ionisation energy of the two materials when not in contact. The drawback of these models is that they do not consider any interfacial layer possibly existing between the two materials nor any density of states (DOS) inside the band gap [2, 233]. These states can lead to a pinning of the Fermi level. Provided a large enough density of these states, thermal equilibrium through charge transfer can be established with only small changes in the chemical potential. The DOS within the gap region can have different origins. Among these are tailing of the Gaussian DOS in the case of organic semiconductors [234], surface/interface states and metal induced gap states, dangling bonds, states caused by adsorbates, etc. [232, 233]. As a consequence of the above mentioned, tabulated values for the energy levels of different materials can serve as a starting point, but can only give a limited insight into the real energy level alignment. This needs to be measured experimentally. Irrespective of the reason for the resulting energy level alignment, mainly two types of semiconductor heterostructures are distinguished and shown in figure

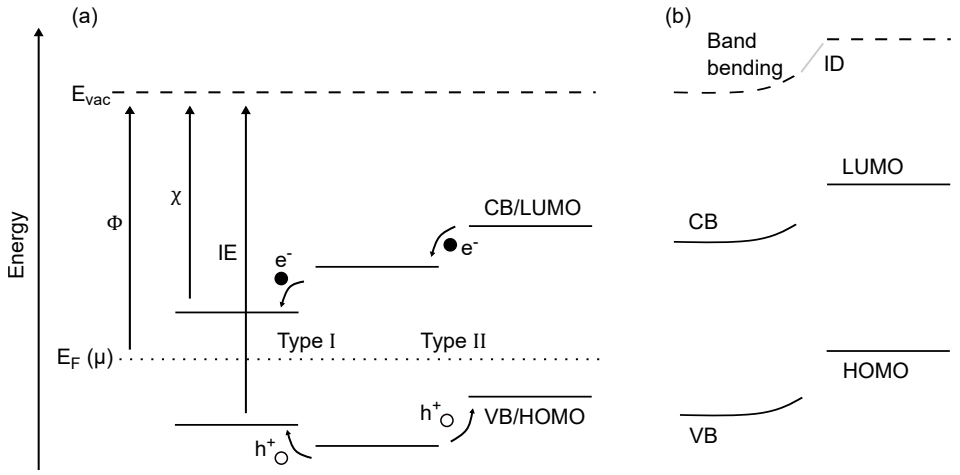


Figure 5.1: Example of energy level alignment at the interface of two dissimilar materials. (a) A type I structure is shown between the left and the middle material. The material in the middle and the right one form a type II heterojunction. In this case, but not in general, the vacuum levels ($E_{vac}$) are aligned. The case of not aligned $E_{vac}$ is shown in (b) where an upward band bending and an interface dipole (ID) are schematically drawn. $E_F$ describes the Fermi level (chemical potential $\mu$) with $\Phi$ as the workfunction. $\chi$ and IE are the electron affinity and ionisation energy, respectively. Electrons are depicted as $e^-$ and holes as $h^+$.

5.1. Type I (straddling) heterostructures are interesting for light-emitting applications. For these structures, the conduction and valence band of one of the materials are both within the band gap of the other one. Electrons and holes can, therefore, accumulate in the smaller gap material. Type II heterostructures are characterised by a staggered energy level arrangement, so that only either CB or VB are within the band gap of the other material. This is useful for the separation of electron and hole at the interface in photovoltaic or sensor applications.

### 5.1.2 TMDC/organic heterostructures - literature overview

The combination of monolayer TMDCs with organic molecules aims in two ways at enhancing the function of the TMDCs. One route is to improve the intrinsic properties of the monolayers itself. This can for example be done by passivating or curing defects and thereby increasing charge carrier mobilities or PL quantum yield. Another possibility is to dope the TMDC which increases room temperature conductivity. The other idea is to build heterojunctions where both materials contribute synergistically to the device function. A literature overview of the two ideas of what can be and has been done will be described in the following. Due to the vast amount of recent literature, only the most relevant one for this thesis will be presented.

As aforementioned, the majority of point defects in TMDCs are chalcogen vacancies. Molecules containing sulphur groups were shown to selectively bind to S-vacancies in $MoS_2$ [161, 235–237]. Different reaction pathways of the thiol-group representing molecule methanethiol ($CH_4S$) with sulphur vacancies were studied by Förster *et al.* [238] using density functional theory (DFT). It was found that the repair of sulphur vacancies is exothermic with only a low activation barrier. While the subsequent release of $CH_4$ from the $MoS_2$ lead to a restoration of the pristine band structure and Fermi level, the route where $CH_3S$ was still attached to the sulphur vacancy did not restore the Fermi level. This might hint to the necessity of removing any groups of the attached sulphur in order to complete defect healing. An increase in mobility through the healing of sulphur vacancies was observed in [161] and an enhancement in PL through thiol functionalisation was seen in [237]. Besides the repair of sulphur defects, the attachment of functional thiol groups was also used to shift the valence band position and work function by a few hundred meV [239] through charge transfer and introduction of a permanent dipole. Additionally, Sim *et al.* [240] treated $MoS_2$ with electron donating and accepting molecules which formed a self-assembled monolayer. An n- and p-type doping induced by the electron donating and withdrawing molecules, respectively, was inferred from PL and field-effect transistor (FET) measurements with an increase in electron density by ∼50% for n-type and a decrease by ∼25% for p-type doping. Doping was also investigated with other acceptor and donor molecules as described in the previous chapter with the observed changes in PL and FET characteristics [179, 229]. Charge transfer causes a shift in the TMDC energy levels. For example, electron transfer to the acceptor molecules C60F48 [241] and F6TCNNQ [242] was found to increase the TMDC work function and induce p-type doping. It was also observed that the underlying substrate plays an important role in the shift of the energy levels and the final energy level alignment, for example, by direct electron transfer from the underlying substrate to the acceptor molecules.

Manipulation of the energy levels leads to the other advertised hybrid structure. Organic/TMDC heterojunctions were studied with different small molecules and polymers already utilised in all-organic or other hybrid devices. Among these are C60 [243–245], pentacene [246–248] and tetracene [249], PTCDA [250–255], rubrene [256], PTB7 [257–260], C8-BTBT [261], rhodamine 6G [262, 263], TDBC [264] and phthalocyanines [12, 17–20, 265–273]. Herein, the phthalocyanines will be discussed further below in more detail in context of the discussion of the experimental findings of this thesis. In the case of C60 a type II energy level alignment was predicted theoretically between an $MoS_2$ monolayer and C60 with only small energy offsets which increased when exchanging $MoS_2$ with $WS_2$ [243]. $MoS_2$/C60 and $WS_2$/C60 composites haven been investigated by Baek *et al.* [245] and an increased charge separation after light excitation was found from time-resolved microwave conductivity experiments in the composites

as compared to the sole TMDCs. In their experiments, multilayer TMDCs fabricated by liquid exfoliation were used and were let to form aggregates with C60 in solution before film formation. To study the fundamental interaction at the hybrid interface, a more controlled deposition is needed, for example by vacuum deposition. This was done in the case of a pentacene/$MoS_2$ p-n junction with type II energy alignment which showed a photovoltaic effect [246]. Betis Homan *et al.* [247] found experimentally that excited charge transfer is fast. Transfer times of an excited hole from $MoS_2$ to pentacene were only a few ps. Similar observations have been made at the $WS_2$/tetracene interface with electron (from tetracene to $WS_2$) and hole (from $WS_2$ to tetracene) transfer times again of a few ps [249]. A type II energy level alignment was presumed from literature values of the separated constituents, but not measured. The electron and hole at the interface will form a so-called charge transfer (CT) exciton. The authors attributed an additional PL peak only visible in the hybrid sample below the band gap of both materials to a CT exciton. The effective PL lifetime of this CT state was substantially larger ($\approx$ 2 ns compared to 500 and 100 ps for excitons in $WS_2$ and tetracene, respectively) owed to the larger spatial separation. PTCDA is another small molecule often used in organic FETs and which was combined with TMDCs. Energy transfer from PTCDA to $MoSe_2$ was studied by Gu *et al.* [251]. An increased PL intensity and PL decay time of $MoSe_2$ together with a quenching of the PTCDA PL point towards energy transfer measured at around 30 % in efficiency. No energy level alignment was, however, given by the authors. A photodiode based on a vertical $WS_2$/PTCDA junction was looked at in [253]. A photoresponse stemming from both $WS_2$ and PTCDA was found as well as PL quenching of both materials. Charge transfer and subsequent electron and hole dissociation was concluded. The $MoS_2$/PTCDA interface was studied in [255] and [254]. Wang *et al.* [255] looked at the electrical current modulation in a FET configuration and a synaptic behaviour of the source-drain current with gate voltage was observed. Obaidulla *et al.* [254] looked at the PL of the heterostructure. An enhanced emission intensity and a more ordered growth of PTCDA on $MoS_2$ was seen but the explanation as well as their proposed type II energy level alignment need further consideration. The polymer PTB7 was used in conjunction with $MoS_2$ and fast charge transfer on the order of hundreds of fs to a few ps was found [257–260]. The proposed energy level alignment here again is of type II, although not directly measured of the two materials in contact. A study was performed by Cheng *et al.* [264] investigating energy transfer from J-aggregates of the cyanine dye TDBC to $MoS_2$. By varying the distance with sheets of h-BN, a transfer radius of approximately two nm was obtained.

## 5.2 Hybrid TMDC/organic systems - experimental results and discussion

In this section, the experimental findings of metal-free phthalocyanine ($H_2Pc$) interfaced with $MoS_2$ obtained during this thesis will be discussed. The focus of the first part will lie on existing literature of $MoS_2$/Pc structures before discussing the experiments. At the end of this section, an outlook with preliminary results will be shown for other hybrid TMDC/molecule structures.

### 5.2.1 Why TMDC/Pc heterostructures?

Phthalocyanines (Pc) are small $\pi$-conjugated molecules. The chemical structure of $H_2Pc$ is shown in figure 5.2, which was used in this thesis. Metals can be incorporated into the centre to tailor its electronic and optical properties. Pcs are of interest for organic photovoltaic and dye sensitised solar cell applications due to their high extinction coefficient in the red to near infrared spectral region. They possess good chemical stability, can be sublimed in vacuum and chemically modified to render them more soluble or influence the packing and crystallisation in the solid state [274, 275]. Utilisation of Pc derivatives in cancer treatment [276] and in combination with organic/inorganic perovskite solar cells as hole transport layer has been considered as well [277]. The first investigations of Pcs in combination with TMDCs were performed in the late 1980s with the study of CuPc deposited on freshly cleaved $MoS_2$ bulk crystals [278]. Motivated by the so-called van der Waals epitaxy, developed by Koma *et al.* in the mid 1980s [279], it was shown that CuPc grows with its own lattice constant and molecularly flat on $MoS_2$. Due to the weak van der Waals interaction between substrate and molecules, the electronic structure of the organic molecules was expected to be largely preserved in ultra-thin films which triggered more fundamental research [280–283]. More recent studies focused on monolayer TMDCs in combination with thin Pc films pursuing application in device geometries. A vertical heterojunction consisting of mono- and bilayer $MoS_2$ with a 30 nm thin film of CuPc was shown to display diode behaviour and a photovoltaic effect [17]. The molecular layer faced the light source and most of the electron-hole pairs were produced in the CuPc layer. After diffusion to the interface, charge separation was then attributed to happen at the CuPC/$MoS_2$ junction. Similar observations were made in a multilayer $MoS_2$/CuPc FET configuration [271]. The same authors reported on a reduction of the persistent photoconductivity present in $MoS_2$ FETs on $SiO_2$/Si in ambient air after deposition of CuPc [272]. This effect was explained by a combination of the passivation of $MoS_2$ against adsorbed oxygen which acts as an electron trap and the faster electron-hole recombination within and at the interface of $MoS_2$ and CuPc. Similar observations of a faster photoresponse of $MoS_2$ after the deposition of ZnPc were also

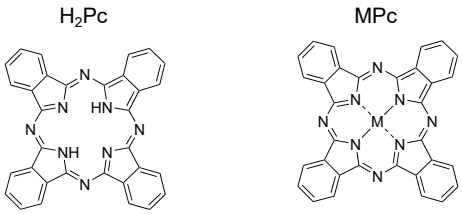


Figure 5.2: Chemical structure of metal-free phthalocyanine $H_2Pc$ on the left and metallated phthalocyanine (MPc) on the right. Various metals like Zn, Cu, Mg, Ni, Fe, etc. can be incorporated.

made by Huang *et al* [12]. Persistent photoconductivity in $MoS_2$ phototransistors ranging from several seconds up to hours has been reported [172, 174, 284–289]. The term refers to a higher conductivity of the $MoS_2$ channel with illumination even after the light is turned off. It has been ascribed to long-lived electron trapping and release by oxygen and water adsorbates and interface traps between substrate and $MoS_2$ [284, 287, 290–292].

With the observations of some electrical properties of the Pc/$MoS_2$ heterojunction by Valez *et al.* [17] and Pak *et al.* [271], more studies were devoted to the better physical understanding of the Pc/TMDC interface. Choi *et al.* [265] investigated mechanically exfoliated $MoS_2$, $MoSe_2$ and $WSe_2$ in combination with NiPc and MgPc. A decrease in PL intensity for $WSe_2$ after deposition of both NiPc and MgPc was observed. $MoSe_2$ showed only a decrease for NiPc and $MoS_2$ for neither of the two Pcs. The authors explained this behaviour with photoexcited electron transfer from the TMDC to the Pc. In the case of $WSe_2$, the conduction band lies above the LUMO of both Pcs. On the other hand, the CB of $MoSe_2$ lies in between the LUMO of NiPc and MgPc, whereas the CB of $MoS_2$ lies below the LUMO of both Pcs. Excited electron transfer is only favourable if the CB has a smaller energy (referenced to the vacuum) than the LUMO. No energy level alignment of the two materials in contact were, however, measured and literature values were taken as a reference. Charge transfer in the ground state was also looked at. No signatures were found in Raman and core level spectroscopy. A higher photocurrent for the TMDC/Pc systems, which showed PL quenching as compared to the pure TMDC, was reported in photoconductive atomic force microscopy (AFM) measurements and attributed to an enhanced charge separation. Excited state charge transfer was also studied by Kafle *et al.* [18, 268] between ZnPc and bulk as well as monolayer $MoS_2$. A fast decay of the ZnPc S1 state for a thin ZnPc film in the hybrid structure of less than 100 fs was observed for both bulk and monolayer $MoS_2$. This is much faster than what was found for a 10 nm thick ZnPc film that can be regarded as probing ZnPc only. In both investigated cases of bulk and monolayer $MoS_2$, a type II energy level alignment with the HOMO at smaller binding energy than the VB was derived from ultraviolet photoelectron spectroscopy (UPS) measurements. The CB

and S1 states were taken from literature and optical experiments, respectively. Hence, the fast decay was explained by efficient excited electron transfer from ZnPc S1 to the $MoS_2$ CB. For bulk $MoS_2$ as the substrate, a fast spin flip and back transfer to the T1 state in ZnPc of the electron was observed. In the case of monolayer $MoS_2$ such a mechanism was not found. Here, the delayed population of a new state was seen at approximately 1.2 eV and interpreted as the hybrid charge transfer (CT) state at the organic/inorganic interface. The difference between bulk and monolayer $MoS_2$ was explained by a larger band bending of ZnPc on the bulk $MoS_2$ which confines the hole in ZnPc closer to the interface. Also, the faster spin flipping in bulk $MoS_2$ and fast separation of the transferred charges away from the interface for monolayer $MoS_2$ were invoked. Fast electron transfer (ca. 10 fs) from ZnPc to $MoS_2$ was also predicted theoretically [269]. In a study by Padgaonkar *et al.* [19] charge transfer in a CuPc/$MoS_2$ and $H_2Pc/MoS_2$ heterostructure was investigated by transient absorption spectroscopy. Excited state electron transfer from CuPc and $H_2Pc$ to $MoS_2$ was $< 320$ fs when exciting only the Pc molecules. Fast dynamics ($\approx 800$ fs) were also found for selective excitation of the $MoS_2$. A combination between hole transfer from $MoS_2$ to the Pcs and resonance energy transfer from $MoS_2$ to the Pcs with subsequent electron back-transfer was proposed. A difference between CuPc and $H_2Pc$ was found in the recombination time of the transferred charges. While both, CuPc and $H_2Pc$, feature a time constant of around 4 ns, CuPc additionally showed a long lifetime component of 70 ns. An explanation given was that CuPc lies preferentially flat and stacks in a $\pi\pi$-like fashion which improves hole migration away from the interface while $H_2Pc$ grows in a mixed flat and upright manner. Both of these cited studies show that fast charge transfer processes occur at the Pc/$MoS_2$ interface. Together with the observations made for a reduction of the response time in FET phototransistors, the Pc/$MoS_2$ heterostructure is shown to be of relevance for sensing or photovoltaic applications. However, a few questions remain open and need more consideration. For one, in the studies by Kafle *et al.* [18] and Huang *et al.* [12] UPS was measured to obtain the $MoS_2$ VB and ZnPc HOMO positions, but the LUMO of the organic molecules was taken from optical measurements. This is of importance since large exciton binding energies are expected in TMDCs and phthalocyanines. Secondly, Amsterdam *et al.* [20] reported on an additional absorption feature slightly lower in energy than the absorption of the molecule. This was attributed to the charge transfer (CT) exciton of an electron in the $MoS_2$ CB and a hole in the Pc HOMO. A CT exciton is a bound state between an electron and a hole each located on opposite sides of the heterointerface. It forms when both electron and hole are spatially confined at the interface. The CT exciton can dissociate or recombine and therefore limit for example photocurrent generation in such heterostructures [293]. Usually these states have much lower oscillator strength and do not give a large absorption signal. Therefore, the measurement of the energy levels can test this

interpretation. As a third point, albeit larger photocurrents were measured in the hybrid structure compared to the neat $MoS_2$ [265, 271], direct proof was not shown that the transferred excited electrons can indeed contribute efficiently to the photoconductivity. A better knowledge of these points will therefore help understand the underlying physical interactions in the hybrid TMDC/Pc system better. Additionally, understanding this particular system can help tailoring the optoelectronic properties of similar hybrid structures.

### 5.2.2 Excited state charge transfer at the $MoS_2/H_2Pc$ interface

For the experiments performed within this thesis, a system consisting of $MoS_2$ and $H_2Pc$ was chosen. The reason for using $MoS_2$ is that it is the most frequently used TMDC in FET and photoconductor devices rendering it comparable to literature. Additionally, $MoS_2$ has the largest electron affinity of the four TMDCs [294] which makes it more likely that a type II heterostructure with $H_2Pc$ will be formed. The metal-free $H_2Pc$ was chosen since it shows a smaller intersystem crossing rate to the triplet state compared to the metal Pcs, like CuPc. Therefore, $H_2Pc$ has a higher PL quantum yield making it easier observable in PL experiments for studying decay dynamics [19, 295].

In order to establish the energy level alignment at the $MoS_2/H_2Pc$ interface and to gain understanding in possible transfer mechanisms, photoelectron (PES) and inverse photoelectron spectroscopy (IPES) was performed. The $MoS_2$ monolayer on $SiO_2$ was a commercially purchased closed layer (2D Semiconductors). Prior to the measurements, the $MoS_2$ was annealed overnight at 300 °C in ultrahigh vacuum to evaporate any residual water, minimise the influence of oxygen adsorbates and obtain a clean surface. The VBM and CBM of $MoS_2$ without molecules were measured at the K-point in **k**-space to observe the direct band gap. For the consecutive deposition of $H_2Pc$ on $MoS_2$, the HOMO and LUMO position was measured at the Γ-point, since band-dispersion of $H_2Pc$ is negligible. Additionally, any shift in the energy levels of $MoS_2$ due to an interface dipole would affect all the levels equally. Band distortion is expected to play only a minor role as it was not observed in a heterostructure of $MoS_2$ with the molecule F6TCNNQ. This acceptor molecule is expected to interact much stronger with $MoS_2$ than $H_2Pc$ [242]. Figure 5.3 shows the results of the UPS and IPES measurements. The ionisation potential and electron affinity of sole $MoS_2$ at the K-point are 5.7 eV and 3.6 eV, respectively. This leaves the band gap energy to be 2.1 eV. The workfunction is at 3.9 eV, i.e. 300 meV below the conduction band minimum reflecting the often observed n-type doping of $MoS_2$. A slight shift of 80 meV is seen in the workfunction upon growth of $H_2Pc$ molecules which saturates after 0.5 nm $H_2Pc$ were deposited. At this coverage, the HOMO level can be observed at 0.9 eV below the Fermi level. No shift in the HOMO was seen for further deposition of molecules up to 2 nm. The LUMO level was probed by IPES. The resulting ionisation

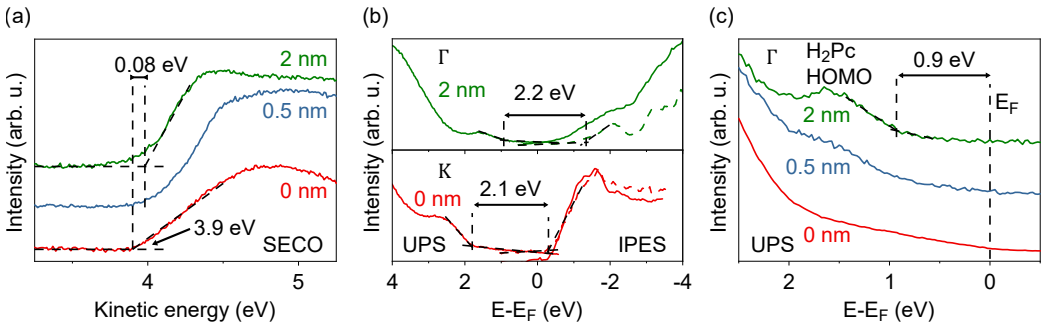


Figure 5.3: PES and IPES measurements of $MoS_2$ with increasing $H_2Pc$ thickness. (a) Secondary electron cut-off used to determine the workfunction. (b) VB and CB and HOMO and LUMO of $MoS_2$ and 2 nm $H_2Pc$ on $MoS_2$. The VB/CB was measured at the K-point while the HOMO/LUMO was recorded at normal incidence (Γ). CB and LUMO were deconvoluted for a more accurate determination of the energies (dashed lines). (c) Evolution of the valence features upon deposition of $H_2Pc$ at Γ. No shift in the $H_2Pc$ HOMO was seen for 0.5 and 2 nm thickness. Adapted from [39].

potential is 4.9 eV and the electron affinity is 2.7 eV for 2 nm $H_2Pc$ giving a HOMO-LUMO gap of 2.2 eV, slightly larger than the band gap energy of $MoS_2$ on $SiO_2$. These values agree with literature values [296]. The tiny shift in the workfunction after deposition of $H_2Pc$ is a sign of negligible charge transfer between $MoS_2$ and the organic molecules in the ground state. A conclusion substantiated by measuring the core levels *via* X-ray photoelectron spectroscopy (XPS). Again, no shift of the $MoS_2$ levels nor the $H_2Pc$ levels for increasing thickness was observed. As a consequence, the energy level alignment is well represented by the Schottky-Mott rule, i.e. vacuum level alignment. That means, at least up to the measured thickness, negligible formation of an interface dipole or band bending in the $H_2Pc$ film is observed. In the works by Huang *et al.* [12] and Kafle *et al.* [18], ground state charge transfer was observed for ZnPc deposited on $MoS_2$. Huang *et al.* showed a shift in the Mo 3d and S 2p core levels to lower binding energy upon deposition of ZnPc. Additionally, a shift in the VB closer to the Fermi level is observed with increasing ZnPc coverage. Both was interpreted as a depletion of excess electrons by ZnPc. This conclusion was supported by an increase in the ratio of free exciton to trion PL emission, a sign usually attributed to p-doping of $MoS_2$. However, no, or only a much smaller, change in the workfunction was seen implying a reduced ionisation energy or a reduced band gap. Further, ITO was used as a conducting substrate in their UPS and XPS measurements to reduce sample charging. Yet, an influence of the substrate on the underlying charge transfer mechanisms has been observed recently, in particular for conducting substrates [242]. These two points were not discussed by the authors and need to be taken into

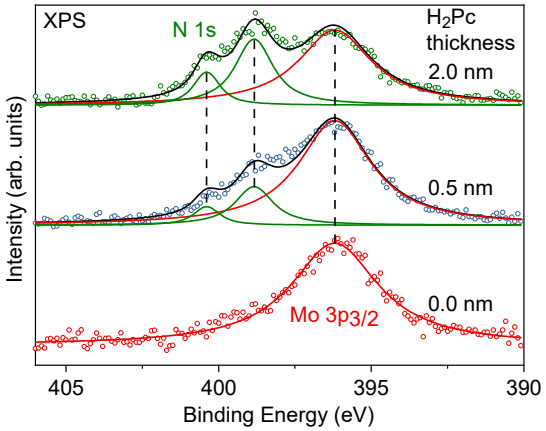


Figure 5.4: Core level spectra probed by XPS for 0, 0.5 and 2 nm $H_2Pc$ on $MoS_2$. No shift in the core levels of $MoS_2$ (Mo $3p_{3/2}$) or $H_2Pc$ (N 1s) was observed (modified from [39]).

consideration for the interpretation of ground state charge transfer. In the study by Kafle *et al.*, a shift in the HOMO position upon incremental deposition of ZnPc was seen and attributed to upwards band bending in the ZnPc layer towards the interface which implies rather an electron donating effect of ZnPc. Unfortunately, the change in workfunction for the individual deposition steps of the molecule is not apparent in their publication. It needs to be noted that in both these publications, the ZnPc molecules are deposited differently on the $MoS_2$. While Huang *et al.* immersed an $MoS_2$ monolayer in a solution of ZnPc dissolved in chloroform, in the study by Kafle *et al.* the molecules were sublimed in an ultra-high vacuum (UHV) chamber. Although in both cases ground state charge transfer might occur according to their data, some more detailed studies would be needed with incremental deposition of ZnPc. In the results of $H_2Pc$ on $MoS_2$ presented in this thesis, no sign of ground state charge transfer is seen. On the other hand, the type II energy level alignment as depicted in figure 5.5 renders excited state charge transfer energetically possible. With a VB/HOMO and a CB/LUMO offset of 0.9 eV and 1.0 eV, respectively, efficient hole transfer from the $MoS_2$ VB to the $H_2Pc$ HOMO and electron transfer from the $H_2Pc$ LUMO to the $MoS_2$ CB become likely.

In order to look more into the details of the interaction at the interface of the excited states of the two materials, PL experiments were performed. Figure 5.6(a) shows the absorbance and PL spectra of individual $MoS_2$ grown on quartz by pulsed thermal deposition and the spectra of a 15 nm thick film of $H_2Pc$ on quartz, normalised for better visibility. The molecules were deposited in a UHV chamber and the thickness was measured *ex-situ* by AFM to determine the tooling factor. PL and absorbance of the $MoS_2$ shows the typical A and B excitonic features. The PL of the A exciton is at 1.89 eV and the A and B exciton transitions in absorbance are

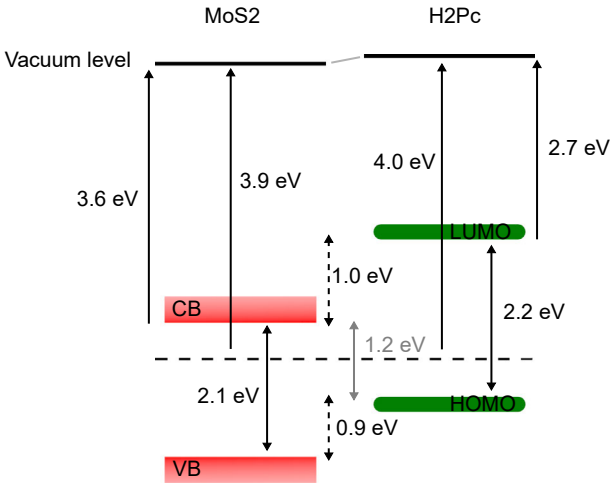


Figure 5.5: Resulting energy level alignment at the interface of $MoS_2$ and $H_2Pc$ (redrawn from [39]).

found at 1.90 eV and 2.05 eV. The absorption of $H_2Pc$ features two main bands as typical for phthalocyanines and the related porphyrins. In the violet to near UV region, the Soret- or B-band can be seen emerging around 3 eV. The Q band is found in the visible region of the light spectrum between 1.7 eV and 2.2 eV with two distinct peaks at 1.78 eV and 1.94 eV. These values agree well with absorption spectra of $H_2Pc$ thin films found in literature of the so-called $\alpha$-phase [297, 298]. $H_2Pc$ exhibits a broad emission between ca. 1.2-1.7 eV peaked at 1.4 eV. An exciton binding energy of the $MoS_2$ A exciton on $SiO_2$ of 200 meV and 420 meV for $H_2Pc$ is calculated from the absorption spectra and the PES measurements. These values are still smaller than the energy of the band offsets, making the dissociation of excitons and subsequent charge transfer energetically possible. PL and absorbance spectra of the hybrid sample of a nominally 1 nm thin film on $MoS_2$ are shown in figure 5.6(b). In PL, both the emission from $MoS_2$ and $H_2Pc$ can be observed at 1.89 eV and 1.42 eV, respectively. For $MoS_2$, a broadening but no shift in the emission spectrum is seen, while $H_2Pc$ shows a slight red-shift of 30 meV. Whereas the PL spectra only show minor changes, the hybrid sample shows a qualitatively different absorption spectrum than the individual ones. In particular, the spectral region below 1.85 eV is modified where only the $H_2Pc$ molecules absorb light. Figure 5.7(a) shows this region in more detail. The hybrid absorption is depicted in blue and the $MoS_2$ monolayer absorption, before deposition of $H_2Pc$ molecules, in red. The green line represents the difference between these two spectra and the broken line is the $H_2Pc$ reference for comparison. As can be seen, the absorption in the hybrid sample is extended further into the red than both the references. An additional feature appears around 1.72 eV. These results

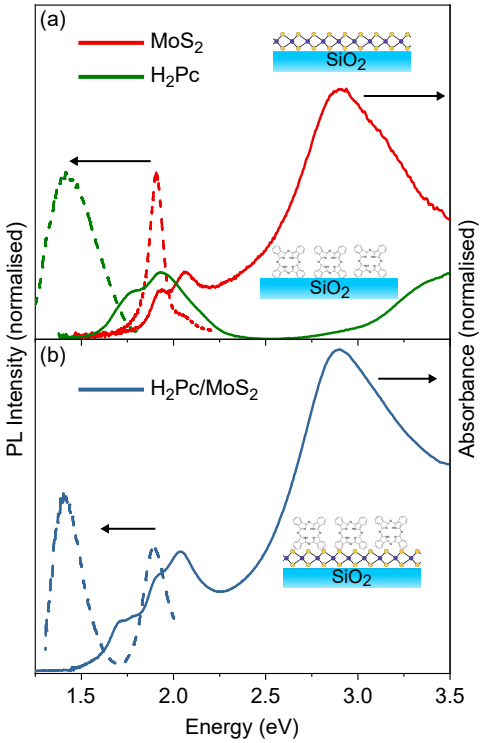


Figure 5.6: (a) Normalised PL and absorbance of an $MoS_2$ monolayer (red) and a 15 nm thick $H_2Pc$ (green) film on $SiO_2$ (b) PL and absorbance of the same $MoS_2$ monolayer as in (a) with 1 nm $H_2Pc$ deposited on top. The PL is only slightly changed. The absorbance shows the additional contribution of $H_2Pc$ as seen in the spectral region around 1.75 eV where only $H_2Pc$ absorbs. Adapted from [39].

are very similar to what Amsterdam *et al.* [20] found for the absorption of different non-metal and metal phthalocyanines on $MoS_2$. It was proposed by the authors to correspond to a direct charge transfer exciton absorption between the $H_2Pc$ HOMO and the $MoS_2$ CB. The absorption energy should therefore correspond approximately to the energy difference between HOMO and CB. This value is 1.2 eV as measured by PES. The energetic difference is much lower in energy than the additional absorption feature around 1.7 eV. Rather, the value of 1.2 eV corresponds well to the observation of an additional excited state at the $MoS_2$/ZnPc interface which was assigned to a relaxed CT state [18]. Also, for charge transfer states in other systems, it is known that they usually exhibit much lower oscillator strength due to their spatially indirect nature compared to the direct transitions [6]. In the present system the absorption at 1.7 eV is however comparable to the $H_2Pc$ reference one. Under these considerations and the PES measurements, the additional absorption feature is not attributed to a CT state. $H_2Pc$ molecules can arrange in various phases in the solid state. The most frequently observed ones

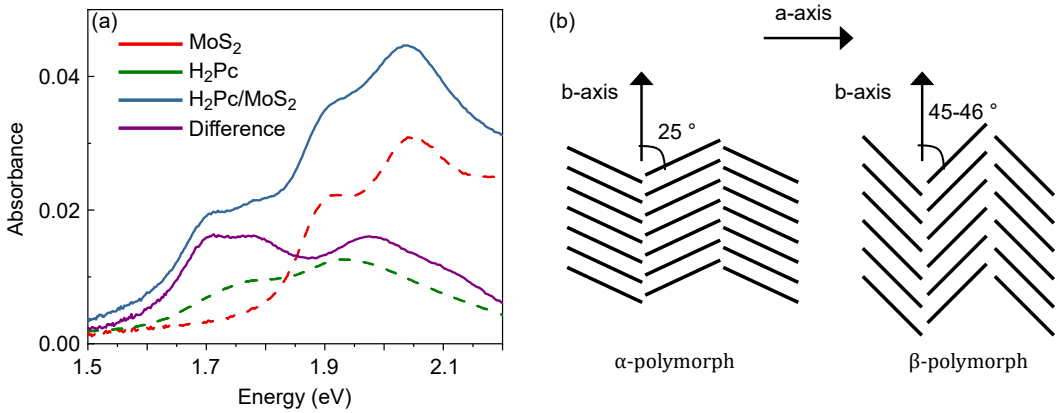


Figure 5.7: (a) Close up of the absorbance shown in 5.6(b). The reference absorbance spectra of $MoS_2$ and 1 nm $H_2Pc$ on $SiO_2$ are shown as dashed lines. The difference spectrum between the hybrid sample (blue) and the $MoS_2$ refernce (red) is displayed in violet. (b) Difference in stacking of $H_2Pc$ in the $\alpha$- and $\beta$-polymorph.

are the $\alpha$- and $\beta$-phase [299]. Both polymorphs differ in the stacking angle with respect to the growth axis. Figure 5.7(b) shows the arrangement of the molecules in the $\alpha$- and $\beta$-phase. The $\alpha$-phase is usually obtained for a growth at room temperature and can be transformed to the $\beta$-phase, for example, by subsequent annealing. The $\beta$-polymorph can be distinguished by a red-shifted absorption as compared to the $\alpha$ one. Also, a larger intensity ratio of the lower to higher energy peak of the Q-band can be observed [300, 301]. Taking the different polymorphs of $H_2Pc$ thin films into account, the stacking of the $H_2Pc$ molecules might be different on $MoS_2$ and the $SiO_2$ substrate used as a reference. The $H_2Pc$ $\beta$-phase exhibits a red-shifted absorption, similar to what was observed here. It was reported that $H_2Pc$ grows flat lying on the van der Waals substrate hBN in the first monolayer, but tends to develop needle-like structures for larger molecular coverage [302]. This elongated growth mode is preferably found for the $H_2Pc$ $\beta$-polymorph [298]. Zhang *et al.* [184] reported on the change in morphology of CuPc grown on $MoS_2$ after air-exposure. They concluded that the CuPc molecules first grow in a face-on orientation and then adopt a more upright orientation when exposed to air. The additional absorption feature cannot unambiguously be correlated to the $\beta$-polymorph from the presented experimental results. AFM images also do not show needle-like aggregates (figure 5.11). Nonetheless, a mixture between different phases seems likely but a more thorough growth study is needed here.

Energy and charge transfer processes between the two materials will lead to a change in the dynamics of the excited state. Therefore, as a next step, time-resolved PL measurements were performed (figure 5.8). Charge or energy transfer from one material to the other after excitation

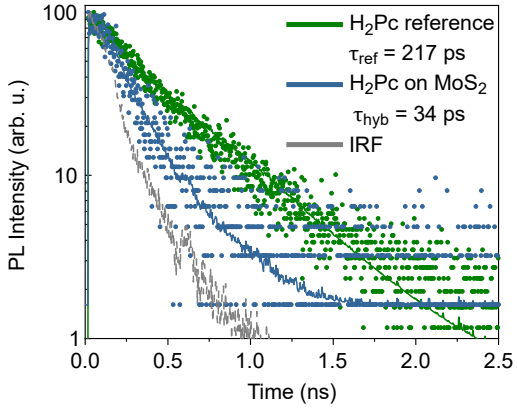


Figure 5.8: PL decay of a 1 nm thin $H_2Pc$ film on $SiO_2$ (green) and on $MoS_2$ (blue). Fitted averaged decay times are given. The IRF is shown in grey (adapted from [39]).

will lead to a shortening of the PL decay time. Considering the overlap of the $MoS_2$ PL and the $H_2Pc$ absorption together with the energy level alignment, both non-radiative resonance energy transfer as well as hole transfer from $MoS_2$ to $H_2Pc$ can occur. Since the PL decay of $MoS_2$ is too fast to be distinguished from the instrument response function already in the reference, only the dynamics of $H_2Pc$ can be probed. The $H_2Pc$ PL does not show any overlap with the $MoS_2$ absorption but excited electron transfer from the LUMO to the CB is energetically feasible. Hence, time-correlated single photon counting of a 1 nm thin $H_2Pc$ film on $SiO_2$ and on $MoS_2$ was measured. A shortening of the $H_2Pc$ PL decay time is observed when it is deposited on $MoS_2$ compared to the film on $SiO_2$. This is an indication for the dissociation of the $H_2Pc$ excitons. The transients were modelled by a two-component exponential function. An average lifetime for $H_2Pc$ on $SiO_2$ of $\tau_{\mathrm{ref}} = 217$ ps is found which reduces to $\tau_{\mathrm{hyb}} \leq 34$ ps in the hybrid sample. This results in an effective exciton dissociation time of $\tau_{\mathrm{dis}} = \frac{\tau_{\mathrm{ref}}\tau_{\mathrm{hyb}}}{\tau_{\mathrm{ref}}-\tau_{\mathrm{hyb}}} = 40$ ps and an efficiency of $\eta = 1 - \frac{\tau_{\mathrm{hyb}}}{\tau_{\mathrm{ref}}} = 0.85$. Here, the decay time of $H_2Pc$ in the hybrid sample is given as an upper limit since a faster component cannot be resolved as the decay is close to the instrument response function (IRF). Fast exciton dissociation and electron transfer on the order of 100 fs have been found at the ZnPc/$MoS_2$ and CuPc/$MoS_2$ interface [18, 19]. The effective dissociation time found here includes also exciton diffusion from molecules further away from the interface.

So far, a quenching of the $H_2Pc$ excitons is observed and associated to the transfer of the excited electron in the molecule's LUMO to the $MoS_2$ CB. This electron can form a charge transfer state with a hole in the HOMO of $H_2Pc$. The CT state can recombine radiatively or non-radiatively at the hybrid interface or dissociate and result in a separated electron and hole. If efficient dissociation occurs, the separated charges can contribute to photoconductivity

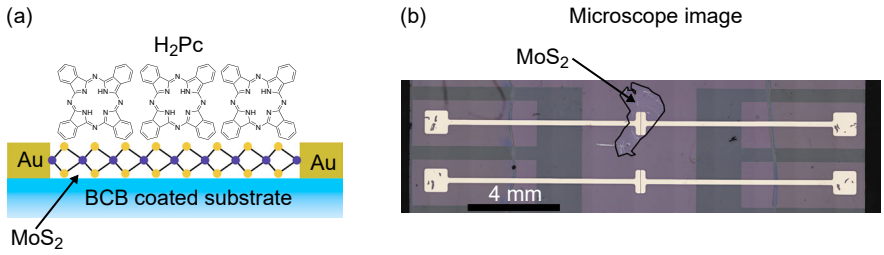


Figure 5.9: (a) Schematic of the hybrid $MoS_2/H_2Pc$ photodetector (modified from [39]) (b) Microscope image of an $MoS_2$ device without $H_2Pc$. Here, two fingers are shown, one which is covered (top, black outline) with $MoS_2$ and one empty one (lower).

or -current which is desired in a sensor or photovoltaic device. Therefore, in order to test if the transferred charges can be used in that way, photocurrent action spectroscopy (PAS) was performed. In this technique, the excitation light is modulated by a mechanical chopper at a certain frequency and the photocurrent is amplified with a lock-in amplifier. In such a way, only the current related to the modulation frequency of the illumination is measured. This results, on the one hand, in an improved signal-to-noise ratio and, on the other hand, suppresses the persistent photoconductivity present in $MoS_2$ devices. The $MoS_2$-based detectors used in this study were fabricated from commercially purchased CVD-grown monolayer $MoS_2$. As a dielectric substrate, a layer of a benzocyclobutene (BCB)-based polymer was deposited by spin coating from toluene solution onto an $SiO_2$ substrate. BCB is used as a raisin in microelectronics. Here it was taken to minimise electronically active traps in $SiO_2$ which could influence the $MoS_2$ photoconductivity [172, 229]. After the deposition of the BCB layer, the gold electrodes were deposited in a vacuum chamber through a shadow mask. The resulting channel length and width were 30 µm and 1 mm, respectively. The monolayer was positioned *via* a polystyrene-based wet transfer process on prefabricated electrodes [26]. The schematic detector design is shown in figure 5.9 with a microscope image of a resulting device. For the hybrid device, a nominally 3 nm thin film of $H_2Pc$ was thermally evaporated in vacuum onto the whole device with the positioned $MoS_2$ monolayer. A source-drain bias of 10 V was applied to register the photocurrent. The response of the photodetector was derived by dividing the current by the power of the excitation light at each wavelength. Figure 5.10 displays the normalised photoresponse of an $MoS_2$-only reference detector and a hybrid $H_2Pc/MoS_2$ one. Normalisation was done at the energy range where $H_2Pc$ does not absorb ($\approx$ 2.5 eV) to compare only the additional photoconductivity induced by the $H_2Pc$ layer. A clear increase, but also an extension of the spectral response of the hybrid photodetector to lower energy values, can be seen when compared to the $MoS_2$ reference. As apparent from the red curve in the figure, the photoresponse of the $MoS_2$ reference directly mimics the absorption spectrum with

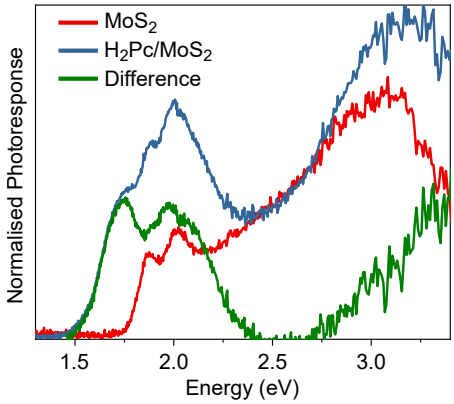


Figure 5.10: Normalised photoresponse of an $MoS_2$ reference photoconductor (green) and a hybrid device (blue). The difference of these two spectra is shown in green which clearly resembles the $H_2Pc$ absorption (adapted from [39]).

the typical A, B and broad C excitonic features. The hybrid sample shown in blue demonstrates additional peaks. They stem from $H_2Pc$ as becomes clear when subtracting the $MoS_2$ reference from the hybrid response, as displayed in green. Both the Q-band from around 1.6 to 2.3 eV and the Soret band at higher energies than ca. 3 eV can be identified. This is a clear indication that the $H_2Pc$ molecules indeed contribute to the photoconductivity. In order to exclude that this contribution is solely due to a photoconducting effect in the $H_2Pc$ layer on top of $MoS_2$ without charge transfer, a photodetector with only $H_2Pc$ was prepared. No photocurrent could be detected in this device. In addition, to exclude that this is caused by a difference in the morphology of the $H_2Pc$ layer grown on the $MoS_2$ and on BCB, AFM images were acquired. On the left side of figure 5.11 one can see the morphology of $H_2Pc$ on $MoS_2$ and on BCB on the right side. In both cases, spherical-like particles were observed, similar to the results of other groups [184, 298, 303]. It can also be seen that neither on $MoS_2$ nor on BCB a closed layer is formed. This can explain why no photocurrent was seen for the $H_2Pc$-only device even though it can, in principle, conduct current. In the presented case, the discontinuous morphology is beneficial since now the total contribution of $H_2Pc$ seen in PAS can be traced back to an excited state charge transfer. An estimation of the efficiency of the additional photoconductivity through charge transfer can be obtained by looking at the PA spectra (figure 5.10). The contribution of $H_2Pc$ in the region of the Q-band to the photoresponse is comparable to the one measured for the $MoS_2$ reference around the A-exciton. Both materials also absorb approximately the same amount of light in this region (figure 5.6). This indicates that the transferred electrons contribute to the photoconductivity with roughly the same efficiency as the electrons generated by a direct absorption process in $MoS_2$. Here it is

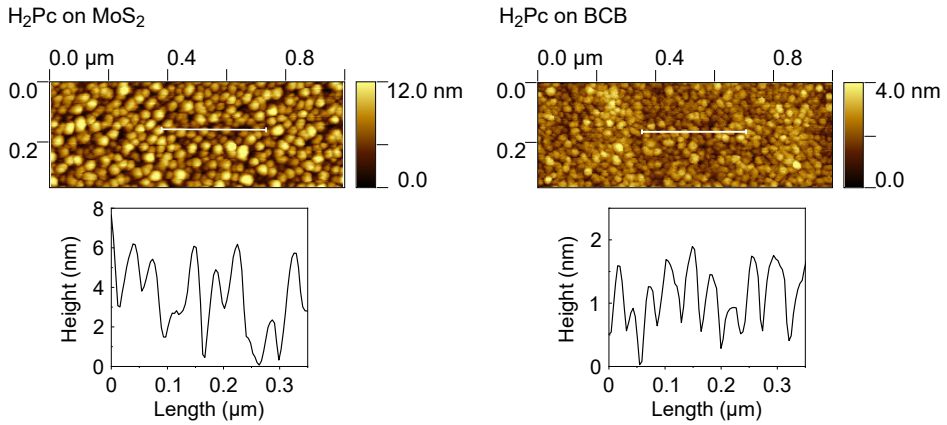


Figure 5.11: AFM of $H_2Pc$ on $MoS_2$ and on BCB. The nominal thickness in both cases was 3 nm. The height is taken at the white line (modified from [39]).

assumed that the electron mobility in the reference and hybrid sample is the same. Therefore, the electrons transferred from $H_2Pc$ to $MoS_2$ can be used in an advantageous way since they indeed contribute to the $MoS_2$ photoconductivity.

## 5.3 Summary and outlook

To summarise, PES and inverse PES revealed a robust type II energy level alignment between an $MoS_2$ monolayer and a thin film of the organic molecule $H_2Pc$. The energy offset between HOMO and VB as well as LUMO and CB was found to be $\sim 1$ eV. No evidence of ground state charge transfer was found. Excited state charge transfer is however energetically favourable, demonstrated by the efficient quenching of $H_2Pc$ excitons. Further, with the help of PAS, it was shown that the transferred electron from the molecule's LUMO into the $MoS_2$ CB is not lost at the interface. On the contrary, it contributes to the photoconductivity of the underlying $MoS_2$. Due to the smaller optical energy gap of $H_2Pc$, the overall response of the hybrid detector is extended towards lower energy. Also, an overall increase in relative photoconductivity is manifested by the charge transfer. Further studies on this system can involve the growth and exact stacking of ultrathin $H_2Pc$ films and their influence on the optical response. Future work will be devoted to the detection of the CT state, which should occur at around 1.2 eV according to PES. This can be pursued by using NIR PL or electroluminescence measurements [293].

Another interesting hybrid system, i.e. $MoS_2$ and the molecule 2,7-Bis[9,9-di(4-methylphenyl)-fluoren-2-yl]-9,9-di(4-methylphenyl)fluorene (TDAF), was looked at and preliminary results are shown in figure 5.12. TDAF shows strong PL quenching in the hybrid as seen in time-resolved measurements. The molecule absorbs in the near UV and its PL is overlapping with the $MoS_2$

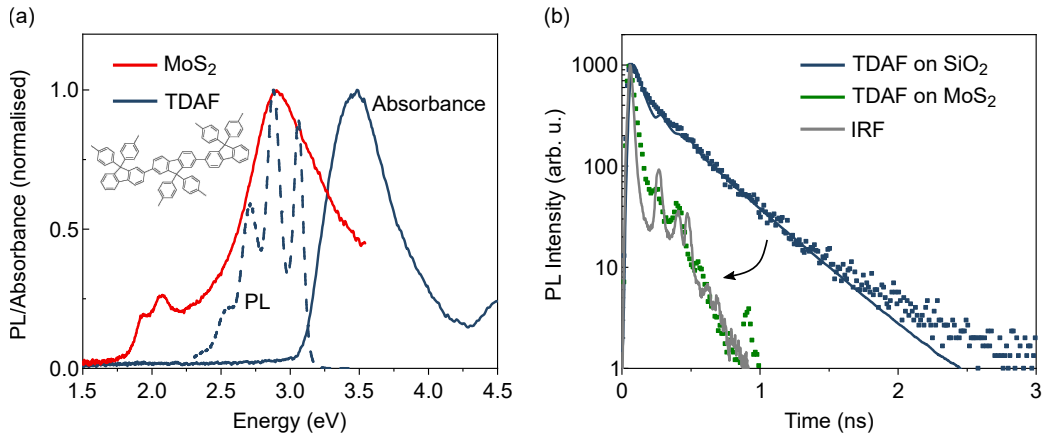


Figure 5.12: (a) Normalised PL and absorbance of the molecules TDAF (blue) deposited on $SiO_2$ and the absorbance of an $MoS_2$ monolayer (red). A large overlap between the TDAF PL and the c-exciton absorption of $MoS_2$ is seen. The molecular structure is shown as well. (b) PL decay of TDAF on $SiO_2$ and on $MoS_2$. On $SiO_2$, the decay time is 226 ps whereas on $MoS_2$ the PL decay is indistinguishable from the IRF (grey).

absorption so that efficient energy transfer might be possible. Future work can use this as a starting point for studying this system in more depth, similar to the $MoS_2/H_2Pc$-system. The absorption of TDAF is interesting for sensor applications where an increased sensitivity in the UV spectral region is desired.

The monolayer nature of TMDCs and their chemical inertness make them particularly interesting to study interface phenomena. This is reflected in the study of hybrid TMDC/organic systems by several research groups. It was shown in literature that TMDCs can serve as ideal templates for the growth of organic molecules since defect-free TMDCs do not possess dangling bonds. Situations where only weak van der Waals interaction between the molecules and the underlying substrate exist is expected to occur therefore more often. Still, fast excited charge transfer has been observed in this study as well as in the works of other groups, as described in the beginning of this chapter. These transfer processes can, thus, compete with the ultrafast excited state dynamics present in TMDCs. As these studies are promising also with respect to sensor applications or in FET, there still needs to be a more thorough understanding of underlying processes at the interface. This starts, for one, with a better knowledge of the energy level alignment since the electronic states in TMDC monolayers are also affected by the dielectric surrounding [229]. Additionally, the possibly reduced interaction of the molecules with TMDCs as a growth substrate can, for example, lead to different molecular growth [252, 304]. This might lead to altered optical properties complicating comparative studies where a

reference is needed. The presented study, together with already existing literature, highlight that TMDCs in combination with organic molecules and polymers are promising for further investigation. It is seen that fast processes like charge and energy transfer occur at the hybrid TMDC/organic interface which can be utilised in flexible and semi-transparent opto-electronic applications.

# 6 Conclusion and outlook

The target of the conducted studies for this thesis was to deepen the understanding of energy and charge transfer phenomena at hybrid inorganic/organic interfaces. The goal of utilising these processes in possible later opto-electronic devices was always kept in mind in the design of the experiments. Two routes for two different material combinations were explored. These were, on the one side, non-radiative energy transfer and, on the other side, excited state charge transfer.

Non-radiative FRET was investigated in chapter one from the already technologically relevant GaN-class of materials to the solution-processable polymer Cn-ether PPV. In addition to the studies in literature [9, 13, 47, 305], it was concluded from photoluminescence studies that FRET not only led to an exciton transfer but that these excitons could indeed enhance the emission of the acceptor. This was also found true for InGaN/GaN quantum well systems possessing large internal electric fields that reduce the FRET rate. These two points are relevant from an application point of view since FRET needs to compete with the already high overall power conversion efficiency of white LEDs which rely on radiative colour conversion ($\sim$40 - 50 %). Moreover, the FRET scheme also works efficiently for cyan to green light emitting diodes with higher indium content and therefore higher internal electric fields. It was, however, also shown by temperature dependent PL measurements that the competition between the different decay channels of the excited states need to be taken into account. In the studied system, it was found that non-radiative pathways in the InGaN/GaN quantum well outcompeted both radiative and FRET rates at temperatures around 130 K. These non-radiative decay channels are defect assisted, which stem from crystal imperfections, and are in principle not inherent to high efficiency LEDs. The challenge of implementing the FRET scheme in working LEDs is to bring donor and acceptor materials in close proximity of a few nanometres. Although some routes, like structuring the LEDs into pillars, are being pursued [48, 306–308], there is still work to be done. It is hoped that this study can shed some light on the advantages of FRET to boost colour conversion and help future work that follows this scheme.

The emerging material of TMDCs was considered as the inorganic counterpart in the second hybrid system. TMDCs are promising candidates for ultra-thin optoelectronic applications. TMDCs became popular only recently in the last 10-15 years. Hence, no large scale fabrication

method exists so far to produce high quality crystals as opposed to GaN, for example. The quality of TMDCs, especially grown by chemical vapour deposition methods, has improved in the last years. However, an all-UHV process can bring the advantage of better growth control which is needed to study intrinsic effects of TMDCs. Furthermore, it becomes possible to grow heterostructures as well as alloys in one process without breaking the vacuum. This is particularly important for the fabrication of reliable devices with invariable quality. Therefore, the easily implementable PTD method was developed in-house. Optical spectroscopy, like absorbance and PL, were used as feedback. It was shown that through the resistive heating process of a metal wire, TMDC monolayers with comparable optical properties to the monolayers obtained by the more conventional CVD or mechanical exfoliation methods, could be grown. To further demonstrate the flexibility of the PTD process, mixed $Mo_{1-x}W_xS_2$ alloys and thin heterostructures of $TaS_2/MoS_2$ were grown. This new method still needs more optimisation. The grain size of the monolayers is in the order of a few ten nanometres, as compared to micrometres for the other processes, and needs to be enlarged. Also, so far nothing is known about the defect density of the samples, which is necessary when introducing dopants. Among other measurements, this will require extended electron microscope studies. However, thanks to the promising results presented, this method will be examined and optimised further, thereby leading to a better understanding of the intrinsic properties of the TMDCs.

One extrinsic effect that influences the optical and electronic properties of monolayer TMDCs is their dielectric surrounding. By combining PES and DRS, it was shown that the exciton binding energy and the electron band gap shrink for $MoS_2$ and $WSe_2$ when deposited on gold as compared to sapphire. The exciton transition energy was further measured for three other dielectric substrates. Only a slight red-shift in the transition energy was found. This can be explained by an almost compensating reduction of the exciton binding energy and the electron band gap as discussed in literature [14]. However, the value of the substrate dielectric function, especially when considering its energy dependence, is still under debate [120]. The PES and DRS studies presented here serve as a step towards a more thorough understanding of the influence of the dielectric surrounding when combined with theory in the future. This understanding opens up the possibility of band gap engineering of TMDCs solely through their dielectric surrounding. For example, by varying the in-plane band gap energy through systematically tailoring the dielectric substrate.

Organic molecules in a hybrid system represent another extrinsic effect influencing TMDC properties. The charge transfer route was followed in this case, as compared to FRET in the InGaN/Cn-ether PPV system. For this, $MoS_2/H_2Pc$ heterostructures were investigated by PL, PES and PAS. A type II energy level was found to promote excited state electron transfer from $H_2Pc$ to $MoS_2$. Charge transfer was manifested by a shortening of the decay

time. A transfer efficiency of 85 % was found in agreement with fast charge transfer reported in literature [18, 19]. The experimentally determined energy level alignment in the presented case made it more over possible to determine the CB-HOMO energy offset to be 1.2 eV. This value is much lower than what was assigned to be stemming from a CT exciton measured in absorption [20]. Hence, the additional absorption feature, also seen in the presented case, is not attributed to a CT exciton. It seems likely to be caused by a different stacking of the molecules on $H_2Pc$ than on quartz. PAS further allowed to establish that transferred electrons are not lost at the interface but can contribute to an enhanced photoconductivity. The absorption of $H_2Pc$ spectrally extended the sensitivity of the hybrid photoconductor further in relation to the $MoS_2$-only device. The presented study helps to understand the processes at the hybrid TMDC/$H_2Pc$ interface in particular, but also illustrates the use of hybrid TMDC/molecule structures in a more general way.

The studies shown in this thesis exemplify how the combination of inorganic semiconductors with organic molecules can improve the functionality of either material type. This can result in an improved light emission or an enhanced spectral sensitivity in optical sensors, as demonstrated. Further steps towards an implementation for commercial devices are to better understand the role of defects in the inorganic counterpart and to better control molecular growth and orientation at the hybrid interface. Here, two-dimensional TMDCs have been proven to be auspicious candidates for further studies. The monolayer growth of these materials keeps improving, which provides high quality templates for van-der Waals epitaxy with organic molecules. Molecular orientation and stacking can differ from the growth on other substrates, like quartz, due to a weak interaction. In order to study the processes at the hybrid interface, a profound understanding of the influence of the underlying substrate is also needed. This could be achieved, for example, by decoupling the TMDC from the substrate through few layers of the insulating and pristine material h-BN. Another possibility would be to transfer the TMDCs on prefabricated molecular layers. The molecular layer can then also be used for shaping the energetic landscape of the TMDCs. This can either be done by introducing alternating donor and acceptor molecules to induce doping or by varying the dielectric surrounding in order to change the TMDC band gap energy.

# Bibliography


1. Kroemer, H. Nobel Lecture: Quasielectric fields and band offsets: teaching electrons new tricks. *Reviews of Modern Physics* **73,** 783–793 (2001).
2. Sze, S. M. *et al. Physics of Semiconductor Devices* 3. ed. ISBN: 0-471-14323-5 (Wiley-Interscience, Hoboken, NJ, 2007).
3. Agranovich, V. M. *et al.* Hybrid resonant organic-inorganic nanostructures for optoelectronic applications. *Chemical Reviews* **111,** 5179–5214 (2011).
4. Blumstengel, S. *et al.* Converting Wannier into Frenkel excitons in an inorganic/organic hybrid semiconductor nanostructure. *Physical Review Letters* **97,** 237401 (2006).
5. Bianchi, F. *et al.* Cascade energy transfer versus charge separation in ladder-type oligo(p -phenylene)/ZnO hybrid structures for light-emitting applications. *Applied Physics Letters* **105,** 233301 (2014).
6. Piersimoni, F. *et al.* Charge transfer absorption and emission at ZnO/Organic interfaces. *The Journal of Physical Chemistry Letters* **6,** 500–504 (2015).
7. Eyer, M. *et al.* Charge transfer excitons at ZnMgO/P3HT heterojunctions: Relation to photovoltaic performance. *Applied Physics Letters* **107,** 221602 (2015).
8. Chanyawadee, S. *et al.* Nonradiative exciton energy transfer in hybrid organic-inorganic heterostructures. *Physical Review B* **77,** 193402 (2008).
9. Itskos, G. *et al.* Efficient dipole-dipole coupling of Mott-Wannier and Frenkel excitons in (Ga,In)N quantum well/polyfluorene semiconductor heterostructures. *Physical Review B* **76,** 035344 (2007).
10. Rindermann, J. J. *et al.* Dependence of resonance energy transfer on exciton dimensionality. *Physical Review Letters* **107,** 236805 (2011).
11. Yu, P. *et al.* 13% efficiency hybrid organic/silicon-nanowire heterojunction solar cell via interface engineering. *ACS Nano* **7,** 10780–10787 (2013).
12. Huang, Y. L. *et al.* The organic-2D transition metal dichalcogenide heterointerface. *Chemical Society Reviews* **47,** 3241–3264 (2018).

13. Itskos, G. *et al.* Förster resonant energy transfer from an inorganic quantum well to a molecular material: Unexplored aspects, losses, and implications to applications. *The Journal of Chemical Physics* **143,** 214701 (2015).

14. Cho, Y. *et al.* Environmentally sensitive theory of electronic and optical transitions in atomically thin semiconductors. *Physical Review B* **97,** 041409(R) (2018).

15. Chernikov, A. *et al.* Exciton binding energy and nonhydrogenic Rydberg series in monolayer $WS_2$. *Physical Review Letters* **113,** 076802 (2014).

16. Waldecker, L. *et al.* Rigid band shifts in two-dimensional semiconductors through external dielectric screening. *Physical Review Letters* **123,** 206403 (2019).

17. Vélez, S. *et al.* Gate-tunable diode and photovoltaic effect in an organic-2D layered material p-n junction. *Nanoscale* **7,** 15442–15449 (2015).

18. Kafle, T. R. *et al.* Effect of the interfacial energy landscape on photoinduced charge generation at the ZnPc/$MoS_2$ interface. *Journal of the American Chemical Society* **141,** 11328–11336 (2019).

19. Padgaonkar, S. *et al.* Molecular-orientation-dependent interfacial charge transfer in phthalocyanine /$MoS_2$ mixed-dimensional heterojunctions. *The Journal of Physical Chemistry C* **123,** 13337–13343 (2019).

20. Amsterdam, S. H. *et al.* Electronic coupling in metallophthalocyanine-transition metal dichalcogenide mixed-dimensional heterojunctions. *ACS Nano* **13,** 4183–4190 (2019).

21. Kasap, S. *et al. Springer Handbook of Electronic and Photonic Materials* 1537 pp. ISBN: 978-3-319-48931-5 (Springer International Publishing, Cham, 2017).

22. Haugstad, G. *Atomic Force Microscopy. Understanding Basic Modes and Advanced Applications* xxii, 464. ISBN: 9780470638828 (John Wiley & Sons, Hoboken N.J., 2012).

23. Bruker Corporation. *Peak Force Tapping* (ed Bruker Nano Surfaces Devision) `https://www.bruker.com/fileadmin/user_upload/8-PDF-Docs/SurfaceAnalysis/AFM/Brochures/PeakForce_Tapping_-_Brochure.pdf` (2020).

24. Frisenda, R. *et al.* Recent progress in the assembly of nanodevices and van der Waals heterostructures by deterministic placement of 2D materials. *Chemical Society Reviews* **47,** 53–68 (2018).

25. Kang, K. *et al.* Layer-by-layer assembly of two-dimensional materials into wafer-scale heterostructures. *Nature* **550,** 229–233 (2017).

26. Gurarslan, A. *et al.* Surface-energy-assisted perfect transfer of centimeter-scale monolayer and few-layer $MoS_2$ films onto arbitrary substrates. *ACS Nano* **8,** 11522–11528 (2014).

27. Pelant, I. *et al. Luminescence Spectroscopy of Semiconductors* ISBN: 0199588333 (Oxford University Press, Oxford and New York, 2012).

28. Lakowicz, J. R. *Principles of Fluorescence Spectroscopy* 3rd ed. ISBN: 0387312781 (Springer, New York, 2006).

29. Meisel, T. *et al.* Fingerprint of charge redistribution in the optical spectra of hybrid inorganic/organic semiconductor interfaces. *The Journal of Physical Chemistry C* **122,** 12913–12919 (2018).

30. Frisenda, R. *et al.* Micro-reflectance and transmittance spectroscopy: a versatile and powerful tool to characterize 2D materials. *Journal of Physics D: Applied Physics* **50,** 074002 (2017).

31. McIntyre, J. *et al.* Differential reflection spectroscopy of very thin surface films. *Surface Science* **24,** 417–434 (1971).

32. Zinth, W. *et al. Optik. Lichtstrahlen - Wellen - Photonen* 3., verb. Aufl. 337 pp. ISBN: 9783486705348 (Oldenbourg, München, 2011).

33. Fox, A. M. *Optical Properties of Solids* Second edition. 396 pp. ISBN: 9780191576720 (Oxford University Press, Oxford and New York, 2010).

34. Born, M. *et al. Principles of Optics. Electromagnetic Theory of Propagation, Interference and Diffraction of Light* 6. ed., reprinted (with corrections). 808 pp. ISBN: 0-08-026482-4 (Pergamon Press, Oxford, 1993).

35. Michler, G. H. *Electron Microscopy ofPolymers* ISBN: 978-3-540-36350-7 (Springer, Berlin and Heidelberg, 2008).

36. Suga, S. *et al. Photoelectron Spectroscopy* 389 pp. ISBN: 978-3-642-37529-3 (Springer Berlin Heidelberg, Berlin, Heidelberg, 2014).

37. Dr. Rudy Schlaf. *Calibration of Photoemission Spectra and Work Function Determination* `http://rsl.eng.usf.edu/Documents/Tutorials/PEScalibration.pdf` (2020).

38. Park, S. *et al.* Direct determination of monolayer $MoS_2$ and $WSe_2$ exciton binding energies on insulating and metallic substrates. *2D Materials* **5,** 025003 (2018).

39. Mutz, N. *et al.* Excited-state charge transfer enabling $MoS_2$/phthalocyanine photodetectors with extended spectral sensitivity. *The Journal of Physical Chemistry C* **124,** 2837–2843 (2020).

40. Haken, H. *et al. Molekülphysik und Quantenchemie. Einführung in die experimentellen und theoretischen Grundlagen ; mit 43 Tabellen und 133 Aufgaben* 5., völlig neubearb. und erw. Aufl. 530 pp. ISBN: 9783540303145 (Springer, Berlin, 2006).
41. Mutz, N. *et al.* Energy transfer between cyano-ether PPV and InGaN/GaN quantum wells with large piezoelectric fields. *Physica Status Solidi (a)* **215,** 1800322 (2018).
42. Snider, G. *1D Schrödinger and Poisson solver* `https://www3.nd.edu/~gsnider/`.
43. Kirmse, H. *et al.* Structure of p -Sexiphenyl nanocrystallites in ZnO revealed by high-resolution transmission electron microscopy. *Crystal Growth & Design* **16,** 2789–2794 (2016).
44. Achermann, M. *et al.* Energy-transfer pumping of semiconductor nanocrystals using an epitaxial quantum well. *Nature* **429,** 642–646 (2004).
45. Rohrmoser, S. *et al.* Temperature dependence of exciton transfer in hybrid quantum well/nanocrystal heterostructures. *Applied Physics Letters* **91,** 092126 (2007).
46. Itskos, G. *et al.* White light emission via cascade Förster energy transfer in (Ga, In)N quantum well/polymer blend hybrid structures. *Nanotechnology* **20,** 275207 (2009).
47. Chanyawadee, S. *et al.* Increased color-conversion efficiency in hybrid light-emitting diodes utilizing non-radiative energy transfer. *Advanced Materials* **22,** 602–606 (2010).
48. Smith, R. *et al.* Hybrid III-nitride/organic semiconductor nanostructure with high efficiency nonradiative energy transfer for white light emitters. *Nano Letters* **13,** 3042–3047 (2013).
49. Achermann, M. *et al.* Nanocrystal-based light-emitting diodes utilizing high-efficiency nonradiative energy transfer for color conversion. *Nano Letters* **6,** 1396–1400 (2006).
50. Zhuang, Z. *et al.* Improvement of color conversion and efficiency droop in hybrid light-emitting diodes utilizing an efficient non-radiative resonant energy transfer. *Applied Physics Letters* **109,** 141105 (2016).
51. Quay, R. *Gallium Nitride Electronics* ISBN: 978-3-540-71892-5 (Springer, Berlin, Heidelberg, 2008).
52. Vurgaftman, I. *et al.* Band parameters for nitrogen-containing semiconductors. *Journal of Applied Physics* **94,** 3675–3696 (2003).
53. Nakamura, S. Nobel Lecture: Background story of the invention of efficient blue InGaN light emitting diodes. *Reviews of Modern Physics* **87,** 1139–1151 (2015).
54. Ruterana, P. *et al. Nitride Semiconductors. Handbook on Materials and Devices* 1st ed. ISBN: 3527403876 (Wiley-VCH, Weinheim, 2003).

55. Chichibu, S. *et al.* Spontaneous emission of localized excitons in InGaN single and multiquantum well structures. *Applied Physics Letters* **69,** 4188–4190 (1996).

56. Morel, A. *et al.* Donor-acceptor-like behavior of electron-hole pair recombinations in low-dimensional (Ga,In)N/GaN systems. *Physical Review B* **68,** 045331 (2003).

57. Graham, D. M. *et al.* Optical and microstructural studies of InGaN/GaN single-quantum-well structures. *Journal of Applied Physics* **97,** 103508 (2005).

58. Davies, M. J. Optical Studies of InGaN/GaN Quantum Well Structures. *PhD thesis.* `https://www.research.manchester.ac.uk/portal/en/theses/optical-studies-of-ingangan-quantum-well-structures(f6c6e59b-8366-44aa-b149-9338d3f03dc0).html` (2014).

59. *GaN Wurtzite Crystal Structure* `https://en.wikipedia.org/wiki/Gallium_nitride`.

60. Wood, C. *et al. Polarization Effects in Semiconductors. From Ab InitioTheory to Device Applications* 523 pp. ISBN: 9780387368313 (Springer Science+Business Media LLC, Boston, MA, 2008).

61. Fiorentini, V. *et al.* Evidence for nonlinear macroscopic polarization in III–V nitride alloy heterostructures. *Applied Physics Letters* **80,** 1204–1206 (2002).

62. Tan, I. H. *et al.* A self-consistent solution of Schrödinger-Poisson equations using a nonuniform mesh. *Journal of Applied Physics, 68(8), 4071-4076* (1990).

63. Burroughes, J. H. *et al.* Light-emitting diodes based on conjugated polymers. *Nature* **347,** 539–541 (1990).

64. Helbig, M. *et al.* Investigation of poly(arylenevinylene)s. Electrochemical studies on poly(p-phenylenevinylene)s. *Die Makromolekulare Chemie* **194,** 1607–1618 (1993).

65. Greenham, N. C. *et al.* Efficient light-emitting diodes based on polymers with high electron affinities. *Nature* **365,** 628–630 (1993).

66. Barth, S. *et al.* Extrinsic and intrinsic dc photoconductivity in a conjugated polymer. *Physical Review. B* **56,** 3844–3851 (1997).

67. Rost, H. *et al.* Novel light emitting and photoconducting polyarylenevinylene derivatives containing phenylene arylamine and phenylene oxide units in the main chain. *Synthetic Metals* **84,** 269–270 (1997).

68. Tillmann, H. *et al.* Synthesis, optical and redox properties of novel segmented cyano-PPV derivatives. *Synthetic Metals* **101,** 138–139 (1999).

69. Chasteen, S. V. *et al.* The effect of broken conjugation on the excited state: ether linkage in the cyano-substituted poly(p-phenylene vinylene) conjugated polymer poly(2,5,2',5'-tetrahexyloxy-8,7'-dicyano-di-p-phenylene vinylene). *The Journal of Chemical Physics* **124,** 214704 (2006).

70. Pope, M. *et al. Electronic Processes in Organic Crystals and Polymers* 2. ed. 1328 pp. ISBN: 0-19-512963-6 (Oxford Univ. Press, New York, 1999).

71. Köhler, A. *et al. Electronic Processes in Organic semiconductors. An Introduction* 405 pp. ISBN: 978-3-527-68514-1 (Wiley-VCH Verlag GmbH & Co, Weinheim, 2015).

72. Samuel *et al.* Efficient interchain photoluminescence in a high-electron-affinity conjugated polymer. *Physical Review. B* **52,** 11573–11576 (1995).

73. Samuel, I. *et al.* Intra- and inter-molecular photoexcitations in a cyano-substituted poly(p-phenylenevinylene). *Chemical Physics* **227,** 75–82 (1998).

74. Hsu, J.-H. *et al.* Decay dynamics of interchain excited states in luminescent conjugated polymer CN-PPV. *Chemical Physics* **269,** 367–379 (2001).

75. Conwell *et al.* Interchain photoluminescence in poly(phenylene vinylene) derivatives. *Physical Review. B* **54,** 2308–2310 (1996).

76. Grynberg, G. *et al. Introduction to Quantum Optics. From the Semi-Classical Approach to Quantized Light* 665 pp. ISBN: 978-0-511-78825-3 (Cambridge University Press, Cambridge, 2010).

77. Griffiths, D. J. *Introduction to Electrodynamics* 3. ed., reprinted with corrections. 576 pp. ISBN: 0-13-805326-x (Prentice Hall, Upper Saddle River, NJ, 1999).

78. Förster, T. Zwischenmolekulare Energiewanderung und Fluoreszenz. *Annalen der Physik* **437,** 55–75 (1948).

79. Agranovich, V. *et al.* Hybrid interface excitons in organic-inorganic quantum wells. *Solid State Communications* **92,** 295–301 (1994).

80. Basko, D. *et al.* Förster energy transfer from a semiconductor quantum well to an organic material overlayer. *The European Physical Journal B* **8,** 353–362 (1999).

81. Dexter, D. L. A theory of sensitized luminescence in solids. *The Journal of Chemical Physics* **21,** 836–850 (1953).

82. Berkowicz, E. *et al.* Optical spectroscopy of InGaN/GaN quantum wells. *Physica Status Solidi (b)* **216,** 291–300 (1999).

83. Lefebvre, P. *et al.* High internal electric field in a graded-width InGaN/GaN quantum well: Accurate determination by time-resolved photoluminescence spectroscopy. *Applied Physics Letters* **78,** 1252–1254 (2001).

84. *GaN Literature Values* `http://www.ioffe.ru/SVA/NSM/Semicond/GaN/bandstr.html`.

85. Mayrock, O. *et al.* Polarization charge screening and indium surface segregation in (In,Ga)N/GaN single and multiple quantum wells. *Physical Review B* **62,** 16870–16880 (2000).

86. Monemar, B. *et al.* Influence of polarization fields and depletion fields on photoluminescence of AlGaN/GaN multiple quantum well structures. *Physica Status Solidi (b)* **237,** 353–364 (2003).

87. Tingberg, T. *et al.* Investigation of Si and O donor impurities in unintentionally doped MBE-grown GaN on SiC(0001) substrate. *Journal of Electronic Materials* **46,** 4898–4902 (2017).

88. Schultz, T. *et al.* Tuning the work function of GaN with organic molecular acceptors. *Physical Review B* **93,** 125309 (2016).

89. Reimann, K. *et al.* Exciton binding energies and band gaps in GaN bulk crystals. *Journal of Crystal Growth* **189-190,** 652–655 (1998).

90. Gelžinytė, K. *et al.* High spatial uniformity of photoluminescence spectra in semipolar (20-21) plane InGaN/GaN quantum wells. *Journal of Applied Physics* **117,** 023111 (2015).

91. Davies, M. J. *et al.* High excitation carrier density recombination dynamics of InGaN/GaN quantum well structures: Possible relevance to efficiency droop. *Applied Physics Letters* **102,** 022106 (2013).

92. Yin, C. *et al.* Tuning of the excited-state properties and photovoltaic performance in PPV-based polymer blends. *The Journal of Physical Chemistry C* **112,** 14607–14617 (2008).

93. List, E. *et al.* Excitation energy migration in highly emissive semiconducting polymers. *Chemical Physics Letters* **325,** 132–138 (2000).

94. *White LED Efficiency* `https://www.dial.de/en/blog/article/efficiency-of-ledsthe-highest-luminous-efficacy-of-a-white-led/`.

95. Zhmakin, A. I. Enhancement of light extraction from light emitting diodes. *Physics Reports* **498,** 189–241 (2011).

96. Rashidi, A. *et al.* Thermal and efficiency droop in InGaN/GaN light-emitting diodes: decoupling multiphysics effects using temperature-dependent RF measurements. *Scientific Reports* **9,** 19921 (2019).

97. Specht, J. F. *et al.* Theory of excitation transfer between two-dimensional semiconductor and molecular layers. *Physical Review Applied* **9,** 044025 (2018).

98. Jiang, B. *et al.* The impact of carrier transport confinement on the energy transfer between InGaN/GaN quantum-well nanorods and colloidal nanocrystals. *Advanced Functional Materials* **22,** 3146–3152 (2012).

99. Mutz, N. *et al.* Pulsed thermal deposition of binary and ternary transition metal dichalcogenide monolayers and heterostructures. *Applied Physics Letters* **114,** 162101 (2019).

100. Geim, A. K. Nobel Lecture: Random walk to graphene. *Reviews of Modern Physics* **83,** 851–862 (2011).

101. Geim, A. K. *et al.* Van der Waals heterostructures. *Nature* **499,** 419–425 (2013).

102. Mak, K. F. *et al.* Photonics and optoelectronics of 2D semiconductor transition metal dichalcogenides. *Nature Photonics* **10,** 216–226 (2016).

103. Kolobov, A. V. *et al. Two-Dimensional Transition-Metal Dichalcogenides* 545 pp. ISBN: 978-3-319-31449-5 (Springer International Publishing, Cham, 2016).

104. Roldán, R. *et al.* Electronic properties of single-layer and multilayer transition metal dichalcogenides $MX_2$ (M = Mo, W and X = S, Se). *Annalen der Physik* **526,** 347–357 (2014).

105. Koperski, M. *et al.* Optical properties of atomically thin transition metal dichalcogenides: observations and puzzles. *Nanophotonics* **6,** 1289–1308 (2017).

106. Yoffe, A. D. Layer compounds. *Annual Review of Materials Science* **3,** 147–170 (1973).

107. Joensen, P. *et al.* Single-layer $MoS_2$. *Materials Research Bulletin* **21,** 457–461 (1986).

108. Zhu, Y. *et al.* Graphene and graphene oxide: synthesis, properties, and applications. *Advanced Materials* **22,** 3906–3924 (2010).

109. Lee, C. *et al.* Measurement of the elastic properties and intrinsic strength of monolayer graphene. *Science* **321,** 385–388 (2008).

110. Radisavljevic, B. *et al.* Single-layer $MoS_2$ transistors. *Nature Nanotechnology* **6,** 147–150 (2011).

111. Mak, K. F. *et al.* Atomically thin $MoS_2$: a new direct-gap semiconductor. *Physical Review Letters* **105,** 136805 (2010).

112. Jin, W. *et al.* Direct measurement of the thickness-dependent electronic band structure of $MoS_2$ using angle-resolved photoemission spectroscopy. *Physical Review Letters* **111,** 106801 (2013).

113. Li, T. *et al.* Electronic properties of $MoS_2$ nanoparticles. *The Journal of Physical Chemistry C* **111,** 16192–16196 (2007).

114. Cappelluti, E. *et al.* Tight-binding model and direct-gap/indirect-gap transition in single-layer and multilayer $MoS_2$. *Physical Review B* **88,** 075409 (2013).

115. Yazyev, O. V. *et al.* $MoS_2$ and semiconductors in the flatland. *Materials Today* **18,** 20–30 (2015).

116. Scalise, E. *et al.* Strain-induced semiconductor to metal transition in the two-dimensional honeycomb structure of $MoS_2$. *Nano Research* **5,** 43–48 (2012).

117. Conley, H. J. *et al.* Bandgap engineering of strained monolayer and bilayer $MoS_2$. *Nano Letters* **13,** 3626–3630 (2013).

118. He, K. *et al.* Experimental demonstration of continuous electronic structure tuning via strain in atomically thin $MoS_2$. *Nano Letters* **13,** 2931–2936 (2013).

119. Nayak, A. P. *et al.* Pressure-dependent optical and vibrational properties of monolayer molybdenum disulfide. *Nano Letters* **15,** 346–353 (2015).

120. Wang, G. *et al.* Colloquium: Excitons in atomically thin transition metal dichalcogenides. *Reviews of Modern Physics* **90,** 021001 (2018).

121. Frindt, R. F. *et al.* Physical properties of layer structures: optical properties and photoconductivity of thin crystals of molybdenum disulphide. *Proceedings of the Royal Society of London. Series A. Mathematical and Physical Sciences* **273,** 69–83 (1963).

122. Klingshirn, C. F. *Semiconductor optics* 3rd ed. xxvii, 809. ISBN: 354038345X (Springer, Berlin and New York, 2007).

123. Tongay, S. *et al.* Defects activated photoluminescence in two-dimensional semiconductors: interplay between bound, charged, and free excitons. *Scientific Reports* **3,** 2657 (2013).

124. Jadczak, J. *et al.* Probing of free and localized excitons and trions in atomically thin $WSe_2$, $WS_2$, $MoSe_2$ and $MoS_2$ in photoluminescence and reflectivity experiments. *Nanotechnology* **28,** 395702 (2017).

125. Selig, M. *et al.* Excitonic linewidth and coherence lifetime in monolayer transition metal dichalcogenides. *Nature Communications* **7,** 13279 (2016).

126. Wang, H. *et al.* Radiative lifetimes of excitons and trions in monolayers of the metal dichalcogenide $MoS_2$. *Physical Review B* **93,** 045407 (2016).

127. Palummo, M. *et al.* Exciton radiative lifetimes in two-dimensional transition metal dichalcogenides. *Nano Letters* **15,** 2794–2800 (2015).

128. Moody, G. *et al.* Intrinsic homogeneous linewidth and broadening mechanisms of excitons in monolayer transition metal dichalcogenides. *Nature Communications* **6,** 8315 (2015).

129. Jakubczyk, T. *et al.* Radiatively limited dephasing and exciton dynamics in $MoSe_2$ monolayers revealed with four-wave mixing microscopy. *Nano Letters* **16,** 5333–5339 (2016).

130. Dey, P. *et al.* Optical coherence in atomic-monolayer transition-metal dichalcogenides limited by electron-phonon interactions. *Physical Review Letters* **116,** 127402 (2016).

131. Cadiz, F. *et al.* Excitonic linewidth approaching the homogeneous limit in $MoS_2$-based van der Waals heterostructures. *Physical Review X* **7,** 021026 (2017).

132. Robert, C. *et al.* Exciton radiative lifetime in transition metal dichalcogenide monolayers. *Physical Review B* **93,** 205423 (2016).

133. Amani, M. *et al.* Near-unity photoluminescence quantum yield in $MoS_2$. *Science* **350,** 1065–1068 (2015).

134. Jin, C. *et al.* On optical dipole moment and radiative recombination lifetime of excitons in $WSe_2$. *Advanced Functional Materials* **27,** 1601741 (2017).

135. Plechinger, G. *et al.* Valley dynamics of excitons in monolayer dichalcogenides. *Physica Status Solidi (RRL)* **11,** 1700131 (2017).

136. Zhang, X.-X. *et al.* Experimental evidence for dark excitons in monolayer $WSe_2$. *Physical Review Letters* **115,** 257403 (2015).

137. Malic, E. *et al.* Dark excitons in transition metal dichalcogenides. *Physical Review Materials* **2,** 014002 (2018).

138. Selig, M. *et al.* Dark and bright exciton formation, thermalization, and photoluminescence in monolayer transition metal dichalcogenides. *2D Materials* **5,** 035017 (2018).

139. Brem, S. *et al.* Exciton relaxation cascade in two-dimensional transition metal dichalcogenides. *Scientific Reports* **8,** 8238 (2018).

140. Cha, S. *et al.* 1s-intraexcitonic dynamics in monolayer $MoS_2$ probed by ultrafast mid-infrared spectroscopy. *Nature Communications* **7,** 10768 (2016).

141. Steinleitner, P. *et al.* Direct observation of ultrafast exciton formation in a monolayer of $WSe_2$. *Nano Letters* **17,** 1455–1460 (2017).

142. Newaz, A. *et al.* Electrical control of optical properties of monolayer $MoS_2$. *Solid State Communications* **155,** 49–52 (2013).

143. Mak, K. F. *et al.* Tightly bound trions in monolayer $MoS_2$. *Nature Materials* **12,** 207–211 (2013).

144. Mouri, S. *et al.* Tunable photoluminescence of monolayer $MoS_2$ via chemical doping. *Nano Letters* **13,** 5944–5948 (2013).

145. Hu, Z. *et al.* Two-dimensional transition metal dichalcogenides: interface and defect engineering. *Chemical Society Reviews* **47,** 3100–3128 (2018).

146. Tongay, S. *et al.* Broad-range modulation of light emission in two-dimensional semiconductors by molecular physisorption gating. *Nano Letters* **13,** 2831–2836 (2013).

147. Qiu, H. *et al.* Hopping transport through defect-induced localized states in molybdenum disulphide. *Nature Communications* **4,** 2642 (2013).

148. Schwermann, C. *et al.* Incorporation of oxygen atoms as a mechanism for photoluminescence enhancement of chemically treated $MoS_2$. *Physical Chemistry Chemical Physics* **20,** 16918–16923 (2018).

149. Zhou, W. *et al.* Intrinsic structural defects in monolayer molybdenum disulfide. *Nano Letters* **13,** 2615–2622 (2013).

150. Suh, J. *et al.* Doping against the native propensity of $MoS_2$: degenerate hole doping by cation substitution. *Nano Letters* **14,** 6976–6982 (2014).

151. Noh, J.-Y. *et al.* Stability and electronic structures of native defects in single-layer $MoS_2$. *Physical Review B* **89,** 205417 (2014).

152. Komsa, H.-P. *et al.* Native defects in bulk and monolayer $MoS_2$ from first principles. *Physical Review B* **91,** 125304 (2015).

153. McDonnell, S. *et al.* Defect-dominated doping and contact resistance in $MoS_2$. *ACS Nano* **8,** 2880–2888 (2014).

154. Chuang, S. *et al.* $MoS_2$ P-type transistors and diodes enabled by high work function $MoO_x$ contacts. *Nano Letters* **14,** 1337–1342 (2014).

155. Park, S. *et al.* Demonstration of the key substrate-dependent charge transfer mechanisms between monolayer $MoS_2$ and molecular dopants. *Communications Physics* **2,** 109 (2019).

156. Singh, A. *et al.* Origin of n -type conductivity of monolayer $MoS_2$. *Physical Review B* **99,** 121201 (2019).

157. Dolui, K. *et al.* Origin of the n-type and p-type conductivity of $MoS_2$ monolayers on a $SiO_2$ substrate. *Physical Review B* **87,** 165402 (2013).

158. Lu, C.-P. *et al.* Bandgap, mid-gap states, and gating effects in $MoS_2$. *Nano Letters* **14,** 4628–4633 (2014).

159. Chae, W. H. *et al.* Substrate-induced strain and charge doping in CVD-grown monolayer $MoS_2$. *Applied Physics Letters* **111,** 143106 (2017).

160. Hong, J. *et al.* Exploring atomic defects in molybdenum disulphide monolayers. *Nature Communications* **6,** 6293 (2015).

161. Yu, Z. *et al.* Towards intrinsic charge transport in monolayer molybdenum disulfide by defect and interface engineering. *Nature Communications* **5,** 5290 (2014).

162. van der Zande, A. M. *et al.* Grains and grain boundaries in highly crystalline monolayer molybdenum disulphide. *Nature Materials* **12,** 554–561 (2013).

163. Xu, X. *et al.* Microstructure and elastic constants of transition metal dichalcogenide monolayers from friction and shear force microscopy. *Advanced Materials* **30,** 1803748 (2018).

164. Lien, D.-H. *et al.* Electrical suppression of all nonradiative recombination pathways in monolayer semiconductors. *Science* **364,** 468–471 (2019).

165. Amani, M. *et al.* Recombination kinetics and effects of superacid treatment in sulfur- and selenium-based transition metal dichalcogenides. *Nano Letters* **16,** 2786–2791 (2016).

166. Sun, D. *et al.* Observation of rapid exciton-exciton annihilation in monolayer molybdenum disulfide. *Nano Letters* **14,** 5625–5629 (2014).

167. Plechinger, G. *et al.* Identification of excitons, trions and biexcitons in single-layer $WS_2$. *Physica Status Solidi (RRL)* **9,** 457–461 (2015).

168. Yu, Y. *et al.* Fundamental limits of exciton-exciton annihilation for light emission in transition metal dichalcogenide monolayers. *Physical Review B* **93,** 201111 (2016).

169. Chernikov, A. *et al.* Electrical tuning of exciton binding energies in monolayer $WS_2$. *Physical Review Letters* **115,** 126802 (2015).

170. Singh, A. *et al.* Trion formation dynamics in monolayer transition metal dichalcogenides. *Physical Review B* **93,** 041401 (2016).

171. Yu, Z. *et al.* Analyzing the carrier mobility in transition-metal dichalcogenide $MoS_2$ field-effect transistors. *Advanced Functional Materials* **27,** 1604093 (2017).

172. Wu, Y.-C. *et al.* Extrinsic origin of persistent photoconductivity in monolayer $MoS_2$ field effect transistors. *Scientific Reports* **5,** 11472 (2015).

173. Rathi, N. *et al.* Reduction of persistent photoconductivity in a few-layer $MoS_2$ field-effect transistor by graphene oxide functionalization. *RSC Advances* **6,** 23961–23967 (2016).

174. Di Bartolomeo, A. *et al.* Electrical transport and persistent photoconductivity in monolayer $MoS_2$ phototransistors. *Nanotechnology* **28,** 214002 (2017).

175. Bao, W. *et al.* High mobility ambipolar $MoS_2$ field-effect transistors: Substrate and dielectric effects. *Applied Physics Letters* **102,** 042104 (2013).

176. Huo, N. *et al.* High carrier mobility in monolayer CVD-grown $MoS_2$ through phonon suppression. *Nanoscale* **10,** 15071–15077 (2018).

177. Jena, D. *et al.* Enhancement of carrier mobility in semiconductor nanostructures by dielectric engineering. *Physical Review Letters* **98,** 136805 (2007).

178. Dolui, K. *et al.* Possible doping strategies for $MoS_2$ monolayers: An ab initio study. *Physical Review B* **88,** 075420 (2013).

179. Schmidt, H. *et al.* Electronic transport properties of transition metal dichalcogenide field-effect devices: surface and interface effects. *Chemical Society Reviews* **44,** 7715–7736 (2015).

180. Balasubramaniam, B. *et al.* Engineering of transition metal dichalcogenide-based 2D nanomaterials through doping for environmental applications. *Molecular Systems Design & Engineering* **4,** 804–827 (2019).

181. Terrones, H. *et al.* New first order Raman-active modes in few layered transition metal dichalcogenides. *Scientific Reports* **4,** 4215 (2014).

182. Lee, C. *et al.* Anomalous lattice vibrations of single- and few-layer $MoS_2$. *ACS Nano* **4,** 2695–2700 (2010).

183. Chakraborty, B. *et al.* Symmetry-dependent phonon renormalization in monolayer $MoS_2$ transistor. *Physical Review B* **85,** 161403 (2012).

184. Zhang, K. *et al.* Self-induced uniaxial strain in $MoS_2$ monolayers with local van der Waals-stacked interlayer interactions. *ACS Nano* **9,** 2704–2710 (2015).

185. Lin, Y. *et al.* Dielectric screening of excitons and trions in single-layer $MoS_2$. *Nano Letters* **14,** 5569–5576 (2014).

186. Ryou, J. *et al.* Monolayer $MoS_2$ bandgap modulation by dielectric environments and tunable bandgap transistors. *Scientific Reports* **6,** 29184 (2016).

187. Naik, M. H. *et al.* Substrate screening effects on the quasiparticle band gap and defect charge transition levels in $MoS_2$. *Physical Review Materials* **2,** 084002 (2018).

188. Komsa, H.-P. *et al.* Effects of confinement and environment on the electronic structure and exciton binding energy of $MoS_2$ from first principles. *Physical Review B* **86,** 241201 (2012).

189. Kylänpää, I. *et al.* Binding energies of exciton complexes in transition metal dichalcogenides and effect of dielectric environment. *Physical Review B* **92,** 658 (2015).

190. Moss, T. S. Relations between the refractive index and energy gap of semiconductors. *Physica Status Solidi (b)* **131,** 415–427 (1985).

191. Ravichandran, R. *et al.* Solid state dielectric screening versus band gap trends and implications. *Optical Materials* **60,** 181–187 (2016).

192. Keldysh, L. V. Coulomb interaction in thin semiconductor and semimetal films. *JETP Letters* **29** (1979).

193. Keldysh, L. V. Excitons in semiconductor–dielectric nanostructures. *Physica Status Solidi (a)* **164,** 3–12 (1997).

194. Berkelbach, T. C. *et al.* Theory of neutral and charged excitons in monolayer transition metal dichalcogenides. *Physical Review B* **88,** 045318 (2013).

195. Cudazzo, P. *et al.* Dielectric screening in two-dimensional insulators: Implications for excitonic and impurity states in graphane. *Physical Review B* **84,** 085406 (2011).

196. Steinleitner, P. *et al.* Dielectric engineering of electronic correlations in a van der Waals heterostructure. *Nano Letters* **18,** 1402–1409 (2018).

197. Zhang, C. *et al.* Absorption of light by excitons and trions in monolayers of metal dichalcogenide $MoS_2$: Experiments and theory. *Physical Review B* **89,** 205436 (2014).

198. Ugeda, M. M. *et al.* Giant bandgap renormalization and excitonic effects in a monolayer transition metal dichalcogenide semiconductor. *Nature Materials* **13,** 1091–1095 (2014).

199. Wang, Y. *et al.* Screening effect of graphite and bilayer graphene on excitons in $MoSe_2$ monolayer. *2D Materials* **4,** 015021 (2017).

200. Desai, S. B. *et al.* Gold-mediated exfoliation of ultralarge optoelectronically-perfect monolayers. *Advanced Materials* **28,** 4053–4058 (2016).

201. Heyl, M. *et al.* Thermally–activated gold–mediated TMDC exfoliation and a unique gold–mediated transfer. *Physica Status Solidi (RRL) - Rapid Research Letters* (2020).

202. Jung, Y. *et al.* Recent progresses in the growth of two-dimensional transition metal dichalcogenides. *Journal of the Korean Ceramic Society* **56,** 24–36 (2019).

203. Chen, F. *et al.* The effect of the experimental parameters on the growth of $MoS_2$ flakes. *CrystEngComm* **20,** 4823–4830 (2018).

204. Wang, S. *et al.* Shape evolution of monolayer $MoS_2$ crystals grown by chemical vapor deposition. *Chemistry of Materials* **26,** 6371–6379 (2014).

205. Muratore, C. *et al.* Continuous ultra-thin $MoS_2$ films grown by low-temperature physical vapor deposition. *Applied Physics Letters* **104,** 261604 (2014).

206. Jiao, L. *et al.* Molecular-beam epitaxy of monolayer $MoSe_2$: growth characteristics and domain boundary formation. *New Journal of Physics* **17,** 053023 (2015).

207. Onomitsu, K. *et al.* Epitaxial growth of monolayer $MoSe_2$ on GaAs. *Applied Physics Express* **9,** 115501 (2016).

208. Hall, J. *et al.* Molecular beam epitaxy of quasi-freestanding transition metal disulphide monolayers on van der Waals substrates: a growth study. *2D Materials* **5,** 025005 (2018).

209. Virág, M. *et al.* Thermal field simulation of a tungsten filament lamp referring to its lifetime. *Journal of Electrical Engineering* **56,** 252–257 (2005).

210. Demtröder, W. *Elektrizität und Optik. Mit 11 Farbtafeln, 17 Tabellen, zahlreichen durchgerechneten Beispielen und 143 Übungsaufgaben mit ausführlichen Lösungen* 3., überarb. und erw. Aufl., korr. Nachdr. 482 pp. ISBN: 3540202102 (Springer, Berlin, 2004).

211. Severin, N. *et al.* Reversible dewetting of a molecularly thin fluid water film in a soft graphene-mica slit pore. *Nano Letters* **12,** 774–779 (2012).

212. Yang, P. *et al.* Batch production of 6-inch uniform monolayer molybdenum disulfide catalyzed by sodium in glass. *Nature Communications* **9,** 979 (2018).

213. Tongay, S. *et al.* Two-dimensional semiconductor alloys: Monolayer $Mo_{1-x}W_xSe_2$. *Applied Physics Letters* **104,** 012101 (2014).

214. Sahoo, P. K. *et al.* One-pot growth of two-dimensional lateral heterostructures via sequential edge-epitaxy. *Nature* **553,** 63–67 (2018).

215. Gong, Y. *et al.* Band gap engineering and layer-by-layer mapping of selenium-doped molybdenum disulfide. *Nano Letters* **14,** 442–449 (2014).

216. Gong, Y. *et al.* Vertical and in-plane heterostructures from $WS_2/MoS_2$ monolayers. *Nature materials* **13,** 1135–1142 (2014).

217. Zhang, W. *et al.* CVD synthesis of $Mo_{1-x}W_xS_2$ and $MoS_{2(1-x)}Se_{2x}$ alloy monolayers aimed at tuning the bandgap of molybdenum disulfide. *Nanoscale* **7,** 13554–13560 (2015).

218. Wang, Z. *et al.* Chemical vapor deposition of monolayer $Mo_{1-x}W_xS_2$ Crystals with Tunable Band Gaps. *Scientific reports* **6,** 21536 (2016).

219. Feng, Q. *et al.* Growth of large-area 2D $MoS_{2(1-x)}Se_{2x}$ semiconductor alloys. *Advanced Materials* **26,** 2648–53, 2613 (2014).

220. Chen, Y. *et al.* Tunable band gap photoluminescence from atomically thin transition-metal dichalcogenide alloys. *ACS Nano* **7,** 4610–4616 (2013).

221. Wang, G. *et al.* Spin-orbit engineering in transition metal dichalcogenide alloy monolayers. *Nature Communications* **6,** 10110 (2015).

222. Chen, Y. *et al.* Composition-dependent Raman modes of $Mo_{1-x}W_xS_2$ monolayer alloys. *Nanoscale* **6,** 2833–2839 (2014).

223. Shimada, T. *et al.* Work function and photothreshold of layered metal dichalcogenides. *Japanese Journal of Applied Physics* **33,** 2696–2698 (1994).

224. Park, Y. *et al.* Work function of indium tin oxide transparent conductor measured by photoelectron spectroscopy. *Applied Physics Letters* **68,** 2699–2701 (1996).

225. Ossila Corp. *ITO covered glass* `https://www.ossila.com/products/pv-substrates?variant=1200245025`.

226. Ma, D. *et al.* A universal etching-free transfer of $MoS_2$ films for applications in photodetectors. *Nano Research* **8,** 3662–3672 (2015).

227. Bhanu, U. *et al.* Photoluminescence quenching in gold-$MoS_2$ hybrid nanoflakes. *Scientific Reports* **4,** 5575 (2014).

228. Bruix, A. *et al.* Single-layer $MoS_2$ on Au(111): Band gap renormalization and substrate interaction. *Physical Review B* **93,** 165422 (2016).

229. Huang, Y. L. *et al.* The organic-2D transition metal dichalcogenide heterointerface. *Chemical Society Reviews* **47,** 3241–3264 (2018).

230. Kahn, A. Fermi level, work function and vacuum level. *Materials Horizons* **3,** 7–10 (2016).

231. Cahen, D. *et al.* Electron energetics at surfaces and interfaces: concepts and experiments. *Advanced Materials* **15,** 271–277 (2003).

232. Schlesinger, R. *Energy-Level Control at Hybrid Inorganic/Organic Semiconductor Interfaces* 223 pp. ISBN: 978-3-319-46623-1 (Springer International Publishing, Cham, 2017).

233. Ibach, H. *et al. Festkörperphysik* ISBN: 978-3-540-85794-5 (Springer Berlin Heidelberg, Berlin, Heidelberg, 2009).

234. Oehzelt, M. *et al.* Organic semiconductor density of states controls the energy level alignment at electrode interfaces. *Nature Communications* **5,** 4174 (2014).

235. Tuxen, A. *et al.* Size threshold in the dibenzothiophene adsorption on $MoS_2$ nanoclusters. *ACS Nano* **4,** 4677–4682 (2010).

236. Makarova, M. *et al.* Selective adsorption of thiol molecules at sulfur vacancies on $MoS_2$ (0001), followed by vacancy repair via S–C dissociation. *The Journal of Physical Chemistry C* **116,** 22411–22416 (2012).

237. Ding, Q. *et al.* Basal-plane ligand functionalization on semiconducting 2H-$MoS_2$ monolayers. *ACS Applied Materials & Interfaces* **9,** 12734–12742 (2017).

238. Förster, A. *et al.* Chemical and electronic repair mechanism of defects in $MoS_2$ monolayers. *ACS Nano* **11,** 9989–9996 (2017).

239. Nguyen, E. P. *et al.* Electronic tuning of 2D $MoS_2$ through surface functionalization. *Advanced Materials* **27,** 6225–6229 (2015).

240. Sim, D. M. *et al.* Controlled doping of vacancy-containing few-layer $MoS_2$ via highly stable thiol-based molecular chemisorption. *ACS Nano* **9,** 12115–12123 (2015).

241. Song, Z. *et al.* Electronic properties of a 1D intrinsic/p-doped heterojunction in a 2D transition metal dichalcogenide semiconductor. *ACS Nano* **11,** 9128–9135 (2017).

242. Park, S. *et al.* Demonstration of the key substrate-dependent charge transfer mechanisms between monolayer $MoS_2$ and molecular dopants. *Communications Physics* **2,** 109 (2019).

243. Gan, L.-Y. *et al.* Photovoltaic heterojunctions of fullerenes with $MoS_2$ and $WS_2$ monolayers. *The Journal of Physical Chemistry Letters* **5,** 1445–1449 (2014).

244. Chen, R. *et al.* Templating C60 on $MoS_2$ nanosheets for 2D hybrid van der Waals p–n nanoheterojunctions. *Chemistry of Materials* **28,** 4300–4306 (2016).

245. Baek, J. *et al.* Formation and photodynamic behavior of transition metal dichalcogenide nanosheet-fullerene inorganic/organic nanohybrids on semiconducting electrodes. *Chemistry* **24,** 1561–1572 (2018).

246. Jariwala, D. *et al.* Hybrid, gate-tunable, van der waals p-n heterojunctions from pentacene and $MoS_2$. *Nano Letters* **16,** 497–503 (2016).

247. Bettis Homan, S. *et al.* Ultrafast exciton dissociation and long-lived charge separation in a photovoltaic pentacene-$MoS_2$ van der Waals heterojunction. *Nano Letters* **17,** 164–169 (2017).

248. Shen, N. *et al.* Charge transfer and interface engineering of the pentacene and $MoS_2$ monolayer complex. *Advanced Materials Interfaces* **4,** 1601083 (2017).

249. Zhu, T. *et al.* Highly mobile charge-transfer excitons in two-dimensional $WS_2$/tetracene heterostructures. *Science Advances* **4,** eaao3104 (2018).

250. Zheng, Y. J. *et al.* Heterointerface screening effects between organic monolayers and monolayer transition metal dichalcogenides. *ACS Nano* **10,** 2476–2484 (2016).

251. Gu, J. *et al.* Dipole-aligned energy transfer between excitons in two-dimensional transition metal dichalcogenide and organic semiconductor. *ACS Photonics* **5,** 100–104 (2018).

252. Habib, M. R. *et al.* Tunable photoluminescence in a van der Waals heterojunction built from a $MoS_2$ monolayer and a PTCDA organic semiconductor. *Nanoscale* **10,** 16107–16115 (2018).

253. Liu, X. *et al.* Photoresponse of an organic semiconductor/two-dimensional transition metal dichalcogenide heterojunction. *Nano Letters* **17,** 3176–3181 (2017).

254. Obaidulla, S. M. *et al.* $MoS_2$ and perylene derivative based type–II heterostructure: bandgap engineering and giant photoluminescence enhancement. *Advanced Materials Interfaces* **7,** 1901197 (2020).

255. Wang, S. *et al.* A $MoS_2$/PTCDA hybrid heterojunction synapse with efficient photoelectric dual modulation and versatility. *Advanced Materials* **31,** 1806227 (2019).

256. Liu, F. *et al.* Van der Waals p-n junction based on an organic-inorganic heterostructure. *Advanced Functional Materials* **25,** 5865–5871 (2015).

257. Shastry, T. A. *et al.* Mutual photoluminescence quenching and photovoltaic effect in large-area single-layer $MoS_2$-polymer heterojunctions. *ACS Nano* **10,** 10573–10579 (2016).

258. Zhong, C. *et al.* Mechanisms of ultrafast charge separation in a PTB7/monolayer $MoS_2$ van der Waals heterojunction. *The Journal of Physical Chemistry Letters* **9,** 2484–2491 (2018).

259. Liu, X.-Y. *et al.* Nonadiabatic dynamics simulations reveal distinct effects of the thickness of PTB7 on interfacial electron and hole transfer dynamics in PTB7@$MoS_2$ heterostructures. *The Journal of Physical Chemistry Letters* **10,** 2949–2956 (2019).

260. Petoukhoff, C. E. *et al.* Charge transfer dynamics in conjugated polymer/$MoS_2$ organic/2D heterojunctions. *Molecular Systems Design & Engineering* **4,** 929–938 (2019).

261. He, D. *et al.* A van der Waals pn heterojunction with organic/inorganic semiconductors. *Applied Physics Letters* **107,** 183103 (2015).

262. Yu, S. H. *et al.* Dye-sensitized $MoS_2$ photodetector with enhanced spectral photoresponse. *ACS Nano* **8,** 8285–8291 (2014).

263. Huang, Y. *et al.* Effects of organic molecules with different structures and absorption bandwidth on modulating photoresponse of $MoS_2$ photodetector. *ACS Applied Materials & Interfaces* **8,** 23362–23370 (2016).

264. Cheng, C.-H. *et al.* Efficient energy transfer across organic-2D inorganic heterointerfaces. *ACS Applied Materials & Interfaces* **10,** 39336–39342 (2018).

265. Choi, J. *et al.* Modulating optoelectronic properties of two-dimensional transition metal dichalcogenide semiconductors by photoinduced charge transfer. *ACS Nano* **10,** 1671–1680 (2016).

266. Choudhury, P. *et al.* Modulating electronic and optical properties of monolayer $MoS_2$ using nonbonded phthalocyanine molecules. *The Journal of Physical Chemistry C* **121,** 2959–2967 (2017).

267. Ghimire, G. *et al.* Local enhancement of exciton emission of monolayer $MoS_2$ by copper phthalocyanine nanoparticles. *The Journal of Physical Chemistry C* **122,** 6794–6800 (2018).

268. Kafle, T. R. *et al.* Charge transfer exciton and spin flipping at organic-transition-metal dichalcogenide interfaces. *ACS Nano* **11,** 10184–10192 (2017).

269. Liu, X.-Y. *et al.* Theoretical insights into interfacial electron transfer between zinc phthalocyanine and molybdenum disulfide. *The Journal of Physical Chemistry. A* **122,** 9587–9596 (2018).

270. Nguyen, E. P. *et al.* Excitation dependent bidirectional electron transfer in phthalocyanine-functionalised $MoS_2$ nanosheets. *Nanoscale* **8,** 16276–16283 (2016).

271. Pak, J. *et al.* Enhancement of photodetection characteristics of $MoS_2$ field effect transistors using surface treatment with copper phthalocyanine. *Nanoscale* **7,** 18780–18788 (2015).

272. Pak, J. *et al.* Improved photoswitching response times of $MoS_2$ field-effect transistors by stacking p-type copper phthalocyanine layer. *Applied Physics Letters* **109,** 183502 (2016).

273. Park, J. H. *et al.* Defect passivation of transition metal dichalcogenides via a charge transfer van der Waals interface. *Science Advances* **3,** e1701661 (2017).

274. van Nostrum, C. F. *et al.* Functional supramolecular materials: self-assembly of phthalocyanines and porphyrazines. *Chemical Communications,* 2385 (1996).

275. Claessens, C. G. *et al.* Phthalocyanines: from outstanding electronic properties to emerging applications. *Chemical Record* **8,** 75–97 (2008).

276. Lo, P.-C. *et al.* The unique features and promises of phthalocyanines as advanced photosensitisers for photodynamic therapy of cancer. *Chemical Society Reviews* **49,** 1041–1056 (2020).

277. Urbani, M. *et al.* Phthalocyanines and porphyrinoid analogues as hole- and electron-transporting materials for perovskite solar cells. *Chemical Society Reviews* **48,** 2738–2766 (2019).

278. Hara, M. *et al.* Epitaxial growth of organic thin films by organic molecular beam epitaxy. *Japanese Journal of Applied Physics* **28,** 306–308 (1989).

279. Koma, A. Van der Waals epitaxy—a new epitaxial growth method for a highly lattice-mismatched system. *Thin Solid Films* **216,** 72–76 (1992).

280. Ueno, N. *et al.* Angle–resolved photoemission spectroscopy of ultrathin films of $H_2$ –phthalocyanine on $MoS_2$ surfaces. *The Journal of Chemical Physics* **99,** 7169–7174 (1993).

281. Momose, M. *et al.* Growth and stability of $H_2$–phthalocyanine thin films on $MoS_2$ surfaces studied by means of low-energy electron eransmission Spectroscopy. *Japanese Journal of Applied Physics* **33,** 4754–4758 (1994).

282. Kamiya, K. *et al.* Determination of two-dimensional structures of ultrathin films of $H_2$ and Cu phthalocyanine on $MoS_2$ by angle-resolved ultraviolet photoemission and low energy electron diffraction. *Journal of Electron Spectroscopy and Related Phenomena* **76,** 213–218 (1995).

283. Kamiya Okudaira, K. *et al.* Structure of copper- and $H_2$-phthalocyanine thin films on $MoS_2$ studied by angle-resolved ultraviolet photoelectron spectroscopy and low energy electron diffraction. *Journal of Applied Physics* **85,** 6453–6461 (1999).

284. Late, D. J. *et al.* Hysteresis in single-layer $MoS_2$ field effect transistors. *ACS Nano* **6,** 5635–5641 (2012).

285. Zhang, W. *et al.* High-gain phototransistors based on a CVD $MoS_2$ monolayer. *Advanced Materials* **25,** 3456–3461 (2013).

286. Lopez-Sanchez, O. *et al.* Ultrasensitive photodetectors based on monolayer $MoS_2$. *Nature Nanotechnology* **8,** 497–501 (2013).

287. Furchi, M. M. *et al.* Mechanisms of photoconductivity in atomically thin $MoS_2$. *Nano Letters* **14,** 6165–6170 (2014).

288. Lee, Y. *et al.* Trap-induced photoresponse of solution-synthesized $MoS_2$. *Nanoscale* **8,** 9193–9200 (2016).

289. Han, P. *et al.* Ambient effects on photogating in $MoS_2$ photodetectors. *Nanotechnology* **30,** 284004 (2019).

290. Kufer, D. *et al.* Highly sensitive, encapsulated $MoS_2$ photodetector with gate controllable gain and speed. *Nano Letters* **15,** 7307–7313 (2015).

291. Park, Y. *et al.* Thermally activated trap charges responsible for hysteresis in multilayer $MoS_2$ field-effect transistors. *Applied Physics Letters* **108,** 083102 (2016).

292. Buscema, M. *et al.* Photocurrent generation with two-dimensional van der Waals semiconductors. *Chemical Society Reviews* **44,** 3691–3718 (2015).

293. Eyer, M. *et al.* Role of Hybrid Charge Transfer States in the Charge Generation at ZnMgO/P3HT Heterojunctions. *The Journal of Physical Chemistry C* **121,** 21955–21961 (2017).

294. Zhang, C. *et al.* Systematic study of electronic structure and band alignment of monolayer transition metal dichalcogenides in Van der Waals heterostructures. *2D Materials* **4,** 015026 (2017).

295. Caplins, B. W. *et al.* Femtosecond to nanosecond excited state dynamics of vapor deposited copper phthalocyanine thin films. *Physical Chemistry Chemical Physics* **18,** 11454–11459 (2016).

296. Zahn, D. R. *et al.* The transport gap of organic semiconductors studied using the combination of direct and inverse photoemission. *Chemical Physics* **325,** 99–112 (2006).

297. Lucia, E. A. *et al.* Spectra of polycrystalline phthalocyanines in the visible region. *The Journal of Chemical Physics* **48,** 2674–2681 (1968).

298. Bayliss, S. M. *et al.* Thin film properties and surface morphology of metal free phthalocyanine films grown by organic molecular beam deposition. *Physical Chemistry Chemical Physics* **1,** 3673–3676 (1999).

299. Yoshida, H. *et al.* Charge-transfer excitation bands in electro-absorption spectra of metal (Co, Ni, Cu, Zn)-phthalocyanine films. *Chemical Physics* **109,** 375–382 (1986).

300. Heutz, S. *et al.* Polymorphism in phthalocyanine thin films: mechanism of the $\alpha \rightarrow \beta$ transition. *The Journal of Physical Chemistry B* **104,** 7124–7129 (2000).

301. Yim, S. *et al.* Model for the $\alpha \rightarrow \beta 1$ phase transition in phthalocyanine thin films. *Journal of Applied Physics* **91,** 3632–3636 (2002).

302. Alkhamisi, M. *et al.* The growth and fluorescence of phthalocyanine monolayers, thin films and multilayers on hexagonal boron nitride. *Chemical Communications* **54,** 12021–12024 (2018).

303. Gadalla, A. *et al.* Ultrafast optical dynamics of metal-free and cobalt phthalocyanine thin films. *The Journal of Physical Chemistry C* **114,** 4086–4092 (2010).

304. Huang, H. *et al.* Van der Waals heterostructures between small organic molecules and layered substrates. *Crystals* **6,** 113 (2016).

305. Heliotis, G. *et al.* Hybrid inorganic/organic semiconductor heterostructures with efficient non-radiative energy transfer. *Advanced Materials* **18,** 334–338 (2006).

306. Chanyawadee, S. *et al.* Photocurrent enhancement in hybrid nanocrystal quantum-dot p-i-n photovoltaic devices. *Physical Review Letters* **102,** 077402 (2009).

307. Ghataora, S. *et al.* Electrically injected hybrid organic/inorganic III-nitride white light-emitting diodes with nonradiative Förster resonance energy transfer. *ACS Photonics* **5,** 642–647 (2018).

308. Erdem, T. *et al.* Morphology-dependent energy transfer of polyfluorene nanoparticles decorating InGaN/GaN quantum-well nanopillars. *The Journal of Physical Chemistry C* **117,** 18613–18619 (2013).

# List of publications

The following publications originated during the course of this doctorate:

- N. Mutz, H. Kirmse, C. T. Koch, E. J. W. List-Kratochvil, and S. Blumstengel, *Energy transfer between cyano-ether PPV and InGaN/GaN quantum wells with large piezoelectric fields*, Physica Status Solidi (a) 215, 1800322, 2018

- N. Mutz, T. Meisel, H. Kirmse, S. Park, N. Severin, J. P. Rabe, E. J. W. List-Kratochvil, N. Koch, C. T. Koch, S. Blumstengel, and S. Sadofev, *Pulsed thermal deposition of binary and ternary transition metal dichalcogenide monolayers and heterostructures*, Applied Physics Letters 114, 162101, 2019

- N. Mutz, S. Park, T. Schultz, S. Sadofev, S. Dalgleish, L. Reissig, N. Koch, E. J. W. List-Kratochvil, and S. Blumstengel, *Excited state charge transfer enabling $MoS_2$/Phthalocyanine photodetectors with extended spectral sensitivity*, The Journal of Physical Chemistry C 124, 2837, 2020

- S. Park, N. Mutz, T. Schultz, S. Blumstengel, A. Han, A. Aljarb, L.-J. Li, E. J. W. List-Kratochvil, P. Amsalem, and N. Koch, *Direct determination of monolayer $MoS_2$ and $WSe_2$ exciton binding energies on insulating and metallic substrates*, 2D Materials 5, 025003, 2018

- S. Vempati, J.-C. Deinert, L. Gierster, L. Bogner, C. Richter, N. Mutz, S. Blumstengel, A. Zykov, S. Kowarik, Y. Garmshausen, J. Hildebrandt, S. Hecht, and J. Stähler, *Uncovering the (un-)occupied electronic structure of a buried hybrid interface*, Journal of Physics: Condensed Matter 31, 094001, 2019

Other Publications:

- J. A. Sichert, Y. Tong, N. Mutz, M. Vollmer, S. Fischer, K. Z. Milowska, R. Garciía Cortadella, B. Nickel, C. Cardenas-Daw, J. K. Stolarczyk, A. S. Urban, and J. Feldmann, *Quantum size effect in organometal halide perovskite nanoplatelets*, Nano Letters 15, 6521, 2015

# Acknowledgements

This work would not have been possible without the help and assistance of many people. First, I would like to thank PD Dr. Sylke Blumstengel and Prof. Dr. Emil List-Kratochvil: Dr. Sylke Blumstengel for supervising the thesis, her support in planning the experiments, scientific input and help in interpreting and analysing the data on a day-to-day basis. Prof. Emil List-Kratochvil for the opportunity to do my thesis in his group, his advise and feedback, especially when considering the broader picture. I also thank Prof. Oliver Benson for his supervision in the beginning of my thesis in the former AG Photonik.

Many thanks go to Dr. Sergey Sadofev for his support and the development of the PTD process as well as his ideas in MBE growth in general.

I would like to thank Dr. Simon Dalgleish for his expertise in devices and chemistry and the whole hybrid devices group, in particular Bodo Kranz and Pauly Zybarth who are always available for any questions in and around the labs and providing solutions. Further I want to thank Marion Adam and Claudia Rothkirch.

Thanks go to the SMS group of Prof. Norbert Koch, especially to Dr. Soohyung Park and Dr. Thorsten Schultz for their PES and XPS measurements and the superb collaboration. The same thanks go towards the group of Prof. Christoph Koch and within to Dr. Holm Kirmse for TEM analysis and making the smallest structures visible. I want to thank Lukas Gierster and the group of Prof. Julia Stähler. Additionally, a lot of thanks go to the former members of the AG Photonik and Volker Misch for always having a can of liquid helium ready.

I want to thank Evgenij Travkin, Tino Meisel, Sebastian Kickhöfel, Nicolas Zorn Morales, Seon-Young Rhim, Hala Memmi and Edgar Nandayapa who were part in and out of university.

Nothing would have been possible without the support of all my friends and family, my parents Dieter and Claudia and my brother Pascal. I want to thank Petra, Frederic and Nicolai. Special thanks go to Matea for being in my life.

# Selbstständigkeitserklärung

Ich erkläre, dass ich die Dissertation selbstständig und nur unter Verwendung der von mir gemäß § 7 Abs. 3 der Promotionsordnung der Mathematisch-Naturwissenschaftlichen Fakultät, veröffentlicht im Amtlichen Mitteilungsblatt der Humboldt-Universität zu Berlin Nr. 42/2018 am 11.07.2018 angegebenen Hilfsmittel angefertigt habe. Desweiteren erkläre ich, dass ich mich nicht anderwärts um einen Doktorgrad in dem Promotionsfach beworben habe und keinen entsprechenden Doktorgrad besitze. Die Promotionsordnung der Mathematisch-Naturwissenschaftlichen Fakultät, veröffentlicht im Amtlichen Mitteilungsblatt der Humboldt-Universität zu Berlin Nr. 42 am 11. Juli 2018, habe ich zur Kenntnis genommen.

Berlin, den 04.11.2020

Niklas Mutz